



Simon Prato

Numerical Investigation of TEM Cells and Antenna Coupling

Master Thesis

Studies: Electrical Engineering

submitted to

Technical University of Graz

Supervisor

Dr. Thomas Bauernfeind



Graz, August 2024

Abstract

Electrically small antennas that conduct high-frequency signals can produce significant electromagnetic emissions. The characterization of these emissions by measurement in a TEM cell remains a widely used procedure. This thesis develops a theoretical framework for understanding the coupling mechanisms between the antenna and the TEM cell, and investigates these concepts through numerical analysis.

In the context of these investigations, emphasis is laid on electric and magnetic dipole moments, which effectively represent electrically small radiating sources. The magnitudes of these dipole moments accurately describe the electric and magnetic coupling independently. While established measurement-based methods with the TEM cell for determining these magnitudes exists, this thesis focuses on leveraging the finite element method to eliminate potential inaccuracies arising from the measurement setup and procedure.

The findings in this thesis assist in understanding the influence of the geometrical and electrical characteristics of the antennas on the coupling behavior, and provide the knowledge necessary for manipulating the generated dipole moments. This proves useful, for example, when aiming to increase electromagnetic compatibility of an electronic system containing electrically small conducting structures.

Contents

1	Introduction	1
2	Dipole Theory	2
2.1	Electric Dipoles	2
2.1.1	Infinitesimal Electric Dipoles	2
2.1.2	Small Electric Dipoles	5
2.2	Magnetic Dipoles	6
2.3	Radiated Field	8
2.3.1	Field regions	8
2.3.2	Energy densities and reactances	10
3	Guided Waves	10
3.1	Lorentz Reciprocity Theorem	10
3.2	Green's Function	11
3.2.1	Scalar Green's Function	11
3.2.2	Dyadic Green's Function	13
3.3	Modes in Waveguides	14
3.3.1	Rectangular Waveguides as non-TEM structures	14
3.3.2	TEM mode in the TEM cell	15
3.3.3	Higher-order modes	17
3.3.4	Field distributions	19
3.4	Radiating Sources in TEM Cells	22
3.4.1	Arbitrary source	22
3.4.2	Equivalent dipole moments	23
3.4.3	Electrically small antennas	26
3.4.4	Radiation resistance	28
3.5	Shielding	30
3.5.1	Incident, reflected and transmitted waves in medium	30
3.5.2	Electrical characteristics	31
3.5.3	ASTM ES7-83 Method	33
3.5.4	Dual TEM cell	34
4	Finite Element Method	34
4.1	General Idea	34
4.2	Dividing a computational domain into finite elements	35
4.3	Solving the differential equation	37
4.4	Adaptive solution process	38
5	Numerical Investigations of Antennas in TEM Cells	39
5.1	Preliminary Considerations for Numerical Analysis	39
5.1.1	Skin Effect	39
5.1.2	Antenna models	39
5.1.3	TEM cell model	40
5.1.4	Dipole moments models	41
5.1.5	Mesh modifications	41

5.1.6	Shielding material models	42
5.1.7	S-parameters and derived data	42
5.1.8	Investigation of field regions	43
5.2	Monopole Antenna	46
5.2.1	Setup	46
5.2.2	Equivalent dipole moments	46
5.2.3	Electrical characteristics	47
5.2.4	Current distribution on septum	50
5.2.5	Electromagnetic energy in the TEM cell	51
5.3	Loop antenna	52
5.3.1	Setup	52
5.3.2	Equivalent dipole moments	52
5.3.3	Electrical characteristics	54
5.3.4	Equivalent circuit model	56
5.3.5	Current distribution on septum and higher order modes	59
5.3.6	Influence of antenna's geometry	61
5.4	Loop antenna with gap	62
5.4.1	Setup and geometrical analysis	62
5.4.2	Equivalent dipole moments	63
5.4.3	Electrical characteristics	63
5.5	Inverted-F and center-fed monopole antenna	66
5.5.1	Setup and geometrical analysis	66
5.5.2	Equivalent dipole moments	66
6	Application of Shielding Techniques in TEM Cells	67
6.1	ASTM ES7-83 method	67
6.2	Dual TEM cell	68
6.3	Antennas in shield enclosure	70
6.4	Dipole moments in shield enclosure	71
7	Conclusion	72

List of Figures

2.1	Geometrical arrangement of an infinitesimal electric dipole. It contains a capacitor-plate at each end of the wire to provide a constant current $\mathbf{I}(z)$	3
2.2	Geometrical arrangement of a linear, center-fed wire antenna with a feed-point indicated in the center. The feedpoint consists of a small gap providing current I_0 to the antenna.	5
2.3	Current distribution across linear wire antenna. It has a maximum at the feedpoint, and drops to zero at points $d/2$ and $-d/2$	6
2.4	Geometrical arrangement of a current loop with radius b fed by a current I_0 , producing a magnetic dipole moment \mathbf{m}_m . Alternatively, a magnetic current I_m flows perpendicular to the loop's area along the distance L , which produces an equivalent magnetic dipole moment.	7
2.5	Behavior of Expression 1 and Expression 2 in Equation 2.20 over distance r . The distance r is normalized to the radian distance $\lambda/2\pi$. The magnitude of both expressions is normed to 1 at radian distance to improve comparison.	9
2.6	Field regions of an antenna, here specifically a linear wire antenna, although they are applicable for any antenna with dimension d	10
3.1	The electric and magnetic fields of each the first dominant TE and TM mode in a hallow rectangular waveguide with perfectly conducting walls.	14
3.2	The Green's function in this analysis solves the fields in the cross section surface S of the TEM cell1, which is colored in light gray and bounded by l . The source exciting these fields is a centered, electric dipole moment \mathbf{m}_e	16
3.3	Geometrical arrangement of the TEM cell, demonstrated with cross sections in the xy-plane and the yz-plane.	17
3.4	Forward transmission coefficients S_{12} of the TEM, TE ₀₁ and TE ₁₀ modes in the TEM cell over frequency.	18
3.5	Transversal electric fields in cross section of TEM cell	19
3.6	Output power and $\mathbf{e}_{\text{TEM}}^{\pm}$ for different electric dipole moment positions and orientations.	21
3.7	The normalized electric field distribution $\mathbf{e}_{\text{TEM}}^{\pm}$ in the TEM cell excited with an input power of 1/2 W at a frequency of 3 GHz.	21
3.8	TEM cell with an arbitrary current source \mathbf{J}_1 along the curve τ . \mathbf{E} and \mathbf{H} are the field intensities induced by the current. \mathbf{e}_n^+ and \mathbf{e}_n^- are outgoing fields towards both output ports of the TEM cell of arbitrary form. \mathbf{S} indicates the surface, and V the volume of the domain in question.	22
3.9	Field distribution of the TEM mode highlighting the out-of-phase magnetic fields at the output ports.	25
3.10	Sketch of the surfaces S_0, S_1 and S_2 in the TEM cell with an example antenna, coupling through S_0 to the septum over the displacement current $\partial\mathbf{D}/\partial t$	27
3.11	TEM cell with vertical antenna inserted	29
3.12	Incident, reflected and transmitted electric field intensities at a shielding material.	31
3.14	Dual TEM cell with aperture	34
4.1	Tetrahedron with points on the edge and vertices.	36

4.2	Face of the finite element with unknowns	37
4.3	Adaptive solution process	39
5.1	Geometry of an antenna's feedpoint used in simulation. The antenna is fed through a round waveport of diameter 0.46 mm. The antenna consists of PEC wire with diameter of 0.2 mm. This geometry leads to a reference impedance of $Z_0 \approx 50 \Omega$	40
5.2	Circuit representing the TEM cell, where the capacitance and inductance is split into two separate, equal components $C_T = C_{T1} + C_{T2}$, $L_T = L_{T1} + L_{T2}$ and $C_{T1} = C_{T2}$, $L_{T1} = L_{T2}$. The resistances R_1, R_2 at the output ports model the reference impedance $Z_w \approx 50 \Omega$	40
5.3	A TEM cell containing an electric \mathbf{m}_e and a magnetic dipole moment \mathbf{m}_m in the center $x = 0, y = r = b/4, z = 0$ to investigate the field regions in which the coupling occurs.	44
5.4	$k \cdot r$ in small TEM cell	44
5.5	Moments in small TEM cell	45
5.6	Moments in normal TEM cell	45
5.7	Output powers	45
5.8	Phase shifts	45
5.9	The geometrical aspects of the cylindrical monopole antenna, as implemented in the simulation model, with the respective electric near-field plot.	46
5.10	The equivalent electric and magnetic dipole moments analytically calculated with Equations (3.44a) to (3.44b). To enable direct comparison with the magnetic dipole moment, the electric dipole moment is weighted with the free space impedance Z_0 , as discussed in subsubsection 5.1.4.	47
5.11	Magnitude of the voltage and current applied at the feedpoint of the monopole antenna over frequency, derived through the S-parameters with Equations (5.7) to (5.8), with the respective magnitude and phase of the antenna impedance over frequency, derived through the S-parameters with Equation 5.9.	48
5.12	Electric field in y-direction E_y at $x = 0, y = b/4, z = \pm l/2$, and power at one output port, derived with the S-parameters in Equation 5.5. The output power produced by the monopole antenna is compared to the output power produced by the equivalent dipole moments, to demonstrate validity of the model.	49
5.13	Current distribution at 3 GHz	49
5.14	Current distribution at 1 MHz	49
5.15	The current distribution along the monopole antenna at 3 GHz and 1 MHz.	49
5.16	The Chu equivalent circuit for a short electric dipole models the monopole antenna's behavior.	50
5.17	Current surface densities at different frequencies, below and above the cut-off frequency of the TE ₀₁ -mode.	51
5.18	Electric energy determined by integrating the electric field over the TEM cell volume, using Equation 2.22.	52

5.19	The geometry of the loop antenna assimilates a square with round edges. The height and width of the antenna equal $h = w = 1.6$ mm. The return path leads back to the PEC surface of the TEM cell. The electric near-field shows large a displacement current and voltage drop near the feed-point. It has been derived with a refined mesh on the antenna surface and near the feedpoint, according to the discussion in Section 5.1.5.	53
5.20	The equivalent dipole moments of the loop antenna are derived analytically with Equations (3.44a) to (3.44b), where the electric dipole moment \mathbf{m}_e is weighted with Z_0 to enable comparison with \mathbf{m}_m . The phases of the powers at output ports 1 and 2 are derived from the S-parameters, as discussed in Section 5.1.7. The analysis specifically focuses on the phase shift between the two ports, which provides information about the presence of \mathbf{m}_m and \mathbf{m}_e , as investigated in Section 3.4.2.	53
5.21	Electric field in y-direction E_y at $x = 0, y = b/4, z = \pm l/2$, and the closely related power at one of the output ports, derived with the S-parameters in Equation 5.5. The output power produced by the loop antenna is compared with that generated by the equivalent dipole moments.	54
5.22	Electric and magnetic energy produced by the loop antenna in the TEM cell, derived with Equation 2.22 in the TEM cell volume.	55
5.23	This figure demonstrates the voltage, current and impedance characteristics of the loop antenna. The difference between the current near the feedpoint and that on the return path increases with frequency, indicating a growing occurrence of displacement currents. The current on those paths are determined through magnetic near-field intensity, using Equation 5.11. The voltage across the feedpoint is obtained using Equation 5.8. Magnitude and phase of the impedance of the loop antenna are determined with Equation 5.9.	55
5.24	Equivalent circuits of the small loop antenna.	56
5.25	Loop antenna in free space on PEC plane	57
5.26	Model of the loop antenna connected to a feedpoint mounted on a PEC surface with a side length of $\lambda/2$, where λ corresponds to the free-space wavelength of the solution frequency. This configuration enables the investigation of the loop antenna reactance without influence of the TEM cell.	57
5.27	Circuit representing the TEM cell and the loop antenna, with the additional components C_k and $M_{A,T1}, M_{A,T2}$ modeling their near-field coupling behavior.	58
5.28	Equivalent dipole moments derived by the equivalent circuit depicted in Figure 5.27, compared to the dipole moments of the loop antenna, shown in Figure 5.20a. The electric dipole moment \mathbf{m}_e is weighted with Z_0 for comparison purposes.	58
5.29	Surface current density on the septum induced by the loop antenna for different frequencies and positions of the antenna.	60
5.30	Output power transmitted by the antenna to the output port through the TEM and TE_{01} modes, separately over frequency, determined through the S-parameters with Equation 5.5. At a frequency of $f = 3.21$ GHz a resonance in the TEM cell occurs, leading to the visible peak in the output power produced by the TE_{01} mode.	61

5.31 Dipole moments and output power comparisons of two different loop antenna configurations presented, one with $h = 2.16$ mm, $w = 1.4$ mm and the other with $h = 1.2$ mm, $w = 2.36$ mm. The electric dipole moment \mathbf{m}_e is weighted with Z_0 for comparison purposes.	62
5.32 Geometry of the loop antenna with a gap in the return path inserted in the TEM cell. The gap height is exaggerated for demonstration purposes.	63
5.33 The equivalent dipole moments of the loop antenna with a gap, where the electric dipole moment \mathbf{m}_e is weighted with Z_0 to enable comparison with \mathbf{m}_m . The phases of the powers at output ports 1 and 2 are derived from the S-parameters, as discussed in Section 5.1.7. The analysis specifically focuses on the phase shift between the two ports, which provides information about the presence of \mathbf{m}_m and \mathbf{m}_e , as investigated in Section 3.4.2.	64
5.34 Comparison of dipole moments, where the electric dipole moment \mathbf{m}_e is weighted with η_0 to enable comparison with \mathbf{m}_m , and output power for different gap heights in the loop antenna.	65
5.35 The voltage and current across the feedpoint, together with the related impedance of the loop antenna with gap.	65
5.36 Geometries of IFA and CFM antenna, together with their equivalent dipole moments. the electric dipole moment \mathbf{m}_e is weighted with the free space impedance Z_0 to enable comparison with the magnetic dipole moment \mathbf{m}_m	66
6.1 Shielding effectiveness of a sheet of zinc and nickel versus the material thickness determined with the ASTM ES7-83 Method.	67
6.2 The sum $P_{\text{ref,sum}}$ and difference $P_{\text{ref,diff}}$ of the reference power, measured with empty aperture and calculated with the phase information considered.	68
6.3 The sum $P_{\text{load,sum}}$ and difference in output power $P_{\text{load,diff}}$ measured at port 3 and 4 with the phase information considered.	69
6.4 The electric SE_{dB}^e and magnetic SE_{dB}^m shielding effectiveness derived with Equations (3.69a) and (3.69b).	70
6.5 Investigated antennas placed in the TEM cell covered in a cubic, hollow enclosure.	70
6.6 Output power over frequency produced by antennas with and without enclosure.	71

List of Tables

3.1	Cut-off frequencies of higher order modes at different TEM cell dimensions. The TE ₁₀ -mode is independent of the height b of the TEM cell, as would be the case in a rectangular waveguide. Both the TE ₁₀ -mode and the TE ₀₁ - mode are dependent on the width a	19
6.1	Electromagnetic Properties of barium titanate and ferrite	68

1 Introduction

Over the past several years, electronic systems have exhibited a clear trend towards smaller physical dimensions and faster operating speeds. As such, they commonly contain small conducting structures carrying currents with high amplitude and frequency. These structures tend to radiate and are susceptible to electromagnetic radiation, behaving as antennas and causing electromagnetic compatibility (EMC) issues.

Designing an electronic system with EMC issues in mind minimizes additional cost and schedule delays caused by potential redesigns, and ensures the correct operation of the product in the presence of interference sources [28, p. 64]. Consequently, research focusing on all aspects of EMC is conducted regularly. This thesis aims to contribute to these ongoing investigations, specifically through analysis of the previously mentioned small antennas and their coupling behavior in TEM cells. TEM cells are included because they are useful for measuring electromagnetic emissions in approximate free-space conditions and have been widely used for small devices [10, 19, 12].

Several studies have analyzed small antennas and devices in TEM cells [31, 22]. Specifically, [21, 20, 35] implement electric and/or magnetic dipole moments to model the radiated fields of such antennas, which provide information about the electric and magnetic coupling with the TEM cell, respectively. The magnitudes of the dipole moments are found by measurements with the TEM cell [31] or numerical analysis [20]. This thesis treats the coupling behavior of small antennas modeled with dipole moments using the latter approach, namely numerical computation using the finite element method. The advantage of this approach is the absence of inaccuracies caused by the measurement setup or related uncertainties, allowing the analysis to focus on the underlying mechanics behind the coupling behavior.

The purpose of this thesis to fill the gap in understanding how the electric and magnetic dipole moments representing such antennas are formed and on which variables they depend. This knowledge assists in the EMC-compliant design of radiating structures in electronic devices, such that specific electric and magnetic coupling behavior is achieved.

Furthermore, shielding materials in the presence of dipole moments are investigated. Replacing computationally expensive models of small radiating structures with dipole moments can significantly reduce the simulation time required to determine the coupling between the device and the TEM cell in the presence of shielding materials.

To achieve these objectives, this thesis first presents the theoretical foundations of electric and magnetic dipole moments in Section 2. The behavior of electromagnetic waves generated by arbitrary sources in waveguides, such as the TEM cell, is then discussed in Section 3. Further, methods to determine shielding effectiveness using the TEM cell are presented. A brief overview of the finite element method is provided in Section 4.

Subsequently, Section 5 addresses the numerical modeling of antennas and the TEM cell and investigates the generation of electric and magnetic dipole moments for monopole and loop antennas using the theoretical framework developed earlier. This knowledge is applied to three additional antennas, whose analysis closely follows that of the monopole and loop antennas due to their predominantly inductive or capacitive characteristics, which emerge

as the primary distinction in the antenna coupling behavior. Equivalent circuits to model capacitive and inductive antennas, together with the TEM cell and their coupling paths, are developed, from which the dipole moments can be investigated in more detail.

Section 6 demonstrates the application of shielding materials in numerical simulations involving dipole moments and electrically small antennas. Lastly, section 7 presents the conclusions and discussion derived from this thesis, along with potential directions for future research.

2 Dipole Theory

2.1 Electric Dipoles

2.1.1 Infinitesimal Electric Dipoles

An electric dipole can be modeled as two tiny charged metal spheres [11, p. 467], or alternatively two capacitor-plates [3, p. 151], connected with a linear wire of length d and diameter a . The charges accelerate along the wire and radiate. In case of an ideal, infinitesimal dipole, the wire is very thin ($a \ll \lambda$) and very small ($d \ll \lambda$) compared to the wavelength λ [3, p. 151, 11, p. 468]. For an antenna to be accurately modeled as an infinitesimal electric dipole, its length must be smaller than a fiftieth of the wavelength ($d < \lambda/50$) [3, p. 156]. They are not very practical, but serve as a basic building block for more complex geometries, or as an excitation source in numerical investigations.

An infinitesimal electric dipole, illustrated in Figure 2.1, is analyzed in detail below. The dipole is aligned with the z -axis, which simplifies the following mathematical investigations. Time variation according to $e^{-j\omega t}$ is assumed and therefore omitted. A current flows in the wire, which is spatially uniform throughout the wire. This is expressed as [3, p. 151]

$$\mathbf{I}(z) = \hat{\mathbf{a}}_z I_0. \quad (2.1)$$

The capacitances modeled at the ends of the wire allow for a constant current flow, which would otherwise be physically impossible. The electric dipole moment can be expressed as

$$\mathbf{m}_e = I_0 d \cdot \hat{\mathbf{a}}_z. \quad (2.2)$$

Next, the vector potential \mathbf{A} is determined through the general expression

$$\mathbf{A}(\mathbf{x}) = \frac{\mu}{4\pi} \frac{e^{-jkr}}{r} \iiint_V \mathbf{J}(\mathbf{x}') dv'. \quad (2.3)$$

The vector $\mathbf{x} = \hat{\mathbf{a}}_x x + \hat{\mathbf{a}}_y y + \hat{\mathbf{a}}_z z$ represents the observation point coordinates, while $\mathbf{x}' = \hat{\mathbf{a}}_x x' + \hat{\mathbf{a}}_y y' + \hat{\mathbf{a}}_z z'$ represents the source point coordinates. The vectors $\hat{\mathbf{a}}_x$, $\hat{\mathbf{a}}_y$, and $\hat{\mathbf{a}}_z$ are unit vectors along the x -, y -, and z -directions, respectively. \mathbf{J} is the current density in

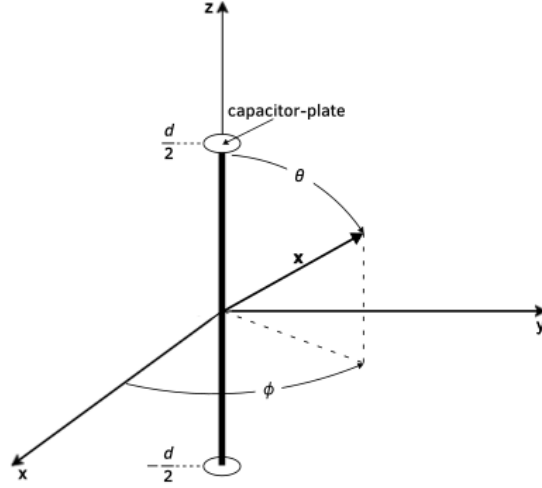


Figure 2.1 Geometrical arrangement of an infinitesimal electric dipole. It contains a capacitor-plate at each end of the wire to provide a constant current $\mathbf{I}(z)$.

the source region. The variable r is the distance from any source point to the observation point $|\mathbf{x} - \mathbf{x}'|$. In this case, the source point $\mathbf{x}' = \mathbf{0}$, due to the infinitesimal dipole [3, p. 152]. The permeability is described by μ and the propagation of the wave by e^{jkr} , where $k = 2\pi/\lambda$ is the propagation factor, or often called wavenumber.

The integration is performed over the volume V of the antenna. This leads to [3, p. 153]

$$\mathbf{A}(\mathbf{x}) = \hat{\mathbf{a}}_z \frac{\mu I_0}{4\pi r} e^{-jkr} \int_{-d/2}^{+d/2} dz' = \hat{\mathbf{a}}_z \frac{\mu I_0 d}{4\pi r} e^{-jkr}. \quad (2.4)$$

Any other field quantities can be derived out of the vector potential \mathbf{A} , such as the electric field intensity \mathbf{E} and magnetic field intensity \mathbf{H} . To simplify this process, the Cartesian components of \mathbf{A} are first transformed into spherical ones. This transform is given in matrix form as [3, p. 153]

$$\begin{bmatrix} A_r \\ A_\theta \\ A_\phi \end{bmatrix} = \begin{bmatrix} \sin \theta \cos \phi & \sin \theta \sin \phi & \cos \theta \\ \cos \theta \cos \phi & \cos \theta \sin \phi & -\sin \theta \\ -\sin \phi & \cos \phi & 0 \end{bmatrix} \begin{bmatrix} A_x \\ A_y \\ A_z \end{bmatrix}, \quad (2.5)$$

where θ is the polar angle and ϕ is the azimuthal angle of the observation point \mathbf{x} . \mathbf{E} and \mathbf{H} are then expressed by [3, p. 153],

$$\mathbf{H} = \frac{1}{\mu r} \left[\frac{\partial}{\partial r} (r A_\theta) - \frac{\partial A_r}{\partial \theta} \right] \hat{\mathbf{a}}_\phi, \quad (2.6a)$$

$$\mathbf{E} = -j\omega \mathbf{A} - j \frac{1}{\omega \mu \epsilon} \nabla (\nabla \cdot \mathbf{A}). \quad (2.6b)$$

Substituting \mathbf{A} into Equations (2.6a) and (2.6b) reduces them to

$$E_r = \eta \frac{I_0 d \cos \theta}{2\pi r^2} \left[1 + \frac{1}{jkr} \right] e^{-jkr}, \quad (2.7a)$$

$$E_\theta = j\eta \frac{k I_0 d \sin \theta}{4\pi r} \left[1 + \frac{1}{jkr} - \frac{1}{(kr)^2} \right] e^{-jkr}, \quad (2.7b)$$

$$E_\phi = 0. \quad (2.7c)$$

and,

$$H_r = H_\theta = 0, \quad (2.8a)$$

$$H_\phi = j \frac{k I_0 d \sin \theta}{4\pi r} \left[1 + \frac{1}{jkr} \right] e^{-jkr}, \quad (2.8b)$$

$\eta = \sqrt{\frac{\mu}{\epsilon}}$ is the wave impedance of the medium in which the waves travel.

The total radiated power of the dipole is obtained by integrating the complex Poynting vector \mathbf{W} over a closed surface surrounding the dipole [3, p. 154]. The real part of the total radiated power provides information about energy transferred by radiation, while the imaginary part about the antenna's reactive behavior. \mathbf{W} is defined by

$$\mathbf{W} = \frac{1}{2} (\mathbf{E} \times \mathbf{H}^*). \quad (2.9)$$

The real power transfer is derived through the time-averaged Poynting vector \mathbf{W}_{av} [3, p. 160], which is calculated by

$$\mathbf{W}_{av} = \frac{1}{2} \Re\{\mathbf{E} \times \mathbf{H}^*\}. \quad (2.10)$$

The complex power P is derived by integrating \mathbf{W} over a closed surface around the dipole, which leads to [3, p. 154]

$$P_r = \eta \frac{\pi |I_0 l|^2}{3 \lambda} \left[1 - j \frac{1}{(kr)^3} \right]. \quad (2.11)$$

The imaginary part of the power radiated by the infinitesimal electric dipole shows capacitive behavior, as demonstrated by Equation 2.11.

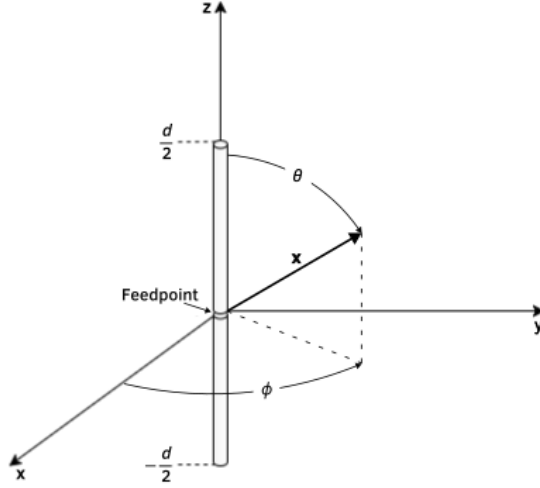


Figure 2.2 Geometrical arrangement of a linear, center-fed wire antenna with a feed-point indicated in the center. The feedpoint consists of a small gap providing current I_0 to the antenna.

2.1.2 Small Electric Dipoles

Wires that are too long to be modeled as an infinitesimal dipole, but short enough to be considered electrically small ($\lambda/50 < l \leq \lambda/10$), are classified as small physical dipoles [3, pp. 162-163]. They are a more accurate and useful representation of a linear wire antenna, and now investigated further.

A current I_0 is fed into the short, center-fed, linear antenna shown in Figure 2.1. The current along the antenna arms $I(z)$ linearly drops to zero [15, p. 412], as visualized in Figure 2.3. Mathematically, it is described by,

$$\mathbf{I}(z) = \hat{\mathbf{a}}_z I_0 \left(1 - \frac{2|z|}{d} \right). \quad (2.12)$$

This is different to the current distribution of the infinitesimal dipole. The capacitor-plates are therefore not needed in this model. Furthermore, charge accumulates along the antenna due to the linear drop of current \mathbf{I} . It is expressed as a charge per unit length ρ' , which is appropriate due to the thin wire. It is derived by the continuity equation $j\omega\rho = \nabla \cdot \mathbf{J}$, which leads to [15, pp. 410-412]

$$\rho' = \pm \frac{d}{dz} j \frac{I(z)}{\omega} = \pm j \frac{2I_0}{\omega d}. \quad (2.13)$$

ρ' is uniformly distributed along each antenna arm.

Next, the vector potential \mathbf{A} is determined using Equation 2.3. The calculations of \mathbf{A} simplify to [15, p. 410],

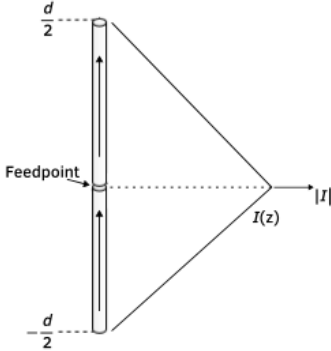


Figure 2.3 Current distribution across linear wire antenna. It has a maximum at the feedpoint, and drops to zero at points $d/2$ and $-d/2$.

$$\mathbf{A}(\mathbf{x}) = \hat{\mathbf{a}}_z \frac{\mu I_0 d}{8\pi r} e^{-jkr} \quad (2.14)$$

The formulation of \mathbf{A} now includes an additional factor of $1/2$ compared to the previously derived expression for infinitesimal dipoles in Equation 2.4. This factor arises from the integration of \mathbf{I} : when integrated over the interval $[-d/2, d/2]$, a linearly decreasing \mathbf{I} yields half the value obtained from a constant \mathbf{I} . For the same reason, the electric dipole moment \mathbf{m}_e is also reduced to half of that in Equation 2.2.

Furthermore, it makes sense to keep $\mathbf{x}' = \mathbf{0}$ for simplicity reasons. It has been shown, that this approximation is sufficient for large r , and the amplitude error remains negligible for small r [15, p. 409], [3, pp. 164-168].

The short physical electric dipole described in this section approximate the behavior of electrically short antennas. Special care must be taken of the excitation method and shape, as it influences the behavior [15, p. 413]. Additionally, any antenna investigated through this method must remain as small as possible compared to the wavelength λ , to reduce any analytical approximation errors.

2.2 Magnetic Dipoles

The magnetic dipole moment characterizes the strength of a magnetic source. A small current loop fed with a current I_0 can be used to model the magnetic dipole, as demonstrated in Figure 2.4. This relation holds as long as its overall length is smaller than a tenth of the wavelength ($2b\pi < \lambda/10$) and as long as the the wire is very thin [3, p. 231]. Furthermore, the radiation pattern of the magnetic dipole is equal to that of the electric dipole, with the role of the electric and magnetic fields interchanged [11, p. 254].

The magnetic dipole moment \mathbf{m}_m is given by

$$\mathbf{m} = I_m L \cdot \hat{\mathbf{a}}_z. \quad (2.15)$$

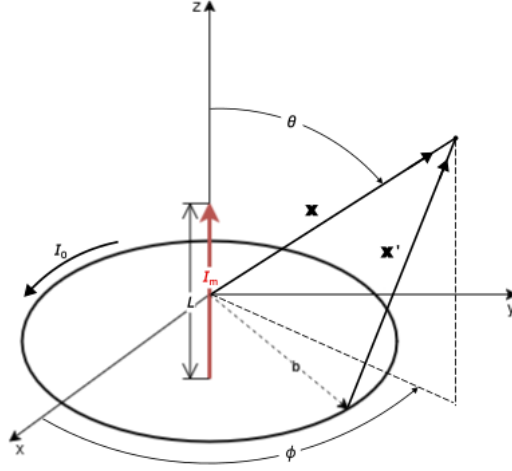


Figure 2.4 Geometrical arrangement of a current loop with radius b fed by a current I_0 , producing a magnetic dipole moment \mathbf{m}_m . Alternatively, a magnetic current I_m flows perpendicular to the loop's area along the distance L , which produces an equivalent magnetic dipole moment.

Furthermore, the magnetic current I_m and the electric current I_0 in the loop are related with [3, p. 237]

$$I_m L = j A \omega \mu_0 I_0 \quad (2.16)$$

with $A = b^2 \pi$ denoting the area of the current loop. Analogous to the separation distance d in the electric dipole, L is the length of the magnetic dipole. I_m and L may be used to model the magnetic dipole moment instead of the current loop, since the electric and magnetic field intensities \mathbf{E} and \mathbf{H} produced by the dipole are the same in both cases. This means, that the infinitesimal magnetic dipole has an equivalent behavior to the electrically small loop [3, p. 237]. \mathbf{E} and \mathbf{H} of the magnetic dipole moment or electrically small current loop are then determined with [3, p. 237]

$$E_r = E_\theta = 0, \quad (2.17a)$$

$$E_\phi = -j \frac{k I_m d \sin \theta}{4\pi r} \left[1 + \frac{1}{jkr} \right] e^{-jkr}, \quad (2.17b)$$

and,

$$H_r = \frac{I_m d \cos \theta}{2\pi r^2 \eta} \left[1 + \frac{1}{jkr} \right] e^{-jkr}, \quad (2.18a)$$

$$H_\theta = j \frac{k I_m d \sin \theta}{4\pi r \eta} \left[1 + \frac{1}{jkr} - \frac{1}{(kr)^2} \right] e^{-jkr}, \quad (2.18b)$$

$$H_\phi = 0. \quad (2.18c)$$

The complex power density \mathbf{W} can be derived analogous to the electric dipole case in Equation 2.9. For the magnetic dipole, the imaginary part of \mathbf{W} has the opposite sign compared to the electric dipole. This is the result of the near-field power being inductive in case of the magnetic dipole, while it is capacitive for the electric dipole. The complex power equals to

$$P_r = \eta \left(\frac{\pi}{12} \right) (ka)^4 |I_0|^2 \left[1 + j \frac{1}{(kr)^3} \right], \quad (2.19)$$

and its imaginary part is inductive [3, p. 238].

2.3 Radiated Field

2.3.1 Field regions

The field quantities \mathbf{E} and \mathbf{H} have been derived for an infinitesimal electric dipole in Equations (2.7a) to (2.7c) and Equations (2.8a) and (2.8b), further for an infinitesimal magnetic dipole in Equations (2.18a) to (2.18c) and Equations (2.17a) and (2.17b). They are valid everywhere except for the source region [3, p. 156].

The behavior of the fields depends on the distance r from the dipole. This dependence becomes evident by investigating the terms $1/(jkr)$ and $1/(kr)^2$ appearing in Equations (2.7a) to (2.7c) and Equations (2.8a) and (2.8b) for the infinitesimal electric dipole. For clarity, these terms are highlighted in the expression for E_θ in Equation (2.20), although they also partially appear in E_r and H_ϕ . They are denoted as Expression 1 and Expression 2, respectively:

$$E_\theta = j\eta \frac{kI_0 d \sin \theta}{4\pi r} \left[1 + \underbrace{\frac{1}{jkr}}_{\text{Expression 1}} - \underbrace{\frac{1}{(kr)^2}}_{\text{Expression 2}} \right] e^{-jkr}. \quad (2.20)$$

If the distance $r < \lambda/2\pi$ (or equivalently, $kr < 1$), then Expression 2 delivers the largest value in the brackets. Consequently, the energy stored in this region is predominantly imaginary. This region is referred to as the near-field region.

At distances $r > \lambda/2\pi$ ($kr > 1$), Expression 1 exceeds Expression 2 in magnitude, resulting in a larger real than imaginary part of the energy. This region is referred to as the intermediate-field region.

At larger distances $r \gg \lambda/2\pi$ ($kr \gg 1$) the energy is predominantly real, reflecting radiated energy propagating outward. This region is referred to as the far-field region.

At $r = \lambda/2\pi$ ($kr = 1$), Expression 1 and Expression 2 are of equal magnitude. This is marked as the radian distance [3, pp. 156-160]. The radian distance therefore represents an important transition point between field regions, where the behavior of the fields shifts.

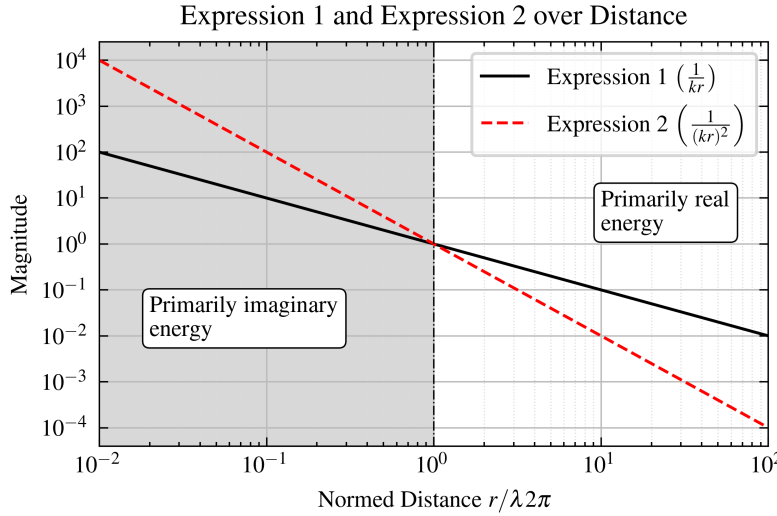


Figure 2.5 Behavior of Expression 1 and Expression 2 in Equation 2.20 over distance r . The distance r is normalized to the radian distance $\lambda/2\pi$. The magnitude of both expressions is normed to 1 at radian distance to improve comparison.

Figure 2.5 visualizes Expression 1 and Expression 2 over r . The analysis of the field regions presented here can be conducted analogously for both the small and infinitesimal magnetic dipole.

Antennas, which cannot be modeled as infinitesimal dipoles, such as the linear wire antenna, are surrounded by different field regions. They are shown in Figure 2.6. The far-field region contains mostly real energy, and the antenna may be most accurately approximated by an infinitesimal electric dipole. In the radiating near-field, the energy is largely real, but depends on the distance r . Lastly, in the reactive near-field the energy is mostly imaginary.

The far-field region starts at approximately r_2 and the radiating near-field at r_1 , which are defined as

$$r_1 = 0.62\sqrt{d^3/\lambda}, \quad (2.21a)$$

$$r_2 = 2d^2/\lambda. \quad (2.21b)$$

Here, d is the largest dimension of the antenna. In the case of the linear wire antenna, d is the wire length [3, pp. 165-170].

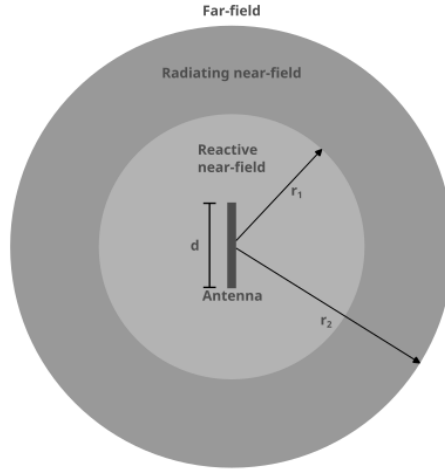


Figure 2.6 Field regions of an antenna, here specifically a linear wire antenna, although they are applicable for any antenna with dimension d .

2.3.2 Energy densities and reactances

The energy density is given by [11, p. 330]

$$w_{\text{em}} = \frac{1}{2} \left(\underbrace{\epsilon E^2}_{\text{Electric energy } w_e} + \underbrace{\frac{1}{\mu} B^2}_{\text{Magnetic energy } w_m} \right). \quad (2.22)$$

Integrating w_{em} over a volume yields the total electromagnetic energy within that volume. Similarly, integrating w_e gives the electric energy W_e , and w_m the magnetic energy W_m .

The reactance of an electrically short antenna directly relates to the electric and magnetic energies w_e, w_m , that it produces. The antennas's equivalent inductance and capacitance can be derived through [11, pp. 107, 328]

$$L = 2 \frac{W_m}{I^2}, \quad (2.23a)$$

$$C = 2 \frac{W_e}{V^2}. \quad (2.23b)$$

3 Guided Waves

3.1 Lorentz Reciprocity Theorem

Let two source pairs $\mathbf{J}_1, \mathbf{M}_1$ and $\mathbf{J}_2, \mathbf{M}_2$ exist in a volume V , bounded by the closed surface S . The medium in V is linear and isotropic. The source pairs generate fields $\mathbf{E}_1, \mathbf{H}_1$ and $\mathbf{E}_2, \mathbf{H}_2$, respectively, with the same frequency. The fields and source pairs can then be related with [3, p. 145, 8, p. 49]

$$-\nabla \cdot (\mathbf{E}_1 \times \mathbf{H}_2 - \mathbf{E}_2 \times \mathbf{H}_1) = \mathbf{E}_1 \cdot \mathbf{J}_2 + \mathbf{H}_2 \cdot \mathbf{M}_1 - \mathbf{E}_2 \cdot \mathbf{J}_1 - \mathbf{H}_1 \cdot \mathbf{M}_2. \quad (3.1)$$

Integrating Equation 3.1 over V , and converting the volume integral to a surface integral with the divergence theorem, leads to [3, p. 145, 8, p. 50]

$$\begin{aligned} & -\oint\!\oint_S (\mathbf{E}_1 \times \mathbf{H}_2 - \mathbf{E}_2 \times \mathbf{H}_1) \cdot d\mathbf{s}' \\ &= \iiint_V (\mathbf{E}_1 \cdot \mathbf{J}_2 + \mathbf{H}_2 \cdot \mathbf{M}_1 - \mathbf{E}_2 \cdot \mathbf{J}_1 - \mathbf{H}_1 \cdot \mathbf{M}_2) \cdot dv'. \end{aligned} \quad (3.2)$$

This integral equation relates the coupling of different source points. Additionally, if one of these sources is set to zero, the respective source point can serve as an observation point. Setting all sources to zero can be done to investigate source fields of a mode and their coupling to other modes in a waveguide, as the following example shows. Suppose the volume V does not contain sources $\mathbf{J}_1 = \mathbf{M}_1 = \mathbf{J}_2 = \mathbf{M}_2 = \mathbf{0}$. Then, the Lorentz Reciprocity theorem in differential and integral form results in [3, pp. 145-146]

$$\nabla \cdot (\mathbf{E}_1 \times \mathbf{H}_2 - \mathbf{E}_2 \times \mathbf{H}_1), \quad (3.3a)$$

$$\oint\!\oint_S (\mathbf{E}_1 \times \mathbf{H}_2 - \mathbf{E}_2 \times \mathbf{H}_1) \cdot d\mathbf{s}' = 0, \quad (3.3b)$$

which the modes in the waveguide must fulfill.

Another application arises when investigating a volume V confined by a perfectly conducting surface S , in which the linear current densities \mathbf{J}_1 and \mathbf{J}_2 flow. Because $\mathbf{n} \times \mathbf{E}_1 = \mathbf{n} \times \mathbf{E}_2 = \mathbf{0}$ along the surface S , the surface integral in Equation 3.2 vanishes, and

$$\mathbf{E}_1 \cdot \mathbf{J}_2 = \mathbf{E}_2 \cdot \mathbf{J}_1, \quad (3.4)$$

arise. This is the Rayleigh-Carson form of the Lorentz reciprocity theorem. It states that \mathbf{J}_1 generates \mathbf{E}_1 , which has components along \mathbf{J}_2 , that are equal to the same components of \mathbf{E}_2 along \mathbf{J}_1 , and vice versa [8, p. 50].

Concluding, the Lorentz Reciprocity theorem is useful to derive reciprocal aspects of waveguides, finding orthogonal properties of modes, investigating fields generated by currents and dipole moments in waveguides [8, p. 50], among several other examples. This theorem will be employed often throughout the remainder of this thesis.

3.2 Green's Function

3.2.1 Scalar Green's Function

The Green's function describes the response of a linear differential operator L to a point source of unit strength. It is explained briefly in the following with an example of solving

the Poisson's equation with boundary conditions, since this concept will be used in further analysis. The general form for a Green's function of a given problem is

$$LG(\mathbf{x}, \mathbf{x}') = -\delta(\mathbf{x} - \mathbf{x}'). \quad (3.5)$$

A point source of unit strength is generally modeled with a delta function δ at a certain point in one-dimensional space. In multi-dimensional space, a product of delta-functions are used.

Once Equation 3.5 is solved for a point source of unit strength, and the Green's function G of this specific problem is known, it can be used to solve for any combination of point sources f to solve for an input function u ,

$$Lu(\mathbf{x}) = f(\mathbf{x}), \quad (3.6)$$

This is done through superposition through point sources of unit strength, as in

$$u(\mathbf{x}) = \iiint_V G(\mathbf{x}, \mathbf{x}') f(\mathbf{x}') dv'. \quad (3.7)$$

The integrands are the source point variables x', y', z' .

One application of the Green's function is solving the Poisson's equation. The scalar potential ϕ can be calculated from a density of charge distribution ρ by using the Green's function of this specific problem. If there are no boundaries present, it takes the form

$$\nabla^2 \phi = -\frac{\rho}{\epsilon}, \quad (3.8a)$$

$$\phi(\mathbf{x}) = \frac{1}{4\pi\epsilon} \iiint_V \frac{\rho(\mathbf{x}')}{|\mathbf{x} - \mathbf{x}'|} dv', \quad (3.8b)$$

where ϵ is the permittivity of the medium.

The Green's function for this problem equals $G(\mathbf{x}, \mathbf{x}') = \frac{1}{4\pi|\mathbf{x} - \mathbf{x}'|}$, and represents the potential at position \mathbf{x} created by a unit point charge at point \mathbf{x}' . In this case, the input function $u = \phi$ and the source function $f = -\rho/\epsilon_0$.

Different volumes of interest V_1, V_2, \dots, V_n can be connected by applying boundary conditions on their surrounding surfaces S_1, S_2, \dots, S_n . Applying Green's second identity on the Poisson's equation enables enforcing such a boundary condition upon the surrounding surface S of a volume V ,

$$\iiint_V (\phi \nabla_{\mathbf{x}'}^2 G - G \nabla_{\mathbf{x}'}^2 \phi) dv' = \iint_S \left(G \frac{\partial \phi}{\partial \mathbf{n}} - \phi \frac{\partial G}{\partial \mathbf{n}} \right) ds'. \quad (3.9)$$

The vector \mathbf{n} is normal to S . The operator $\nabla_{\mathbf{x}'}^2$ differentiates with respect to the source vector \mathbf{x}' due to x', y', z' being the integrands. Inserting $\nabla^2\phi = -\rho/\epsilon$ from Equation 3.8a and $\nabla^2G = -\delta$ from Equation 3.5 leads to

$$\phi = \frac{1}{\epsilon} \iiint_V \rho(\mathbf{x}') G(\mathbf{x}, \mathbf{x}') \cdot d\mathbf{v}' + \oint_S \left(\phi \frac{\partial G}{\partial \mathbf{n}} - G \frac{\partial \phi}{\partial \mathbf{n}} \right) d\mathbf{s}' \quad (3.10)$$

ϕ or its normal derivative to the surface $\partial\phi/\partial\mathbf{n}$ can be forced on the boundary. If only one of those two expressions is known on the boundary surface, the Green's function may be modified such that the unknown expression vanishes. If ϕ is defined on the whole boundary, it satisfies Dirichlet boundary conditions. On the other hand, if $\partial\phi/\partial\mathbf{n}$ is defined on the whole boundary, it satisfies Neumann boundary conditions [8, pp. 55-59].

3.2.2 Dyadic Green's Function

While the scalar Green's function is useful for solving one-dimensional differential equations, the dyadic Green's function $\bar{\mathbf{G}}$ is more suitable for three-dimensional problems. It relates a vector source with a vector response, which is necessary when solving the vector Helmholtz equation in

$$\nabla^2 \mathbf{A} + k^2 \mathbf{A} = -\mu \mathbf{J}. \quad (3.11)$$

When replacing $\mu \mathbf{J}$ by an unit vector source $(\hat{\mathbf{a}}_x + \hat{\mathbf{a}}_y + \hat{\mathbf{a}}_z) \delta(\mathbf{x} - \mathbf{x}')$, the solution for \mathbf{A} of Equation 3.11 in free-space is

$$(\hat{\mathbf{a}}_x + \hat{\mathbf{a}}_y + \hat{\mathbf{a}}_z) \frac{e^{-jk|\mathbf{x}-\mathbf{x}'|}}{4\pi|\mathbf{x}-\mathbf{x}'|}. \quad (3.12)$$

This is a vector Green's Function by definition [8, pp. 91-92].

Each component of the current distribution \mathbf{J} generates fields through a linear relation. This relationship can effectively be represented by dyadics, which are linear mappings between vectors. The dyadic Green's function is therefore introduced and defined as

$$\begin{aligned} \bar{\mathbf{G}} = & G_{xx} \hat{\mathbf{a}}_x \hat{\mathbf{a}}_x + G_{xy} \hat{\mathbf{a}}_x \hat{\mathbf{a}}_y + G_{xz} \hat{\mathbf{a}}_x \hat{\mathbf{a}}_z + \\ & G_{yx} \hat{\mathbf{a}}_y \hat{\mathbf{a}}_x + G_{yy} \hat{\mathbf{a}}_y \hat{\mathbf{a}}_y + G_{yz} \hat{\mathbf{a}}_y \hat{\mathbf{a}}_z + \\ & G_{zx} \hat{\mathbf{a}}_z \hat{\mathbf{a}}_x + G_{zy} \hat{\mathbf{a}}_z \hat{\mathbf{a}}_y + G_{zz} \hat{\mathbf{a}}_z \hat{\mathbf{a}}_z \end{aligned}$$

Each component of the current vector \mathbf{J} is associated with one unit vector of the Green's function, i.e. J_x with $\hat{\mathbf{a}}_x$, J_y with $\hat{\mathbf{a}}_y$ and J_z with $\hat{\mathbf{a}}_z$ [8, p. 92]. Consequently, the field generated by a current component in a given direction is determined by the corresponding column of the dyadic Green's function. For example, if only a current component J_x is present, the field components A_x , A_y , and A_z are obtained from the Green's functions elements G_{xx} , G_{yx} and G_{zx} .

The dyadic Green's function is defined as the solution of

$$\nabla^2 \bar{\mathbf{G}}(\mathbf{x}, \mathbf{x}') + k^2 \bar{\mathbf{G}} = -\bar{\mathbf{I}}\delta(\mathbf{x} - \mathbf{x}'). \quad (3.13)$$

In free space, a commonly used form of the dyadic Green's function is given by [8, p.92]

$$\bar{\mathbf{G}}(\mathbf{x}, \mathbf{x}') = \bar{\mathbf{I}} \frac{e^{-jk|\mathbf{x}-\mathbf{x}'|}}{4\pi|\mathbf{x}-\mathbf{x}'|}, \quad (3.14)$$

where $\bar{\mathbf{I}}$ is an unit dyadic. The free-space case is presented here to provide an overview. Dyadic Green's functions can also be derived for bounded geometries, such as waveguides, by implementing appropriate boundary conditions.

The fields \mathbf{A} generated by arbitrary \mathbf{J} can be expressed with the dyadic Green's function as

$$\mathbf{A}(\mathbf{x}) = \mu \iiint_V \bar{\mathbf{G}}(\mathbf{x}, \mathbf{x}') \mathbf{J}(\mathbf{x}') d\mathbf{x}'. \quad (3.15)$$

Each component of \mathbf{J} drives a combination of components in \mathbf{A} . Dyadics capture this component-wise coupling and simplify the notation [8, p. 92].

3.3 Modes in Waveguides

3.3.1 Rectangular Waveguides as non-TEM structures

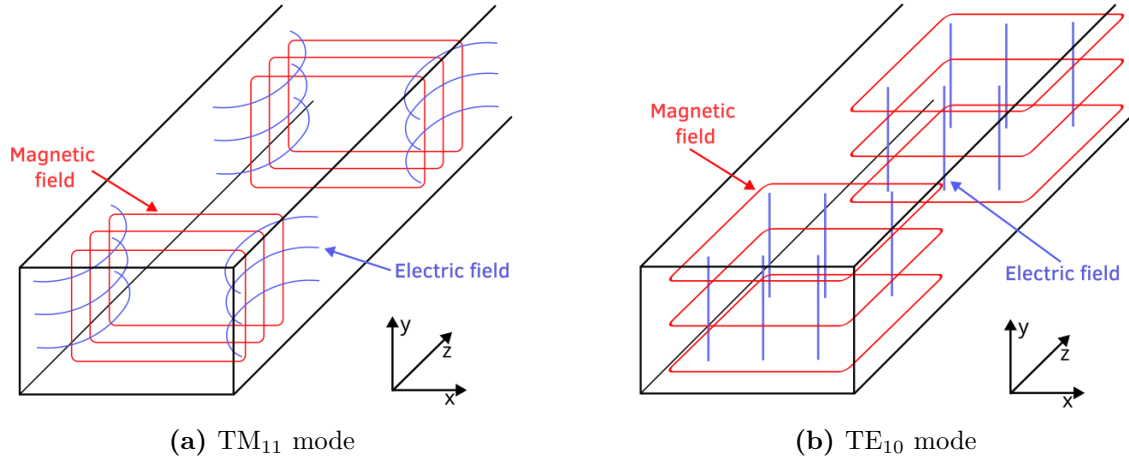


Figure 3.1 The electric and magnetic fields of each the first dominant TE and TM mode in a hallow rectangular waveguide with perfectly conducting walls.

A hollow rectangular waveguide with perfectly conducting walls do not support the propagation of the TEM mode. This can be shown directly from Maxwell's equation, as done in [11, pp. 425-427]. The first two dominant modes are demonstrated in Figure 3.1. The electric field intensity \mathbf{E} and magnetic field intensity \mathbf{H} are defined as

$$\mathbf{E} = (E_{0,x} \cdot \hat{\mathbf{a}}_x + E_{0,y} \cdot \hat{\mathbf{a}}_y + E_{0,z} \cdot \hat{\mathbf{a}}_z) e^{-jkz}, \quad (3.16a)$$

$$\mathbf{H} = (H_{0,x} \cdot \hat{\mathbf{a}}_x + H_{0,y} \cdot \hat{\mathbf{a}}_y + H_{0,z} \cdot \hat{\mathbf{a}}_z) e^{-jkz}. \quad (3.16b)$$

Using Faraday's and Ampère-Maxwell law transforms Equations (3.16a) to (3.16b) to

$$\nabla \times \mathbf{E} = \begin{pmatrix} \frac{\partial}{\partial y} E_z - jk E_y \\ jk E_x - \frac{\partial}{\partial x} E_z \\ \frac{\partial}{\partial x} E_y - \frac{\partial}{\partial y} E_x \end{pmatrix} = \begin{pmatrix} -j\omega B_x \\ -j\omega B_y \\ -j\omega B_z \end{pmatrix}, \quad (3.17a)$$

$$\nabla \times \mathbf{B} = \begin{pmatrix} \frac{\partial}{\partial y} B_z - jk B_y \\ jk B_x - \frac{\partial}{\partial x} B_z \\ \frac{\partial}{\partial x} B_y - \frac{\partial}{\partial y} B_x \end{pmatrix} = \begin{pmatrix} \frac{j\omega}{\mu\epsilon} E_x \\ \frac{j\omega}{\mu\epsilon} E_y \\ \frac{j\omega}{\mu\epsilon} E_z \end{pmatrix}. \quad (3.17b)$$

For a TEM mode, the longitudinal field components vanish $E_z = H_z = 0$. Under this assumption, Equations (3.17a) to (3.17b) together with Gauss' law and Faraday's law reduce to the following conditions for \mathbf{E} components:

$$\frac{\partial}{\partial x} E_x + \frac{\partial}{\partial y} E_y = 0 \quad \text{Derived out of Gauss' law,} \quad (3.18)$$

$$\frac{\partial}{\partial y} E_x - \frac{\partial}{\partial x} E_y = 0 \quad \text{Derived out of Faraday's law.} \quad (3.19)$$

The derived Equations (3.18) to (3.19) cannot fulfill any boundary conditions imposed by the rectangular waveguide. Therefore, a TEM mode cannot propagate.

3.3.2 TEM mode in the TEM cell

Opposed to the rectangular waveguide, a TEM cell conducts TEM waves. Further, the TEM mode is necessarily excited by the geometry of the TEM cell, hence this mode is called essential. The higher order TE and TM modes, which are only excited due to non-uniformity of the TEM cell, are called non-essential modes [17].

The TEM mode in the TEM cell is derived by a procedure presented in [33, 35]. It consists of finding the Green's function of both the TE and TM modes transverse field components H_z, E_z in a rectangular waveguide. The Green's function fulfills the wave equations and boundary conditions of the waveguide, constructed as discussed in Section 3.2.1, with

$$(\nabla^2 + k_{0,t}^2) G(\mathbf{x}_t, \mathbf{x}'_t) = -\delta(\mathbf{x}_t - \mathbf{x}'_t), \quad (3.20a)$$

$$\frac{\partial G(\mathbf{x}_t, \mathbf{x}'_t)}{\partial \mathbf{n}} = 0. \quad (3.20b)$$

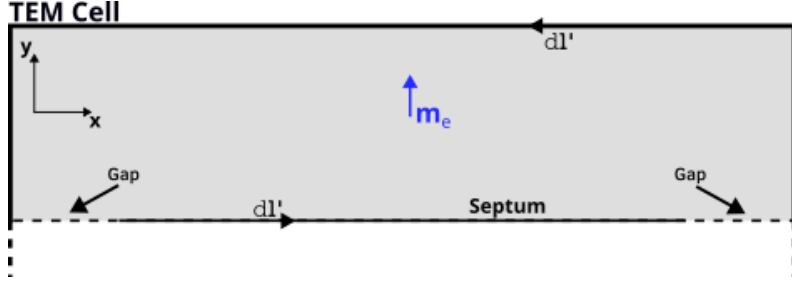


Figure 3.2 The Green's function in this analysis solves the fields in the cross section surface S of the TEM cell1, which is colored in light gray and bounded by l . The source exciting these fields is a centered, electric dipole moment \mathbf{m}_e .

The wave number is separated in a transversal and a longitudinal component $k_0^2 = k_{0,t}^2 + k_{0,z}^2$. Equation 3.20b express the boundary condition on the perfectly conducting walls and septum of the TEM cell, as well as for the gaps, as illustrated in Figure 3.2. The source points are denoted with $\mathbf{x}'_t = (\hat{\mathbf{a}}_x x' + \hat{\mathbf{a}}_y y')$ and the observation points with $\mathbf{x}_t = (\hat{\mathbf{a}}_x x + \hat{\mathbf{a}}_y y)$. They are transformed, such that they have a dependence on the wave number k instead of a z -dependence. This significantly facilitates the derivation of the Green's function, since only a two-dimensional surface has to be considered.

The source exciting the waveguide is assumed to be an infinitesimal electric dipole moment centrally located and oriented along the y -axis. Solving for H_z and applying Green's second identity yields

$$\int_l \left(G(\mathbf{x}_t, \mathbf{x}'_t) \frac{\partial H_z(\mathbf{x}_t)}{\partial \mathbf{n}} - H_z(\mathbf{x}_t) \frac{\partial G(\mathbf{x}_t, \mathbf{x}'_t)}{\partial \mathbf{n}} \right) d\mathbf{l}' = \quad (3.21)$$

$$= H_z(\mathbf{x}_t) - \int_S J_y(\mathbf{x}'_t) \frac{\partial G(\mathbf{x}_t, \mathbf{x}'_t)}{\partial \mathbf{x}'_t} d\mathbf{S}', \quad (3.22)$$

where S is the surface of the waveguide cross section, and l is its boundary. Applying the boundary condition on the perfectly conducting septum and walls, leaves the boundary integrals along the gaps. Further, inserting the electric dipole in Equation 3.22 and forcing H_z to be continuous across the gaps leads to

$$\int_{\text{gaps}} G(\mathbf{x}_t, \mathbf{x}'_t) \frac{\partial H_z(x', 0)}{\partial y'} dx' = -\mathbf{m}_e \frac{\partial G(\mathbf{x}_t, \mathbf{x}'_t)}{\partial \mathbf{x}'_t}. \quad (3.23)$$

Solving for the Green's function G yields a solution for the magnetic longitudinal field intensity H_z of the TE mode. The same process can be applied to solve for the electric longitudinal field intensity E_z of the TM mode. The total field distribution is a superposition of the TE and TM mode fields, which finally demonstrates the excitation of the TEM mode. The transversal fields E_t, H_t relate to H_z with

$$E_t(\mathbf{x}_t) = \frac{j\omega\mu_0}{k_{0,t}^2} \frac{\partial H_z(\mathbf{x}_t)}{\partial \mathbf{t}} \times \hat{\mathbf{a}}_z, \quad (3.24a)$$

$$H_t(\mathbf{x}_t) = \frac{jk_{0,z}}{k_{0,t}^2} \frac{\partial H_z(\mathbf{x}_t)}{\partial \mathbf{t}}, \quad (3.24b)$$

and to E_z with

$$E_t(\mathbf{x}_t) = \frac{jk_{0,z}}{k_{0,t}^2} \frac{\partial E_z(\mathbf{x}_t)}{\partial \mathbf{t}}, \quad (3.25a)$$

$$H_t(\mathbf{x}_t) = \frac{-j\omega\epsilon_0}{k_{0,t}^2} \frac{\partial E_z(\mathbf{x}_t)}{\partial t} \times \hat{\mathbf{a}}_z, \quad (3.25b)$$

where \mathbf{t} denotes the transversal unit vector.

3.3.3 Higher-order modes

The TEM cell under investigation has a width of $a = 40$ mm and a height of $b = 24$ mm with a gap length of $g = 5$ mm, which is shown in ???. For a thin septum ($t/b \ll 0.1$), the cut-off frequency f_c of modes with n-even subscripts, i.e. $\text{TE}_{m,2n}$ and $\text{TM}_{m,2n}$ modes, is approximated as [34]

$$f_c = \frac{c}{2} \sqrt{\left(\frac{m}{a}\right)^2 + \left(\frac{n}{b}\right)^2}. \quad (3.26)$$

- f_c : cutoff frequency of the mode $\text{T}_{m,2n}$
- c : speed of light in the medium
- a : width of the TEM cell
- b : height of the TEM cell
- m : mode index in the a -direction (integer, $m \geq 0$)
- n : mode index in the b -direction (integer, $n \geq 0$)

Equation 3.26 is also valid for cut-off frequencies f_c of higher-order modes in rectangular waveguides [34].

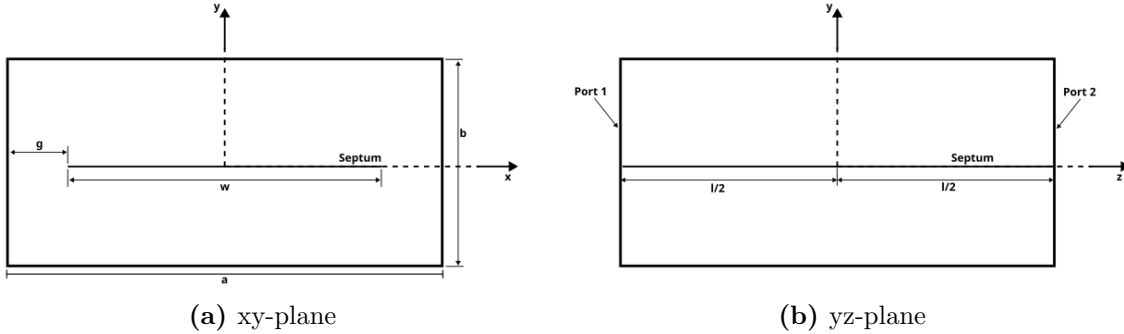


Figure 3.3 Geometrical arrangement of the TEM cell, demonstrated with cross sections in the xy-plane and the yz-plane.

Using numerical analysis, the forward transmission coefficients between the output ports of the TEM cell S_{12} , is computed and shown in Figure 3.4. The cut-off frequency f_c is defined as the lowest frequency at which undisturbed mode propagation occurs, corresponding to $S_{12} = 0 \text{ dB}$. The numerically determined cutoff frequency of the TE_{10} mode, $f_{c,10} = 3.75 \text{ GHz}$, is in agreement with the analytically obtained value given by Equation 3.26.

Analytical approximations for the cut-off frequencies of modes with n-odd subscripts are presented in [38]. For this thesis, the cut-off frequency of the next higher order mode TE_{01} is determined analytically in Figure 3.4 as $f_{c,01} = 3.12 \text{ GHz}$.

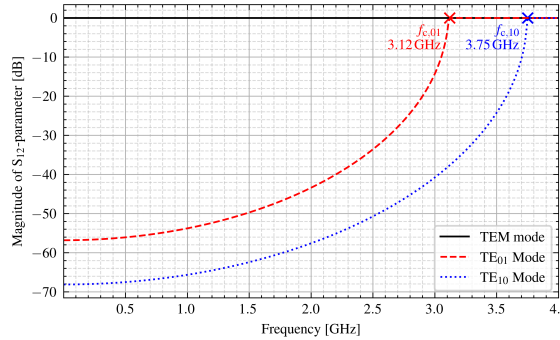


Figure 3.4 Forward transmission coefficients S_{12} of the TEM, TE_{01} and TE_{10} modes in the TEM cell over frequency.

A TEM cell incorporates tapered sections at its output ports, through which the TEM mode propagates with negligible reflection. In contrast, higher-order TE and TM modes reflect at the tapered transitions. Consequently, the TEM cell behaves as a high-Q cavity resonator for these modes, with resonance frequencies occurring at an electrical length of $\frac{\lambda}{4}$ and its multiples. Numerical investigations of TEM cell simulation models that include tapered sections are presented in [17], while analytical approximations of the resonance frequencies for different modes in a TEM cell are given in [34].

Wave propagating in the TEM mode may excite higher order TE and TM modes due to material discontinuities or finite conductivity of the conducting plates [18]. Such discontinuities require the electric and magnetic field to have a component in the direction of propagation, thereby exciting TE and TM modes. This leads to measurement uncertainties that are not present in numerical analysis.

Among the higher-order modes, the TE_{10} and TE_{01} modes are non-essential modes with the lowest cutoff frequencies. Their transverse electric field distributions are illustrated in Figure 3.5.

Table 3.1 shows some cut-off frequencies of these modes for different TEM cell dimensions. The focus for the remainder of this thesis lays on a TEM cell with the dimensions $a = 40 \text{ mm}$ and $b = 24 \text{ mm}$, for which the characteristic impedance of the output ports equals $Z_w = 50 \Omega$.

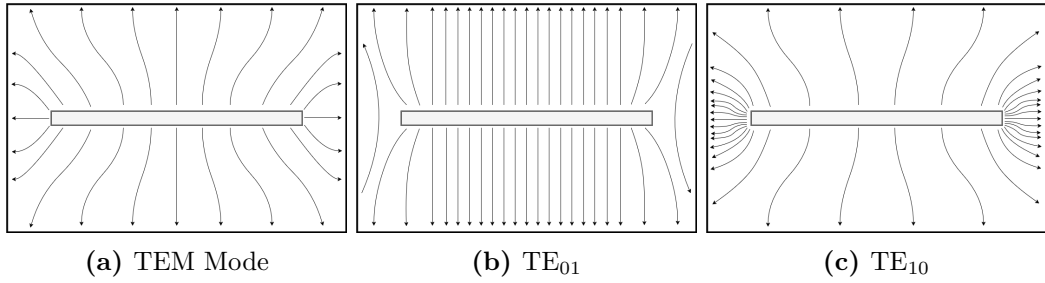


Figure 3.5 Transversal electric fields in cross section of TEM cell

a (mm)	b (mm)	TE ₀₁ f_c (GHz)	TE ₁₀ f_c (GHz)
80	24	1.89	2.05
40	24	3.17	3.76
40	48	2.10	3.76

Table 3.1 Cut-off frequencies of higher order modes at different TEM cell dimensions. The TE₁₀-mode is independent of the height b of the TEM cell, as would be the case in a rectangular waveguide. Both the TE₁₀-mode and the TE₀₁-mode are dependent on the width a .

3.3.4 Field distributions

The normalized electric field intensity of the TEM mode is given as $\mathbf{e}_{\text{TEM}}^{\pm} = e_{\text{TEM},x}^{\pm} \cdot \hat{\mathbf{a}}_y + e_{\text{TEM},y}^{\pm} \cdot \hat{\mathbf{a}}_x + e_{\text{TEM},z}^{\pm} \cdot \hat{\mathbf{a}}_z$ and normalized to \sqrt{W} . The x - and z -component of $\mathbf{e}_{\text{TEM},x}^{\pm}$ is analytically approximated by

$$e_{\text{TEM},x}^{\pm} = \frac{4}{a} Z_w^{1/2} \sum_{m_o=1}^{\infty} \frac{\sinh M(b/2 - py)}{\sinh Mb/2} \cdot \sin Mx \sin Ma/2 J_0(Mg), \quad (3.27a)$$

$$e_{\text{TEM},y}^{\pm} = p \frac{4}{a} Z_w^{1/2} \sum_{m_o=1}^{\infty} \frac{\cosh M(b/2 - py)}{\sinh Mb/2} \cdot \cos Mx \sin Ma/2 J_0(Mg). \quad (3.27b)$$

Z_w denotes the characteristic impedance of the TEM cell output port, a its width and b its height. The sign-function is defined as $p = 1$ above the septum and $p = -1$ below it. The parameter $M = m_o\pi/2a$, and g represented the distance of the gap between the septum and the conducting wall. The index $m_o = 1, 3, 5, \dots$ iterates over odd integers. Both expressions are derived in [35] using the procedure described in Section 3.3.2. Analytical expression of higher-order modes are provided in [33] and not investigated further in this thesis.

In case of higher-order modes propagating, the analysis of the field distribution is conducted with the following assumptions. Each of the propagating modes is assumed to be orthogonal to each other,

$$\iint \mathbf{e}_n^\pm \times \mathbf{h}_m^\pm d\mathbf{s}' = 0 \quad \text{if } n \neq m, \quad (3.28)$$

with \mathbf{e}_n^\pm and \mathbf{h}_n^\pm being the function vectors of the electric and magnetic field in transverse direction [8]. This indicates that the modes do not couple with each other, which is the case in an uniform waveguide with perfectly conducting walls, as discussed in Section 3.3.3. Furthermore, each mode is normalized to \sqrt{W} as shown by

$$\iint \mathbf{e}_n^\pm \times \mathbf{h}_n^\pm d\mathbf{s}' = 1. \quad (3.29)$$

The radiated fields can then be described by a summation of normal modes, as in

$$\mathbf{E}^+ = \sum_n a_n \mathbf{e}_n^+, \quad (3.30a)$$

$$\mathbf{H}^+ = \sum_n a_n \mathbf{h}_n^+. \quad (3.30b)$$

And the fields propagating along the negative z-direction are expressed by [8, p. 360]

$$\mathbf{E}^- = \sum_n b_n \mathbf{e}_n^-, \quad (3.31a)$$

$$\mathbf{H}^- = \sum_n b_n \mathbf{h}_n^-, \quad (3.31b)$$

where \mathbf{h}_n^\pm is the normalized magnetic field intensity.

The coefficients a_n and b_n have units of \sqrt{W} and weight \mathbf{e}_n^\pm and \mathbf{h}_n^\pm of each mode. The field intensities at the outputs \mathbf{E}^\pm and \mathbf{H}^\pm are therefore decomposed into several propagating mode fields, each weighted with the corresponding coefficients. The derivation of a_n and b_n is discussed in Section 3.4.

The normalized magnetic field intensity \mathbf{h}_n^\pm is derived in an analogous manner to \mathbf{e}_n^\pm . For the TEM mode, $\mathbf{h}_{\text{TEM}}^\pm$ can also be directly obtained from $\mathbf{e}_{\text{TEM}}^\pm$ with

$$\mathbf{h}_{\text{TEM}}^\pm = \pm \frac{1}{\eta_0} \hat{\mathbf{a}}_z \times \mathbf{e}_{\text{TEM}}^\pm, \quad (3.32)$$

where $\eta_0 \approx 377 \Omega$ is the free-space wave impedance.

The normalized electric field intensity $\mathbf{e}_{\text{TEM}}^\pm$ of the TEM mode is a key parameter for determining the coupling between a source and the output ports of the TEM cell, as derived using the Lorentz reciprocity theorem discussed in Section 3.1. For example, Figure 3.6a shows the output power generated by an electric dipole moment \mathbf{m}_e oriented

along the y -direction. The dipole is displaced along the x -axis at the center height between the septum and the upper wall of the TEM cell, which has a width of $a = 40$ mm and a height of $b = 24$ mm.

The normalized electric field component in the y -direction $e_{\text{TEM},y}^{\pm}$ reaches its maximum magnitude at the center of the TEM cell, according to Equation 3.27b. The integral form of the Lorentz reciprocity theorem in Equation 3.2 states that this results in the largest output power. This behavior is confirmed by the results shown in Figure 3.6a. Analogously, the output power shown in Figure 3.6b is largest close to the TEM cell wall, if the dipole moment is oriented in x -direction. Analysis of the field distribution is therefore useful to explain coupling behavior of electrically small antennas or dipole moments displaced within the TEM cell.

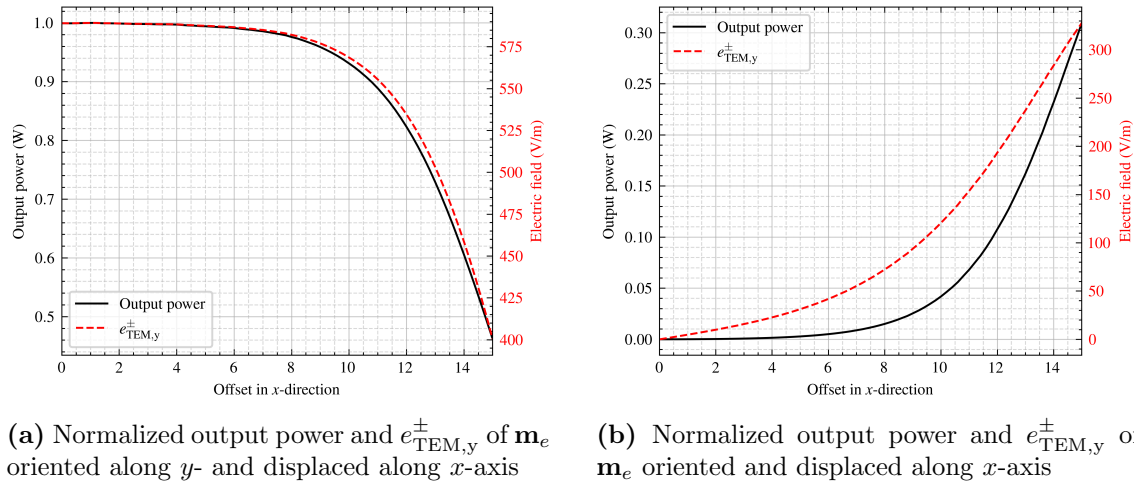


Figure 3.6 Output power and e_{TEM}^{\pm} for different electric dipole moment positions and orientations.

For this reason, Figure 3.7 shows the normalized electric field intensity in the TEM cell for both the x - and y -direction.

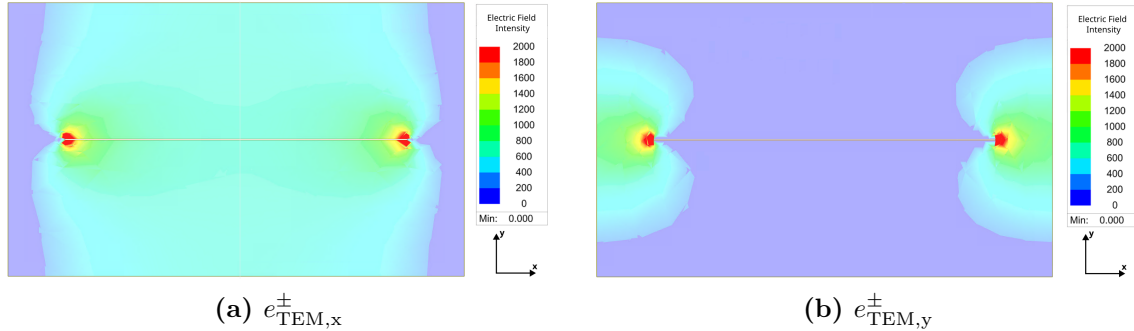


Figure 3.7 The normalized electric field distribution e_{TEM}^{\pm} in the TEM cell excited with an input power of 1/2 W at a frequency of 3 GHz.

Hier würde ich gerne eine Tabelle mit Messwerten des normalisierten elektrischen Feldes in der TEM Zelle einfügen, wie es in [35] getan wurde

3.4 Radiating Sources in TEM Cells

3.4.1 Arbitrary source

Suppose a current \mathbf{J}_1 excites the TEM cell, as shown in Figure 3.8. Normally, such a current would require external fields to drive it, however, these are neglected here. Only the fields \mathbf{E} and \mathbf{H} radiated by \mathbf{J}_1 are considered. These fields satisfy Maxwell's equations: [8, p. 360]

$$\nabla \times \mathbf{E} = -j\omega\mu_0\mathbf{H}, \quad (3.33a)$$

$$\nabla \times \mathbf{H} = j\omega\epsilon_0\mathbf{E} + \mathbf{J}_1. \quad (3.33b)$$

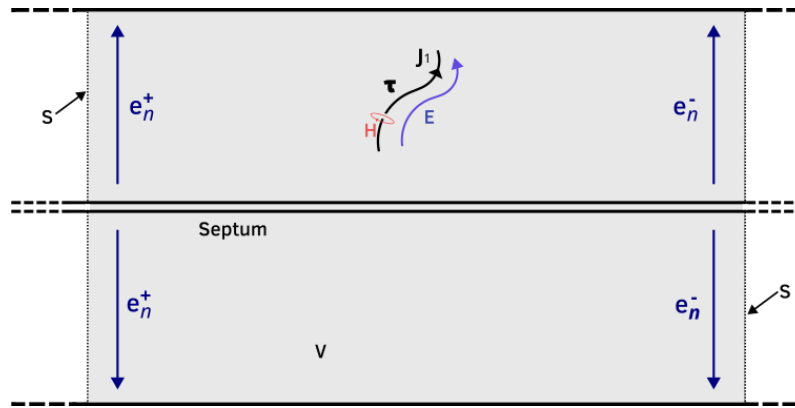


Figure 3.8 TEM cell with an arbitrary current source \mathbf{J}_1 along the curve τ . \mathbf{E} and \mathbf{H} are the field intensities induced by the current. \mathbf{e}_n^+ and \mathbf{e}_n^- are outgoing fields towards both output ports of the TEM cell of arbitrary form. \mathbf{s} indicates the surface, and V the volume of the domain in question.

Applying the integral form of the Lorentz reciprocity theorem in Equation 3.2 with $\mathbf{J}_2 = \mathbf{M}_1 = \mathbf{M}_2 = 0$ yields

$$\iint_S (\mathbf{e}_n^\pm \times \mathbf{H} - \mathbf{E} \times \mathbf{h}_n^\pm) \cdot d\mathbf{s}' = \iiint V \mathbf{J}_1 \cdot \mathbf{e}_n^\pm dv'. \quad (3.34)$$

Using the modal expansions Equations (3.30a) and (3.30b), Equations (3.31a) and (3.31b) for the fields \mathbf{E} and \mathbf{H} radiated by \mathbf{J}_1 lead to

$$\begin{aligned}
& \oint_S (\mathbf{e}_n^+ \times \mathbf{H} - \mathbf{E} \times \mathbf{h}_n^+) \cdot d\mathbf{s}' = \\
&= \oint_S (\mathbf{e}_n^+ \times \sum_m a_m \mathbf{h}_m^+ - \sum_m a_m \mathbf{e}_m^+ \times \mathbf{h}_n^+) \cdot d\mathbf{s}' \\
&= \sum_m a_m \oint_S (\mathbf{e}_n^+ \times \mathbf{h}_m^+ - \mathbf{e}_m^+ \times \mathbf{h}_n^+) \cdot d\mathbf{s}'.
\end{aligned} \tag{3.35}$$

Due to the orthogonal property of Equation 3.28 and the normalization in Equation 3.29, the coefficients of each mode can be evaluated separately with

$$\begin{aligned}
& \oint_S (\mathbf{e}_n^+ \times \mathbf{H} - \mathbf{E} \times \mathbf{h}_n^+) \cdot d\mathbf{s}' = \\
&= a_n \oint_S (\mathbf{e}_n^+ \times \mathbf{h}_n^+ - \mathbf{e}_n^+ \times \mathbf{h}_n^+) \cdot d\mathbf{s}' = -2a_n.
\end{aligned} \tag{3.36}$$

The coefficient b_n of the fields \mathbf{e}_n^- and \mathbf{h}_n^- are evaluated in the same manner.

Assuming only the TEM mode can propagate, combining Equation 3.29 with the fields \mathbf{e}_{TEM} and \mathbf{h}_{TEM} with their respective coefficients a_{TEM} , b_{TEM} leads to [37]

$$P_{\text{out1}} = \iint_S \langle \mathbf{S} \rangle \cdot d\mathbf{s}' = \iint_S \frac{1}{2} \Re\{(a \cdot \mathbf{e}_{\text{TEM}}^\pm) \times (a \cdot \mathbf{h}_{\text{TEM}}^\pm)^*\} \cdot d\mathbf{s}' = \frac{|a_{\text{TEM}}|^2}{2}, \tag{3.37a}$$

$$P_{\text{out2}} = \iint_S \langle \mathbf{S} \rangle \cdot d\mathbf{s}' = \iint_S \frac{1}{2} \Re\{(b \cdot \mathbf{e}_{\text{TEM}}^\pm) \times (b \cdot \mathbf{h}_{\text{TEM}}^\pm)^*\} \cdot d\mathbf{s}' = \frac{|b_{\text{TEM}}|^2}{2}. \tag{3.37b}$$

The Poynting vector $\langle \mathbf{S} \rangle$ of the TEM mode in Equations (3.37a) to (3.37b) does not have an imaginary component,

$$\langle \mathbf{S} \rangle = \mathbf{e}_{\text{TEM}}^\pm \times \mathbf{h}_{\text{TEM}}^\pm = \Re\{\mathbf{e}_{\text{TEM}}^\pm \times (\mathbf{h}_{\text{TEM}}^\pm)^*\}. \tag{3.38}$$

Equations (3.37a) to (3.37b) demonstrate that the coefficients a_{TEM} and b_{TEM} are directly related to the output power. Consequently, the output power can be directly linked to the electric and magnetic field distribution of the TEM mode, and vice versa.

3.4.2 Equivalent dipole moments

Equations (2.2) and (3.34) relate the electric dipole moment \mathbf{m}_e with a given source current \mathbf{J}_1 flowing through an infinitesimal wire, yielding [31]

$$\begin{pmatrix} a_n \\ b_n \end{pmatrix} = -\frac{1}{2} \mathbf{m}_e \cdot \mathbf{e}_n^\pm. \tag{3.39}$$

If this arbitrary current distribution forms an infinitesimal loop, the source can be represented by a magnetic dipole moment \mathbf{m}_m . This leads to [8]

$$\begin{aligned} \begin{pmatrix} a_n \\ b_n \end{pmatrix} &= - \oint_C \mathbf{e}_n^\pm dl \\ &= - \iint_S \nabla \times \mathbf{e}_n^\pm d\mathbf{s}' \\ &= i\omega\mu_0 \iint_S \mathbf{h}_n^\pm \cdot d\mathbf{s}' \\ &= i\omega\mu_0 \mathbf{m}_m \mathbf{h}_n^\pm \end{aligned} \quad (3.40)$$

This formulation assumes, that the magnetic field strength \mathbf{h}^\pm does not change over the loop area. This is the case for electrically small loops. Otherwise, the magnetic field strength \mathbf{h}^\pm must be considered in the integration process of Equation 3.40 [8].

If several modes are propagating, it is useful to determine the coefficients a_n and b_n weighting the modes in Equations (3.30a) to (3.31b). In this case, the orthogonality property in Equation 3.28 can be used to derive [8]

$$2a_n = - \int_C \boldsymbol{\tau} \cdot \mathbf{e}_n^- dl, \quad (3.41a)$$

$$2b_n = \int_C \boldsymbol{\tau} \cdot \mathbf{e}_n^+ dl. \quad (3.41b)$$

The wire follows the curve C , and $\boldsymbol{\tau}$ is the tangential vector along that curve.

In the presence of both a magnetic and an electric dipole moment, their contributions can be summed, resulting in [31]

$$\begin{pmatrix} a_n \\ b_n \end{pmatrix} = \frac{1}{2} (-\mathbf{m}_e \cdot \mathbf{e}_n^\pm + i\omega\mu_0 \mathbf{m}_m \cdot \mathbf{h}_n^\pm). \quad (3.42)$$

For the TEM mode, the relation between $\mathbf{e}_{\text{TEM}}^\pm$ and $\mathbf{h}_{\text{TEM}}^\pm$ expressed in Equation 3.32 yields to a simplified form of Equation 3.42, written as [31]

$$\begin{pmatrix} a_{\text{TEM}} \\ b_{\text{TEM}} \end{pmatrix} = -\frac{1}{2} (\mathbf{m}_e \pm jk\mathbf{m}_m \times \mathbf{z}) \cdot \mathbf{e}_{\text{TEM}}^\pm. \quad (3.43)$$

Equation 3.43 is useful in investigations further in this thesis, because it requires knowledge of only $\mathbf{e}_{\text{TEM}}^\pm$ to determined the dipole moments. The dipole moments \mathbf{m}_e and \mathbf{m}_m are separately derived by

$$\mathbf{m}_e = \frac{a_{\text{TEM}} + b_{\text{TEM}}}{\mathbf{e}_{\text{TEM}}^\pm}, \quad (3.44a)$$

$$\mathbf{m}_m = j \frac{a_{\text{TEM}} - b_{\text{TEM}}}{k_0 e_{\text{TEM}}^{\pm}}. \quad (3.44b)$$

The individual components of the electric field for a given mode $\mathbf{e}_n^{\pm} = e_n, x^{\pm} \cdot \hat{\mathbf{a}}_x + e_n, y^{\pm} \cdot \hat{\mathbf{a}}_y + e_n, z^{\pm} \cdot \hat{\mathbf{a}}_z$ can be analyzed separately by examining the output power of the TEM cell. For example, the components of \mathbf{m}_e are derived with

$$m_{ex} = \frac{2\sqrt{P_x}}{e_{n,x}^{\pm}}, \quad (3.45a)$$

$$m_{ey} = \frac{2\sqrt{P_y}}{e_{n,y}^{\pm}}. \quad (3.45b)$$

P_x and P_y describe the power measured at one output port induced by the respective component of the dipole moment [31].

For the TEM mode, an electric dipole placed in the TEM cell leads to output power with the same phase at both ports. In contrast, a magnetic dipole results in a phase shift of $\pm\pi$. This difference arises from the phase shift of the magnetic fields at the output ports, $\mathbf{h}_{\text{TEM}}^+$ and $\mathbf{h}_{\text{TEM}}^-$, as illustrated in Figure 3.9.

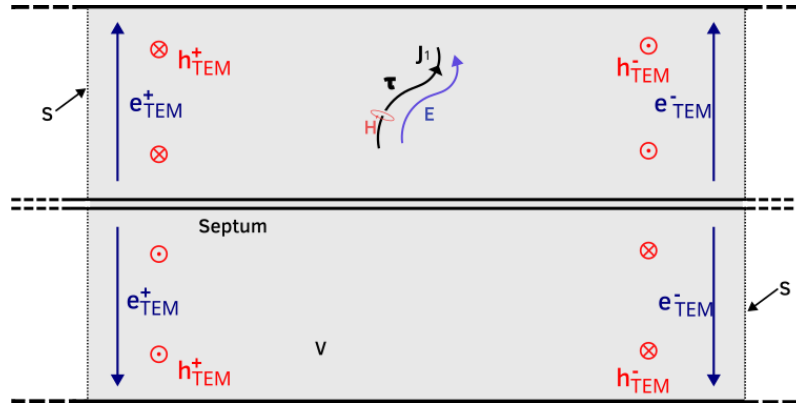


Figure 3.9 Field distribution of the TEM mode highlighting the out-of-phase magnetic fields at the output ports.

For the next higher-order mode TE₀₁, the situation is reversed. An electric dipole moment leads to a phase shift of $\pm\pi$, while a magnetic dipole moment produces no phase shift. This behavior is again due to the phase shift occurring now between the electric field intensities at the output ports, $e_{\text{TE}01}^+$ and $e_{\text{TE}01}^-$, while there is no phase shift between the magnetic field intensities, $\mathbf{h}_{\text{TE}01}^+$ and $\mathbf{h}_{\text{TE}01}^-$.

It is assumed that the dipole moments are positioned halfway along the septum in z -direction. A shift in z -direction introduces a phase shift between the output port powers, consequently altering the results derived above.

3.4.3 Electrically small antennas

The electric field coupling with an electrically small antenna can be expressed as [8, p. 361]

$$2a_n = - \int_C \boldsymbol{\tau} I(l) \cdot \mathbf{e}_n^+ dl. \quad (3.46a)$$

$$2b_n = - \int_C \boldsymbol{\tau} I(l) \cdot \mathbf{e}_n^- dl. \quad (3.46b)$$

Since the antenna is electrically small, the electric field \mathbf{e}_n^\pm is assumed to be constant in C . Furthermore, if the current I is constant along C , it does not have to be considered in the integration. Integrating over the closed loop simplifies to [8, p. 361]

$$2a_n = - \oint_C \mathbf{e}_n^+ \cdot \boldsymbol{\tau} dl = j\omega\mu_0 \iint_S \mathbf{h}_n^+ d\mathbf{s}' = V_n^+, \quad (3.47a)$$

$$2b_n = - \oint_C \mathbf{e}_n^- \cdot \boldsymbol{\tau} dl = j\omega\mu_0 \iint_S \mathbf{h}_n^- d\mathbf{s}' = V_n^-. \quad (3.47b)$$

The induced voltage V_n^+ is related to the fields \mathbf{e}_n^+ and \mathbf{h}_n^+ at the output port located in positive z -direction, while the induced voltage V_n^- to the fields at the other output port \mathbf{e}_n^- and \mathbf{h}_n^- . For the TEM mode, the total induced voltage equals $V_{\text{TEM}} = V_{\text{TEM}}^- - V_{\text{TEM}}^+$. The relation to the magnetic dipole moment \mathbf{m}_m is expressed as

$$\mathbf{m}_m = \frac{a_{\text{TEM}} - b_{\text{TEM}}}{\mathbf{e}_{\text{TEM}}^\pm \cdot k_0} = \frac{V_{\text{TEM}}}{\mathbf{e}_{\text{TEM}}^\pm \cdot k_0}. \quad (3.48)$$

For the TE₀₁ mode, the total induced voltage equals $V_{\text{TE}01} = V_{\text{TEM}}^- + V_{\text{TE}01}^+$.

In the general case, a magnetic dipole moment \mathbf{m}_m producing fields characterized with coefficients a_n and b_n models the magnetic coupling behavior of any electrically small antenna yielding the same coefficients. Consequently, deriving an equivalent magnetic dipole moments \mathbf{m}_m of an electrically small antenna is possible by measuring a_n and b_n at the output ports.

In a similar manner to Equations (3.46a) and (3.46b), a constant magnetic field \mathbf{h}_n^\pm along a magnetic current I_m following a curve C , makes following expression possible:

$$2a_n = - \int_C \boldsymbol{\tau} I_m(l) \cdot \mathbf{h}_n^+ dl, \quad (3.49a)$$

$$2b_n = - \int_C \boldsymbol{\tau} I_m(l) \cdot \mathbf{h}_n^- dl. \quad (3.49b)$$

Analogous to Equations (3.47a) and (3.47b), I_m is assumed to be constant and C to form a closed loop, leading to

$$2a_n = - \oint_C \mathbf{h}_n^- \cdot \boldsymbol{\tau} dl = -j\omega\epsilon_0 \iint_{S_0} \mathbf{e}_n^+ d\mathbf{s}', \quad (3.50a)$$

$$2b_n = - \oint_C \mathbf{h}_n^+ \cdot \boldsymbol{\tau} dl = -j\omega\epsilon_0 \iint_{S_0} \mathbf{e}_n^- d\mathbf{s}'. \quad (3.50b)$$

Now, the surfaces S_1 and S_2 are defined, which are depicted in Figure 3.10. Surface S_1 starts from S_0 and runs parallel to the electric field \mathbf{e}_n^\pm , extending infinitely. A total surface is defined $S = S_0 + S_1 + S_2$, where S_2 closes the total surface around S_1 in infinity.

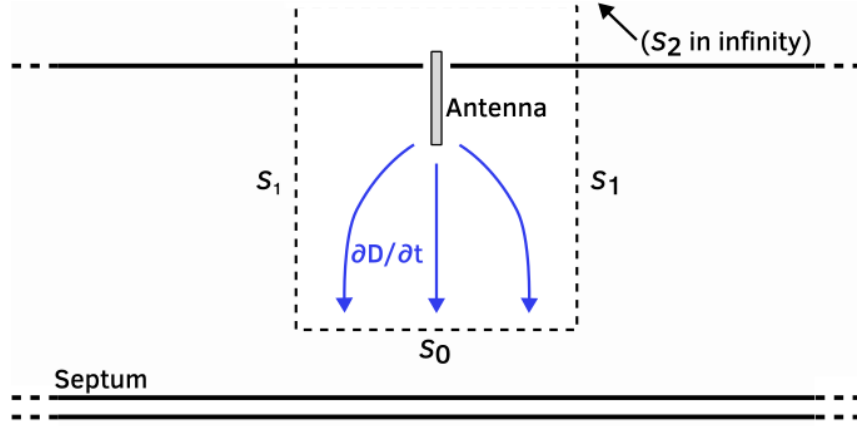


Figure 3.10 Sketch of the surfaces S_0 , S_1 and S_2 in the TEM cell with an example antenna, coupling through S_0 to the septum over the displacement current $\partial\mathbf{D}/\partial t$.

Consequently, Equations (3.50a) and (3.50b) can be written with the newly defined closed surface S as

$$j\omega\epsilon_0 \iint_S \mathbf{e}_n^\pm \cdot d\mathbf{s}' = j\omega\epsilon_0 \iint_{S_0} \mathbf{e}_n^\pm \cdot d\mathbf{s}' + \underbrace{j\omega\epsilon_0 \iint_{S_1} \mathbf{e}_n^\pm \cdot d\mathbf{s}'}_{=0} + \underbrace{j\omega\epsilon_0 \iint_{S_2} \mathbf{e}_n^\pm \cdot d\mathbf{S}}_{=0}. \quad (3.51)$$

Inserting Gauss' law $\nabla \cdot \mathbf{E} = \frac{\rho}{\epsilon_0}$ leads to

$$-j\omega\epsilon_0 \iint_S \mathbf{e}_n^\pm \cdot d\mathbf{s}' = -j\omega\epsilon_0 \iiint_V \nabla \cdot \mathbf{e}_n^\pm \cdot dv' = -j\omega \iiint_V \rho_n^\pm \cdot dv'. \quad (3.52)$$

With the continuity equation $j\omega\rho = -\nabla \cdot \mathbf{J}$ this yields

$$2a_n = -j\omega \iiint_V \rho_n^+ \cdot dv' = \iiint_V \nabla \cdot \mathbf{J}_n^+ \cdot dv' = \iint_S \mathbf{J}_n^+ \cdot d\mathbf{s}' = I_n^+, \quad (3.53a)$$

$$2b_n = -j\omega \iiint_V \rho_n^- \cdot dv' = \iiint_V \nabla \cdot \mathbf{J}_n^- \cdot dv' = \iint_S \mathbf{J}_n^- \cdot d\mathbf{s}' = I_n^-. \quad (3.53b)$$

For the TEM mode, relating the obtained Equations (3.53a) and (3.53b) to the electric dipole moment from Equation 3.44a with a total current $I_{\text{TEM}} = I_{\text{TEM}}^+ + I_{\text{TEM}}^-$ delivers

$$\mathbf{m}_e = \frac{a_{\text{TEM}} + b_{\text{TEM}}}{\mathbf{e}_{\text{TEM}}^\pm} = \frac{I_{\text{TEM}}}{\mathbf{e}_{\text{TEM}}^\pm}. \quad (3.54)$$

An electric dipole moment \mathbf{m}_e producing fields characterized with coefficients a_n and b_n models the electric coupling behavior of any electrically small antenna yielding the same coefficients. Consequently, deriving an equivalent \mathbf{m}_e of an electrically small antenna is possible by measuring a_n and b_n at the output port.

The physical meaning of I_n is the electrical current passing between the septum and the dipole via capacitive coupling, representing the displacement current. In summary, the magnetic dipole moment arises from the induced voltage on the septum, whereas the electric dipole moment results from the coupling displacement current.

3.4.4 Radiation resistance

TODO: Dieses Kapitel eventuell rausnehmen.

The radiation resistance of an electrically small antenna is derived by applying the Green's function. The following content is mostly taken from [36].

To analyze the fields in a TEM cell, the dyadic Green's function discussed in subsubsection 3.2.2 proves itself to be useful. It is assumed, that a vertical, electrically short antenna is inserted in the top center of the TEM cell. This is modeled by a current distribution in y-direction $\hat{\mathbf{J}}(\mathbf{x}) = \mathbf{a}_y J(\mathbf{x})$ [36]. Accordingly, the Green's function reduces to $\hat{\mathbf{G}}(\mathbf{x}, \mathbf{x}') = \mathbf{a}_y G(\mathbf{x}, \mathbf{x}')$. First, the Green's function for a rectangular waveguide $G_O(\mathbf{x}, \mathbf{x}')$ is shown in Equation 3.55 [3]. There, η_0 is the free-space impedance, $M = m\pi/(2a)$, $N = n\pi/b$ and $K_m = (\xi^2 - M^2)^{1/2}$. Furthermore,

$$\Delta_n = \begin{cases} \frac{1}{2}, & n = 0 \\ 1, & n > 0 \end{cases}$$

Check
Vector notation. Is
correct for
Dyadics?

and,

$$g_{mn}(\mathbf{x}_t, \mathbf{x}'_t) = \left(\frac{2}{ab} \right) \sin M(x + a) \sin M(x' + a) \cdot \cos Ny \cos Ny'$$

are functions implemented in

$$\tilde{G}_0(\mathbf{x}_t, \mathbf{x}'_t) = \frac{-j\eta_0}{k_0} \left\{ \sum_{m,n=0}^{\infty} \frac{\Delta_n[M^2 + \beta^2]}{M^2 + N^2 - \xi^2} g_{mn}(\mathbf{x}_t, \mathbf{x}'_t) \right\} \quad (3.55)$$

The components x , x' and y , y' are part of the vectors \mathbf{x}_t , \mathbf{x}'_t .

The TEM cells Green's function by adding a unperturbed term to it [36]. The derivation of those Green's Functions is demonstrated in [35], which uses the same methods described in [3], as mentioned above.

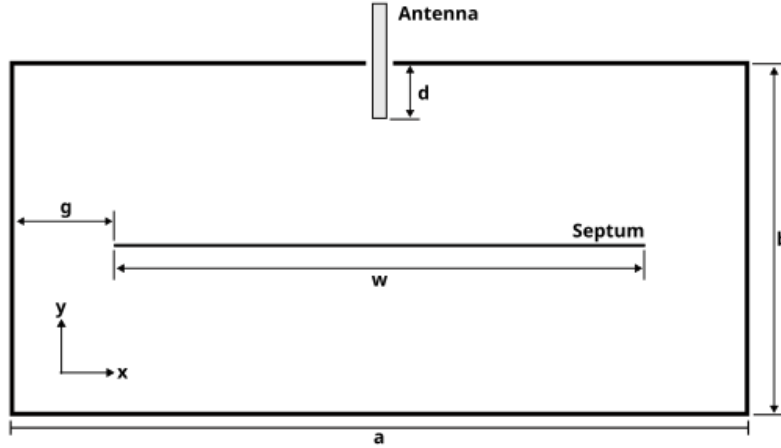


Figure 3.11 TEM cell with vertical antenna inserted

The perturbed term in

$$\tilde{G}_g(\mathbf{x}_t, \mathbf{x}'_t) = \frac{-j\pi k_0 \eta_0}{2a^2 s^2} L(\beta) f(\mathbf{x}_t) f(\mathbf{x}'_t) \quad (3.56)$$

describes the influence of the gaps on the field distribution. They are derived by forcing the tangential fields to be continuous across the gaps, then describing this boundary condition mathematically as a perturbing second Green's function. The rest of the boundary conditions on the are zero due to the geometry of the TEM cell. The functions used are,

$$L(\beta) = \left[\ln \left(\frac{8a}{\pi g} \right) - \frac{\pi}{a} \sum_{m \in \{1, 3, 5, \dots\}}^{\infty} \left(\frac{\cot K_m b}{K_m} + \frac{2a}{m\pi} \right) \right]^{-1}$$

and,

$$f(\mathbf{x}_t) = \sum_{m \in \{1, 3, 5, \dots\}}^{\infty} M \frac{\cos K_m(b-y)}{K_m \sin K_m b} \sin Ma \cos Mx J_0(Mg).$$

To receive the final Green's Function, the unperturbed and perturbed term are added together $G(\mathbf{x}_t, \mathbf{x}'_t) = G_O(\mathbf{x}_t, \mathbf{x}'_t) + G_g(\mathbf{x}_t, \mathbf{x}'_t)$. Naturally, the observation point \mathbf{x} can only be on the upper half in the chamber, where the source is also located [36].

Because waves propagating in the TEM cell are assumed to travel into infinity, they might have any longitudinal propagation constant β . They are not limited by boundary conditions in this direction. It therefore proofs useful to apply a Fourier Series over this variable, as done in

$$G_O(\mathbf{x}, \mathbf{x}') = \frac{1}{2\pi} \int_{-\infty}^{\infty} \tilde{G}_0(\mathbf{x}_t, \mathbf{x}'_t) e^{j\beta z} d\beta, \quad (3.57a)$$

$$G_g(\mathbf{x}, \mathbf{x}') = \frac{1}{2\pi} \int_{-\infty}^{\infty} \tilde{G}_g(\mathbf{x}_t, \mathbf{x}'_t) e^{j\beta z} d\beta. \quad (3.57b)$$

Now, the antenna impedance is calculated using

$$Z = \frac{-1}{I^2} \int_S \int_{S'} \mathbf{J}(\mathbf{x}) \cdot \mathbf{G}(\mathbf{x}, \mathbf{x}') \cdot \mathbf{J}(\mathbf{x}') ds' ds. \quad (3.58)$$

The Green's Function in this represents the electric field excited by an unit strength dipole [36]. Scaled by multiplication with the current density $\mathbf{J}(\mathbf{x})$ and integrated over the length of the wire, results in the total electric field. Next, by multiplying it by the current distribution $\mathbf{J}(\mathbf{x})$ and integrated over the length of the wire again, leads to the apparent power. In the end, dividing this term by the total current consumption squared I^2 leads to the impedance.

When evaluating the real part of the impedance for the case described here, the radiation resistance results from

$$R = \frac{\pi \eta_0 k_0^2}{4a^2} \csc^2 k_0 d L(k_0) H(k_0). \quad (3.59)$$

If the inserted antenna is electrically small, as it is in this case, d reduces the influence of other terms. The most dominant term then, k_0^2 , results in a quadratic relation of the radiation resistance to the frequency. This agrees with the theoretical framework in the discussion about small dipoles in ??, as well as with the simulations results in Section 4.

Here,

$$H(\beta) = \sum_{m' \in \{1, 3, 5, \dots\}}^{\infty} h_{m'}(\beta) \sum_{m \in \{1, 3, 5, \dots\}}^{\infty} h_m(\beta) J_0(r(M^2 + \beta^2)^{1/2})$$

and,

$$h_m(\beta) = \frac{M \sin Ma J_0(Mg)}{K_m \sin K_m b} \cdot \frac{\cos k_0 d - \cos K_m d}{M^2 + \beta^2}.$$

3.5 Shielding

3.5.1 Incident, reflected and transmitted waves in medium

In the following, the fundamental theory of electromagnetic shielding is presented. A figure of merit for shielding capabilities of a material is the electromagnetic shielding effectiveness SE , given in [9, 16, p. 63]

$$SE_{dB} = 20 \log \left(\frac{E_i}{E_t} \right). \quad (3.60)$$

E_i denotes the incident electric field intensity, while E_t represents the transmitted electric field intensity, as illustrated in Figure 3.12. These values depend on the material's thickness, geometry, and its electric and magnetic properties.

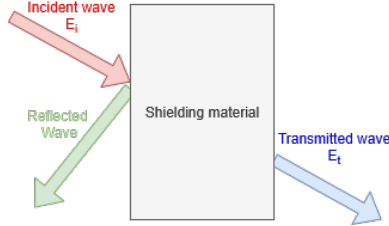


Figure 3.12 Incident, reflected and transmitted electric field intensities at a shielding material.

An electromagnetic wave can undergo reflection, absorption or multiple reflections within the shielding material, with each reflection contributing to the total reflected, absorbed, and transmitted wave. The main contribution of a material's shielding effectiveness is reflection [16, p. 1]. The total shielding effectiveness is determined by [16, p. 63]

$$SE_{\text{dB}} = R_{\text{dB}} + A_{\text{dB}} + B_{\text{dB}}, \quad (3.61)$$

according to Schelkunoff's approach to shielding [29]. Absorption losses A_{dB} arise from waves propagating through the shield, R_{dB} denotes reflections at the material's surface, and B_{dB} is a correction factor accounting for multiple reflections within the shield [9]. However, when investigating shielding materials with thicknesses less than the skin depth, B_{dB} can be neglected [16, p. 1]. While absorption A_{dB} is related to the skin depth, the thinness of the shielding material shifts the emphasis to reflection as the primary shielding mechanism. The concept of skin depth is still discussed in Section 5.1.1.

Reflections are caused by wave impedance mismatch between two materials, and are characterized by the reflection coefficient R . It is common practice to normalize the wave impedance Z to the free-space wave impedance Z_0 . At the interface between free space and a shielding material, this yields [8]

$$R = \frac{Z - 1}{Z + 1}. \quad (3.62)$$

3.5.2 Electrical characteristics

The normalized wave impedance is given by

$$Z = \frac{1}{Z_0} \sqrt{\frac{i\omega\mu}{\sigma + i\omega\epsilon}}. \quad (3.63)$$

When molecules in a material are exposed to an electric field, they become polarized. This property is characterized by the material's permittivity ϵ . Exposure to a magnetic

field causes the spins of electrons within atoms to align with the field, described by the material's permeability μ . When these electric and magnetic fields vary with time, the molecules continuously move and realign, resulting in the movement of charges, which is quantified by the conductivity σ . The energy lost in this dynamic process is dissipated as heat [2].

The electric field will push charges in polarizable molecules apart. This separation of charges may be described as a electric dipole, depending on the separation distance and the charge. Under alternating electric fields, the moving of charges will contribute to σ . This phenomenon is called dielectric hysteresis. It is quantified by the loss tangent $\tan \delta_e$, and defined as [2]

$$\tan \delta_e = \frac{\sigma_s}{\omega \epsilon'} + \frac{\epsilon''}{\epsilon'}. \quad (3.64)$$

There, σ_s is the static conductivity, indicating the conductivity of the material for constant fields over time. The complex part of the permittivity ϵ'' describes the lossy part of the dielectric material, specifically relevant for alternating fields over time. The real part of the permittivity is lossless and is noted by ϵ' , and corresponds to the material's ability to store electric energy [23]. The overall complex permittivity is therefore $\epsilon = \epsilon' + i\epsilon''$.

The loss tangent relates therefore the conductivity of a material to the real permittivity. A dielectric with low losses has a much larger displacement current than conduction current density ($\tan \delta_e \ll 1$). The opposite is true for a good conductor ($\tan \delta_e \gg 1$) [2].

Analogous to polarizable material, there are also magnetizable lossy materials, which is characterized by a complex permeability $\mu = \mu' + i\mu''$. The real part of the permeability μ' described the material's ability to store magnetic energy, while μ'' described the magnetic losses [23]. The complex permeability can also be described by a magnetic loss tangent $\tan \delta_m$, as shown in

$$\tan \delta_m = \frac{\mu''}{\mu'}. \quad (3.65)$$

Although, the loss tangent is very low for the majority of materials and will be neglected. Ferrites are an exception, which are commonly used to dampen high frequency signals [2].

Electric fields dominate in the near-field region of electric dipoles, as discussed in Section 2.1. Consequently, the wave impedance in this region is very high. For effective shielding by reflection, the shielding material should possess high permittivity and high conductivity to achieve a low impedance (see Equation 3.63), creating the necessary impedance mismatch for reflection [16, p. 67].

In contrast, magnetic fields are predominant in the near-field region of magnetic dipoles, as demonstrated with Section 2.2. A high conductivity shields well against high-frequency magnetic fields due to creation of counter-acting eddy currents [16, p. 112]. Low-frequency magnetic fields are difficult to shield, and the most common approach is the redirection of magentic flux line due to high permeability of the shielding material [16, pp. 112-113].

3.5.3 ASTM ES7-83 Method

The ASTM ES7-83 method is used to determine the shielding effectiveness of shielding materials. The shielding material is inserted into a coaxial TEM cell around the septum. Ideally, they form a continuous connection [27].

In this method, two measurements are performed with an oscilloscope attached to the output of the TEM cell. In the first, an empty TEM cell is excited and a reference output voltage U_{ref} is measured. In the second, the TEM cell is loaded with the shielding material, and the output voltage U_{load} is again noted. The measurement values are then used in

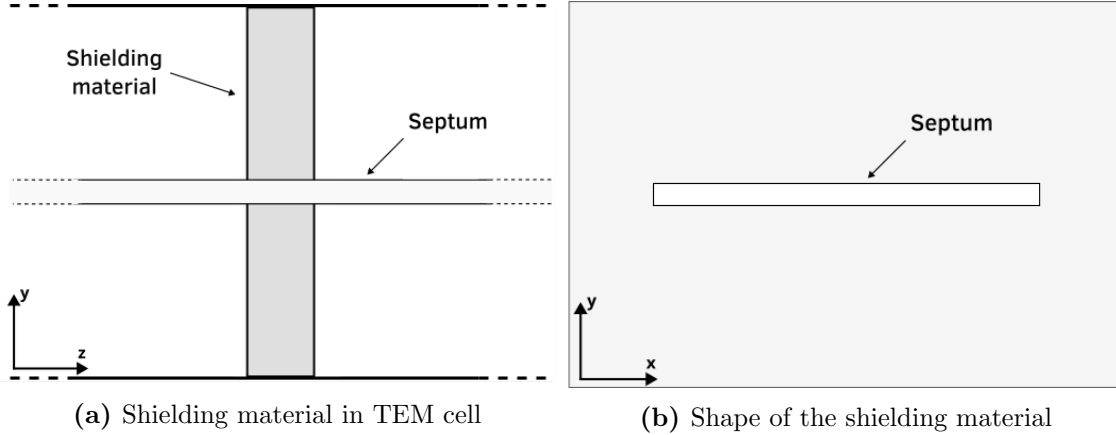
$$SE_{\text{dB}} = 20 \cdot \log \left(\frac{U_{\text{ref}}}{U_{\text{load}}} \right). \quad (3.66)$$

to derive the shielding effectiveness SE_{dB} [27].

When applying numerical analysis in combination with this method, it is more convenient to define a reference output power P_{ref} for an unloaded TEM cell, and an output power for the loaded case P_{load} . This leads to the similar

$$SE_{\text{dB}} = 10 \cdot \log \left(\frac{P_{\text{ref}}}{P_{\text{load}}} \right). \quad (3.67)$$

Additionally, a rectangular TEM cell is used for this method, instead of the commonly used cylindrical version. Figure 3.13b shows the cross section of this shielding material, which is inserted into the TEM cell. In Figure 3.13a the shielding material can be seen wrapped around the septum.



Then, the S-parameters derived in the simulations are used to get to the output powers P_{ref} and P_{load} . By exciting the TEM cell with a power of 1 W, the reference power $P_{\text{ref}} = 1 \text{ W}$. The measured power is then derived through

$$P_{\text{load}} = P_{\text{ref}} \cdot 10^{|S_{12,\text{dB}}|/10}. \quad (3.68)$$

3.5.4 Dual TEM cell

The shielding effectiveness of a material may also be determined using a dual TEM cell shown in Figure 3.14. They are connected through an aperture, which can be filled with the shielding material or left empty. The upper TEM cell is excited through port 1, and acts as a driving cell, transmitting power through the aperture. Port 2 is loaded with the reference impedance $Z_w \approx 50 \Omega$. The second TEM cell functions as a receiver, collecting power at its output ports [27].

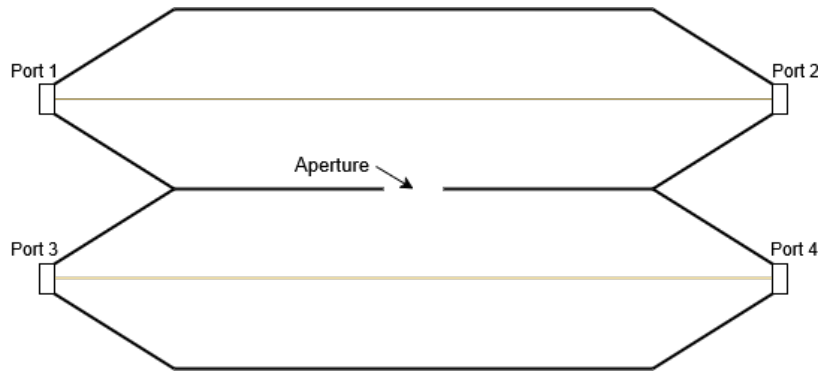


Figure 3.14 Dual TEM cell with aperture

If the aperture is electrically small, its coupling may be described by an electric and a magnetic dipole moment. Their magnitude is related to the electric and magnetic coupling between the TEM cells over the aperture. Therefore, the electric and magnetic coupling can be determined separately by adding or subtracting the output powers of the receiving TEM cell [27, 37]. Consequently, a electric shielding effectiveness SE_{dB}^e and a magnetic shielding effectiveness SE_{dB}^m can be calculated with

$$SE_{\text{dB}}^e = 10 \log \left(\frac{P_{\text{ref,sum}}}{P_{\text{load,sum}}} \right), \quad (3.69a)$$

$$SE_{\text{dB}}^m = 10 \log \left(\frac{P_{\text{ref,diff}}}{P_{\text{load,diff}}} \right). \quad (3.69b)$$

Separating the electric and magnetic shielding effectiveness is useful when applying shielding materials in the near field of electric or magnetic dipole moments. For shielding a magnetic dipole moment, the SE_{dB}^m value is considered significant [37], whereas for an electric dipole moment, the SE_{dB}^e value is relevant.

4 Finite Element Method

4.1 General Idea

Problems involving the calculations of electromagnetic fields are often cumbersome and difficult to solve. This is due to the need of solving differential equations describing these fields over a computational domain, which is not possible with a computer in this

sense. The simulation software Ansys HFSS (High Frequency Simulation Software) aims to provide a solution. This software is used for the simulations in section 4, hence it is described in this following, dedicated section.

HFSS uses a numerical technique, namely the Finite Element Method (FEM). The general idea of FEM after Rayleigh-Ritz-Galerkin is to choose a number of basis functions. The goal is to find a linear combination of these basis functions, so that the differential equation is satisfied as closely as possible. This turns the problem of solving a differential equation into a system of algebraic equations, which the computer can process. There is always a set of basis functions which enable the calculation to converge to the real solution. However, the number of basis functions used in the domain is limited, due to reasons of computability [32].

FEM therefore divides the domain into finite elements, i.e. smaller pieces. Then, within each piece, such a basis function is assigned. A linear combination of these basis functions are found, which satisfy the differential equations. In region where the approximating solution has a high degree of error, the accuracy may be increased by further subdividing the finite elements. This is repeated, until the error falls below a certain threshold, and a precise solution is derived.

4.2 Dividing a computational domain into finite elements

The differential equation to be solved is expressed as

$$\nabla \times \left(\frac{1}{\mu_r} \nabla \times \mathbf{E} \right) - k_0^2 \epsilon_r \mathbf{E} = 0 \quad \text{in } \Omega, \quad (4.1)$$

where ϵ_r is the relative permeability and μ_r is the relative permeability of the material. The variable k_0 is the wave number of free space and equals $k_0 = \omega \sqrt{\epsilon_0 \mu_0}$. [7, 24, 6].

This equation is solved in a computational domain Ω . This computational domain is divided into finite elements, called a mesh. Each node in this mesh has polynomial functions assigned, which are weighted to approximate the real solution. It has been proven that tetrahedral finite elements are best suited for this task, as they are geometrically flexible and make the definition of complete polynomial approximation functions possible [30]. Ansys HFSS uses a adaptive finite element mesh generator, which automatically provides a mesh for a given 3-dimensional construction. The Delaunay tesselation for three-dimensions is used for generating a mesh. It efficiently creates a mesh from objects of arbitrary shapes. Any boundary condition can be added recursively to the mesh. At the heart of this algorithm lies the property, that the circumsphere of an tetrahedra's vertices may not contain other tetrahedra's vertices.

Figure 4.1 shows one of such tetrahedrons. At the edge points, the components of the field which are normal to the respective edge and tangential to the face of the element is stored. At the vertex points, the component of a field which are tangential to the edges are stored. The value of the field at any midpoint is derived through interpolation from the node values. The basis function is used for interpolation.

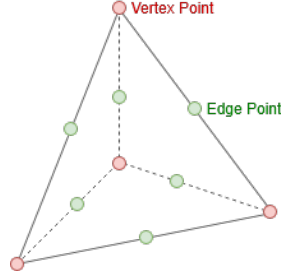


Figure 4.1 Tetrahedron with points on the edge and vertices.

Because of the way how the fields are stored in the tetrahedra, they are called tangential vector finite elements. Their advantage is that tangential components of fields can be forced to be equal among adjacent tetrahedra at the boundary. For example, an electric field stored at a vertex point must point in the direction along one of the edges, therefore it is tangential to the element. An adjacent element then has the same tangential electric field imposed at this node, leading to a continuous tangential electric field, therefore satisfying the boundary conditions implied by the Maxwell equation automatically. Furthermore, any Dirichlet boundary conditions can easily be set along the edges. [24].

The finite element is described as

$$H_1^{(\text{dim}=3)}(\text{curl}) = \left\{ \mathbf{u} \mid \mathbf{u} \in [L_2(\Omega)]^3, \nabla \times \mathbf{u} \in [P_1(\Omega)]^3 \cap D(\Omega) \right\}, \quad (4.2)$$

where $L_2(\Omega)$ is a set of square integrable functions and P_1 a set of piecewise linear functions in the discretized domain Ω [25]. The vector fields at the vertices are given as u . $D(\Omega)$ is a set of divergence free functions. The vectors u used in the finite element therefore

- are continuous in the normal direction.
- are square integrable.
- have a curl describable by piecewise linear functions.

Figure 4.2 shows the finite element with the unknowns marked at each point. For reasons of simplicity, only the face is shown. The variables u_i^j and u_j^i are imposed across element boundaries, therefore guaranteeing tangential continuity at boundaries. Additionally, they inherently defined a linear polynomial, meaning that they describe a gradient of the field along this edge. This relation is mathematically described as

$$\mathbf{u} \cdot \mathbf{t}_{ij} = \frac{1}{l_{ij}} (u_i^j - u_j^i), \quad (4.3)$$

where \mathbf{t}_{ij} is the unit vector tangentially to the edge from node i to node j and l_{ij} is the length of this edge.

Two facial unknowns f_1 and f_2 are added to two of the three edge points at one face. Contrary to the variables u_i^j , the facial unknowns f_i are only assigned locally at each

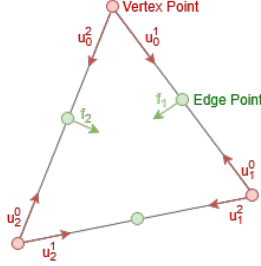


Figure 4.2 Face of the finite element with unknowns

element and do not cross boundaries. The purpose of the facial unknowns f is to provide a quadratic polynomial for the field component normal to the edges. This will lead to a linear approximation for the curl of the unknown vector field $\nabla \times \mathbf{u}$, providing sufficient accuracy. The overall vector field of this element is then calculated by a superposition of all nodes' vector attributions.

4.3 Solving the differential equation

A testing function \mathbf{W}_n is defined, which is multiplied to Equation 4.1. Integrating over the whole test volume then leads to

$$\int_{\Omega} \left(\mathbf{W}_n \cdot \nabla \times \left(\frac{1}{\mu_r} \nabla \times \mathbf{E} \right) - k_0^2 \epsilon_r \mathbf{W}_n \cdot \mathbf{E} \right) dV = 0. \quad (4.4)$$

This yields N equations, with $n = 1, 2, \dots, N$, for each finite element in the domain Ω . This is a common procedure in FEM, and it works through orthogonalization of the residual of Equation 4.1 with respect to the function \mathbf{W}_n . This means the new goal of the solution is to minimize the residual by making \mathbf{W}_n as orthogonal as possible [26].

Using the vector identity $\nabla \cdot (\mathbf{a} \times \mathbf{b}) = (\nabla \times \mathbf{a}) \cdot \mathbf{b} - \mathbf{a} \cdot (\nabla \times \mathbf{b})$ on Equation 4.4 provides a weak form of the equation, meaning a form of the original partial differential equation, which does not contain all original derivatives [7, 6]. Additionally, boundary terms come into play, as seen in the right hand side of the resulting

$$\int_{\Omega} \left[(\nabla \times \mathbf{W}_n) \cdot \frac{1}{\mu_r} \nabla \times \mathbf{E} - k_0^2 \epsilon_r \mathbf{W}_n \cdot \mathbf{E} \right] dV = \oint_{\partial\Omega} \underbrace{\left(\mathbf{W}_n \times \frac{1}{\mu_r} \nabla \times \mathbf{E} \right)}_{\text{Boundary term}} \cdot d\mathbf{S}. \quad (4.5)$$

The usefulness in this step has been described as lowering the highest-order derivative, therefore the approximating functions need to guarantee continuity of value, not of slope [14]. Another explanation is the possibility of incorporation of Neumann boundary conditions [26].

Next, the electric field \mathbf{E} is represented by a superposition of basis functions. When applying Galerkin's method, the basis functions are equal to the test functions W_n . The sum of the basis functions is

$$\mathbf{E} = \sum_m^N x_m \mathbf{W}_n, \quad (4.6)$$

which are weighted with the variable x_m . These variables x for all elements have to be solved, to find the electric field \mathbf{E} over the whole domain. The FEM has therefore reduced the initial wave equation in Equation 4.1 to a simple linear matrix equation $Ax = b$, where A is a known $N \times N$ matrix, b contains port excitations and x is the unknown. Ideally, the basis functions are defined to be zero outside of their adjacent elements. This will result to zero for all entries in the matrix, where the test and basis function do not overlap. Therefore, the matrix is sparse, and will be solved much faster. In the end, other electromagnetic quantities can all be derived through the electric field.

The matrix then is expressed as

$$A_{ij} = \int_{\Omega} \nabla \times \mathbf{W}_i \frac{1}{\mu_r} \nabla \times \mathbf{W}_j dV - k_0^2 \int_{\Omega} \mathbf{W}_i \epsilon_r \mathbf{W}_j dV + ik_0 \left(\frac{\eta_0}{Z_s} \right) \oint_{\partial\Omega} \mathbf{n} \times \mathbf{W}_i \cdot \mathbf{n} \times \mathbf{W}_j d\mathbf{S}. \quad (4.7)$$

Some manipulation on the boundary term have been made, so that it contains the surface impedance Z_s . The surface impedance defines the ratio of the electric field to the magnetic field on the boundary region. Furthermore, it contains the free space, which equals $\eta_0 \approx 377 \Omega$.

4.4 Adaptive solution process

Each finite element therefore has a solved electric field assigned, which should approximate the real solution as closely as possible. To determine the error for each element, Equation 4.1 is evaluated. The elements with the highest residuals contain the largest deviation from the real result, meaning they have a large degree of error, as described in

$$\nabla \times \left(\frac{1}{\mu_r} \nabla \times \mathbf{E}_{\text{solved}} \right) - k_0^2 \epsilon_r \mathbf{E}_{\text{solved}} = \text{residual}. \quad (4.8)$$

Regions in the mesh with large degrees of errors are refined, i.e. the tetrahedral finite elements are split into smaller ones. This allows the FEM solver to recalculate the fields in this region with higher precision, leading to a smaller residual. Consequently, the finite elements represent the fields more accurately, due to a smaller element size and higher resolution [5]. An additional method is increasing the order of the polynomial basis functions of elements with low degree of accuracy.

To determine when the iterative refinement process is done and the solution good enough, some kind of threshold must be defined. One possibility is the Max ΔS parameter. It is compared to the difference of S-parameters of the defined excitation ports over two iterations. If, after a mesh refinement, the S-parameters of the ports do not significantly change anymore, meaning change less than Max ΔS , then the iterative process can be considered done. This described iterative process is shown in Figure 4.3.

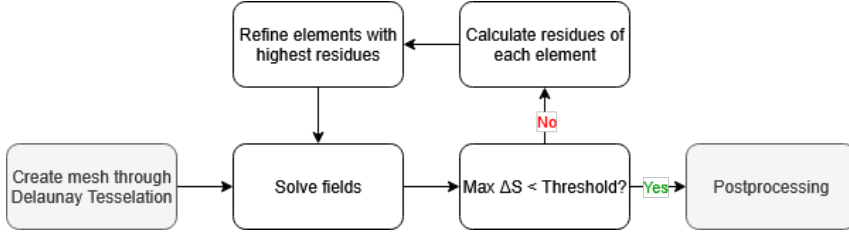


Figure 4.3 Adaptive solution process

5 Numerical Investigations of Antennas in TEM Cells

5.1 Preliminary Considerations for Numerical Analysis

5.1.1 Skin Effect

TODO: Skin Effect Kapitel zu Shielding Kapiteln geben?

The Skin-effect causes current to flow through a reduced area in a conductor, thus increasing resistance. The imaginary part κ of the complex wave number k is described by

$$\kappa = \omega \sqrt{\frac{\epsilon\mu}{2}} \left[\sqrt{1 + \left(\frac{\sigma}{\epsilon\omega} \right)^2} - 1 \right]^{1/2}. \quad (5.1)$$

The skin depth d is responsible for the increased conductor losses and is expressed as

$$d = 1/\kappa. \quad (5.2)$$

For highly conductive materials ($\sigma \ll \epsilon\omega$) the skin depth is $d \propto 1/\sqrt{\omega}$. Conductor losses P_{loss} are linearly proportional to the area of the conductor and therefore Skin-depth. They show the same dependency on the frequency $P_{\text{loss}} \propto 1/\sqrt{\omega}$ [11, p. 413]. Conductor losses contribute to the power consumption of the small loop antenna and is significantly larger than radiation power [3, p. 231].

The investigations in this thesis focus on the coupling behavior of antennas, including the radiation power consumed. All conducting surfaces in the simulation models are perfect electric conductors (PEC) to remove the impact of the Skin-effect.

5.1.2 Antenna models

Every antenna is fed with a round feedpoint, shown in Figure 5.1. They provide an incident wave of unit power (1 W). The antenna wires are modeled as PECs with a diameter of 0.2 mm. The geometry is intentionally kept simple, with the cylindrical wires pointing either in x-, y- or z-direction, without combining multiple orientations.

The first two antennas investigated are the monopole (Section 5.2) and the loop antenna (Section 5.3), which represent the most basic antennas producing electric and magnetic

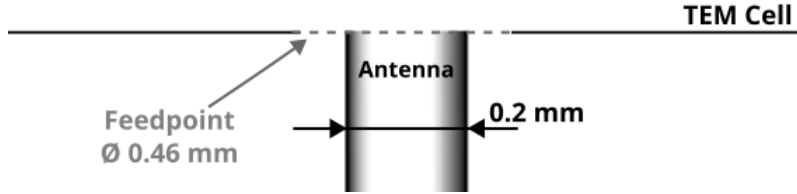


Figure 5.1 Geometry of an antenna's feedpoint used in simulation. The antenna is fed through a round waveport of diameter 0.46 mm. The antenna consists of PEC wire with diameter of 0.2 mm. This geometry leads to a reference impedance of $Z_0 \approx 50 \Omega$.

dipole moments, respectively. Other electrically small antennas deliver similar results, depending on whether they are capacitive or inductive. Capacitive antennas are analogous to monopole antennas, and inductive ones to the loop antenna, both including their equivalent circuits. This applies even for electrically small antennas with high Q-factor.

5.1.3 TEM cell model

The TEM cell model used, shown in Figure 3.3, has a width of $a = 40$ mm, a height of $b = 24$ mm and a length of $l = 100$ mm. The cut-off frequencies of higher-order modes are demonstrated in Figure 3.4. In following investigations focusing on the TEM mode, the frequency range of interest spans from 1 MHz to 3 GHz. If the TE₀₁ mode is included in the investigations, the upper limit of the frequency range is extended to 3.3 GHz.

The cell walls and septum are modeled as PECs. In the TEM cell simulation model, the tapered transition sections at the ports are omitted. As discussed in Section 3.3.3, this simplification allows unrestricted propagation of higher-order modes, facilitating investigations of their coupling behavior with antennas. The reference impedances of the output ports equal $Z_w \approx 50 \Omega$.

Upon exciting the output ports, the electric and magnetic energy W_e and W_m stored in the TEM cell is derived by Equation 2.22. The current and voltage at the output ports is found with Equations (5.7) to (5.8). The capacitance and inductance of the TEM cell are given by Equations (2.23a) to (2.23b). The TEM cell has a constant capacitance and inductance of $C_T = 6.74 \text{ pF}$ and $L_T = 16.25 \text{ nH}$.

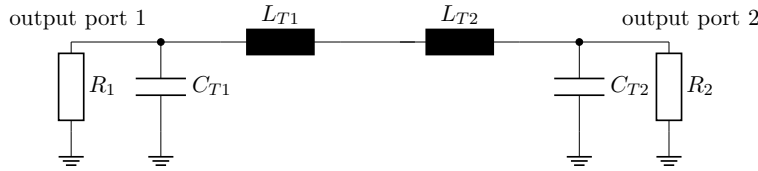


Figure 5.2 Circuit representing the TEM cell, where the capacitance and inductance is split into two separate, equal components $C_T = C_{T1} + C_{T2}$, $L_T = L_{T1} + L_{T2}$ and $C_{T1} = C_{T2}$, $L_{T1} = L_{T2}$. The resistances R_1, R_2 at the output ports model the reference impedance $Z_w \approx 50 \Omega$.

5.1.4 Dipole moments models

A magnetic dipole moment can be expressed equivalently as either an electric current I_0 in a loop, or a magnetic current I_m in a line, as described in Equation 2.16. All dipole moments used in the simulations are assumed to be of infinitesimal length, as discussed in subsubsection 2.1.1 and subsection 2.2. For infinitesimal magnetic dipoles, Equation 2.16 simplifies to

$$|\mathbf{m}_m| = j\omega\mu_0|\mathbf{m}_0|, \quad (5.3)$$

where \mathbf{m}_m with the unit Vm denotes the magnetic dipole moment in the magnetic current representation, and \mathbf{m}_0 with the unit Am² the moment in the electric current representation [20]. The simulation models represent magnetic dipole moments with \mathbf{m}_m , which will be used in further investigations.

The electric and magnetic dipole moments are placed at the center of the TEM cell at $x = 0, y = b/2, z = 0$. As discussed in subsubsection 3.3.4, $\mathbf{e}_{\text{TEM}}^{\pm}(x = 0, y = b/2, z = 0)$ has only a y-component at this location, while $\mathbf{h}_{\text{TEM}}^{\pm}(x = 0, y = b/2, z = 0)$ has only an x-component. Consequently, the equivalent dipole moment \mathbf{m}_e is oriented along the y-direction, and \mathbf{m}_m along the x-direction.

Placing \mathbf{m}_m and \mathbf{m}_e in the center of the TEM cell therefore significantly simplifies modeling electrically small antennas with equivalent dipole moments. This assumption is valid for the TEM mode. This configuration is assumed for all numerical investigations following in this thesis, unless otherwise stated.

When normalizing to the free-space wave impedance η_0 , \mathbf{m}_e can be interchanged with an equivalent \mathbf{m}_m and vice-versa [15, p. 414]. Therefore, normalizing either \mathbf{m}_e or \mathbf{m}_m to the free-space wave impedance Z_0 enables a meaningful comparison between them.

All simulation results are counterchecked by inserting the equivalent dipole moments into the TEM cell and comparing the power and phase at the output ports with the antenna's results.

5.1.5 Mesh modifications

The mesh determines the resolution of the field quantities over the computational domain. Since electrically small conductors are involved, implementing small mesh elements in their proximity is necessary for accurate modeling of near-fields. Adaptive meshing algorithms may neglect this task, due to the low impact of these near-fields on the solution of the overall computational domain. Consequently, adjusting mesh element sizes does not significantly influence the overall solution of the model, but greatly improves the accuracy of near-field investigations.

The maximum mesh element length in error-prone volumes are adjusted, until the obtained results show a reasonably low amount of numerical artifacts. Such volumes are commonly located adjacent to feedpoints and along edges of small conductors, where large field intensities occur within small spatial regions. The simulation models used in this thesis

use roughly 15 elements on the surfaces of such critical volumes to achieve a reasonable representation of these regions while avoiding excessively large meshes.

Lastly, it is best practice to select the upper limit of the investigated frequency range as the solution frequency. This choice produces the largest spatial field changes, forcing the adaptive mesh process to generate a high-resolution mesh. Results in the frequency range below the solution frequency benefit from a reusable mesh that is finer than required. This procedure is applied for every numerically derived frequency-dependent result presented in this thesis.

5.1.6 Shielding material models

The numerical investigation of large computational domains containing thin shielding material requires large mesh sizes for accurate representation of fields around the shield. Especially in the analysis of the ASTM ES7-83 method in Section 6.1, the shielding material leads to high computational effort. A solution is the implementation of boundary conditions on the shielding material's surface, as described in [4].

In this solution process, the shielding material is removed from the computational domain. Instead, the boundary conditions imposed on its surface are considered, and plane wave propagation normal to the surface is assumed.

5.1.7 S-parameters and derived data

The TEM cell with an antenna is modeled as a three-port network. The two output ports of the TEM cell are denoted as ports 1 and 2, while the antenna feedpoint is marked as port A. The behavior of this system is fully characterized by its scattering matrix, given as

$$[S] = \begin{bmatrix} S_{11} & S_{12} & S_{1A} \\ S_{21} & S_{22} & S_{2A} \\ S_{A1} & S_{A2} & S_{AA} \end{bmatrix}. \quad (5.4)$$

The coupling between the antenna and the two ports of the TEM cell are described by S-parameters, specifically the forward transmission coefficients S_{A1} and S_{A2} . The phases of the forward transmission coefficients Φ_{A1} and Φ_{A2} provide information on the phase shift between the incident wave at port A, and the transmitted wave at output ports 1 and 2. The magnitude of this coefficient is the same for the antenna to both ports $|S_{A1}| = |S_{A2}|$, given that the antenna is placed far from the output ports. The power transferred from the antenna P_A to the output ports P_1 and P_2 is derived through

$$P_A = \frac{P_1}{10^{|S_{A1}|/10}} = \frac{P_2}{10^{|S_{A2}|/10}}. \quad (5.5)$$

Consequently, if the normalized electric field distribution of the TEM mode $\mathbf{e}_{\text{TEM}}^{\pm}$ is unknown, it may be derived by setting the output power of a waveport to $P_1 = P_2 = 1/2 \text{ W}$. For example, the uniformly distributed, normalized electric field of the TEM mode along the y-axis at the center of the TEM cell ($z = 0, x = 0$) is derived by

$$|a_{\text{TEM}}| \cdot \mathbf{e}_{\text{TEM}}^+(x = 0, y, z = 0) = \frac{\sqrt{P_1 Z_0}}{b/2}. \quad (5.6)$$

The difference in phase of S_{A1} and S_{A2} influences the magnitude of magnetic dipole moments and electric dipole moments, as discussed in subsubsection 3.4.2. The peak value of the current through the feedpoint of the antennas is calculated with the S-parameters,

$$I_A = \sqrt{2P_A} \frac{(1 - S_{AA})}{\sqrt{Z_0}}. \quad (5.7)$$

P_A is the incident power wave applied to the port. The peak voltage at the feedpoint is calculated in a similar fashion as

$$V_A = \sqrt{2P_A}(1 - S_{AA})\sqrt{Z_0}. \quad (5.8)$$

Another method to derive voltages and currents is by integration of field intensities. Special care has to be taken at mesh refinement in the area of integration to reduce numerical errors.

The impedance seen from the antenna feedpoint is

$$Z_A = Z_0 \frac{1 + S_{AA}}{1 - S_{AA}}. \quad (5.9)$$

All values are peak values, unless otherwise stated.

5.1.8 Investigation of field regions

Update field plots

In this section, the coupling-field regions described in subsection 2.3 are analyzed using the model shown in Figure 5.3. This analysis examines whether frequency-dependent coupling behavior of the TEM cell can be attributed to changes in the dominant coupling-field region.

To determine the influence of the field regions on the coupling effect, \mathbf{m}_e and \mathbf{m}_m are placed in two different TEM cells of dimensions $a = 10$ mm, $b = 6$ mm and $a = 40$ mm, $b = 24$ mm. The $k \cdot r$ -factor for both cases is shown in Figure 5.4.

Making the TEM cell smaller such that $k \cdot r \ll 1$, proves to be feasible. The following simulations are conducted with a TEM cell of dimensions $a = 10$ mm and $b = 6$ mm, visible in Figure 5.3.

First, the current loop antenna used in subsection 5.3 is placed in the dead center of the TEM cell. The equivalent dipole moments are shown in Figure 5.5. In the Figure 5.6 next to it, the dipole moments of the same antenna in the larger TEM cell used before ($a = 40$ mm and $b = 24$ mm) are presented.

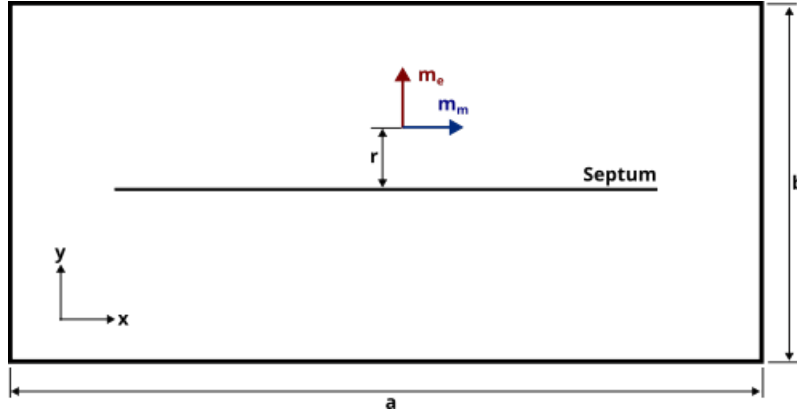


Figure 5.3 A TEM cell containing an electric \mathbf{m}_e and a magnetic dipole moment \mathbf{m}_m in the center $x = 0, y = r = b/4, z = 0$ to investigate the field regions in which the coupling occurs.

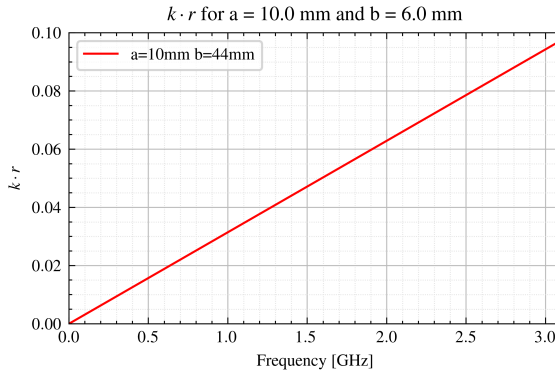
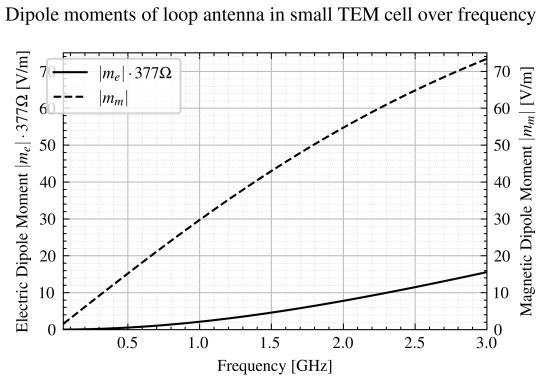
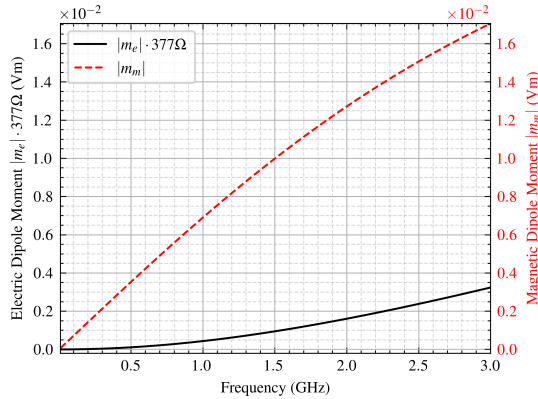


Figure 5.4 $k \cdot r$ in small TEM cell

TODO:Redo plots

This is done to compare the dipole moments in both cases. While they clearly increased by magnitude in case of the small TEM cell due to better coupling, their non-linear frequency relation still remains. This means that the change of field regions is not the reason for this behavior.

The $k \cdot r$ factor is determined in Figure 5.4 in the frequency range from 1 MHz to 3 GHz for the small TEM cell. This factor does not surpass 0.1, thus fulfilling the requirement $k \cdot r \ll 1$ for this investigation. For comparison, the $k \cdot r$ factor over a wider frequency range are shown in Figure 5.4 for the normal sized TEM cell ($a = 40$ mm and $b = 24$ mm) and a degenerately high TEM cell ($a = 10$ mm and $b = 44$ mm). The high TEM does not have a port impedance of 50Ω , and is an attempt to achieve a large $k \cdot r$ factor without higher-order modes propagating. The markers in ?? indicate the cut-off frequency, in which the next higher-order mode propagates. They demonstrate, that even in the high TEM cell a $k \cdot r = 1$ is not achieved.

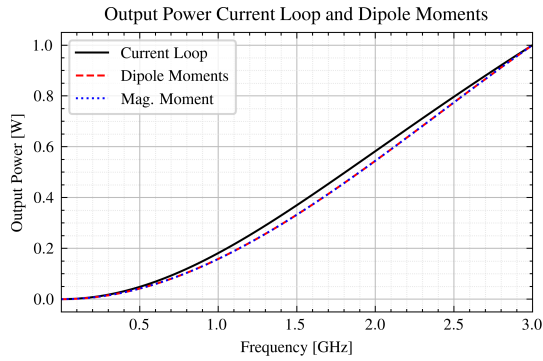
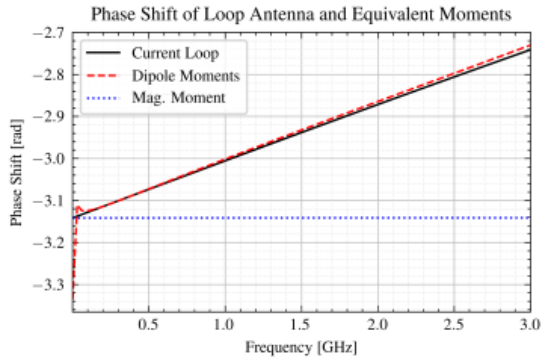
**Figure 5.5** Moments in small TEM cell**Figure 5.6** Moments in normal TEM cell

Fix figures: Titles and Legends. Add kr of normal cell.

Now, three simulations are conducted with different excitation sources in the small TEM cell:

- The current loop
- The equivalent dipole sources e_z and m_m of the current loop
- The equivalent magnetic dipole source m_m , neglecting e_z

Figure 5.7 shows the output power over frequency normalized to 1 W for all three constellations. The normalization is done to qualitatively discuss the frequency-dependent coupling behavior. Figure 5.8 demonstrates the phase shift between the powers at the two waveports over frequency.

**Figure 5.7** Output powers**Figure 5.8** Phase shifts

The frequency dependent behavior of the output power does not change depending on the type of dipole moment used. This is significant, because this shows that the dipole moments do not exhibit different coupling behaviors in the TEM cells. This is further proven in the phase shift plots. The magnetic dipole moment causes a constant phase shift of $-\pi$. If this was not the case, this would mean that the coupling behavior of the

magnetic dipole moment in the TEM cell would change. Since the opposite is the case, this poses as good evidence against arguments of change in field regions causing the non-linear dipole moment behavior. Instead, it is very likely to be caused by the geometry of the antenna.

5.2 Monopole Antenna

5.2.1 Setup

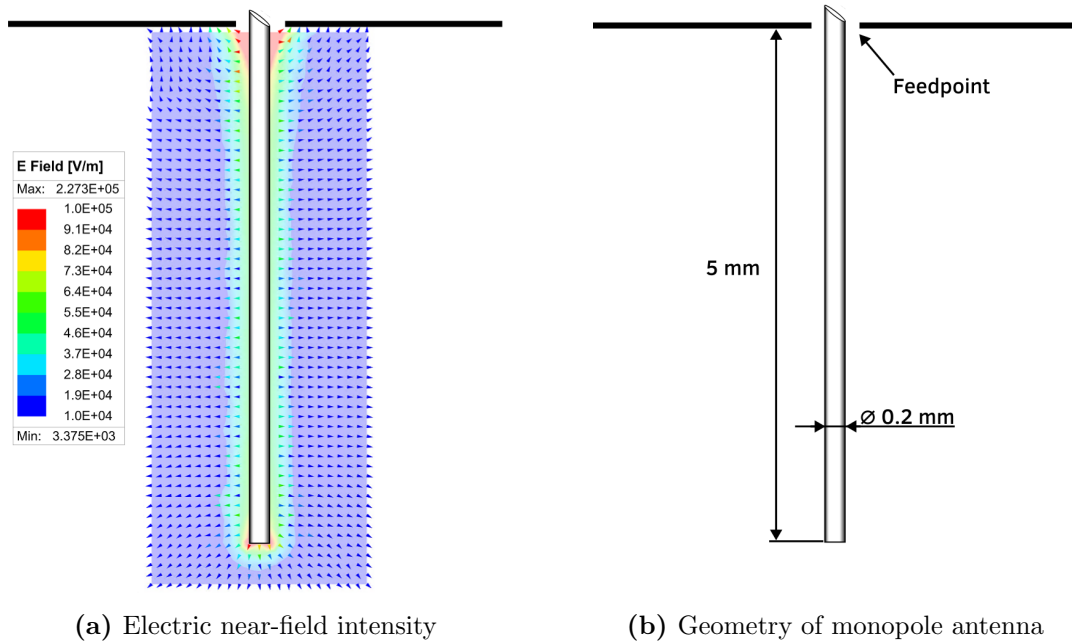


Figure 5.9 The geometrical aspects of the cylindrical monopole antenna, as implemented in the simulation model, with the respective electric near-field plot.

The monopole antenna is the most basic antenna generating an electric dipole moment. It is shown in Figure 5.9b, installed in the TEM cell and connected to a feed point located on the top wall. The numerically derived near-field plot of the monopole antenna shows strong displacement currents near the feedpoint and at the wire end. Simulation results are improved by decreasing mesh element lengths in these regions. The current flowing through it is aligned with the TEM mode and produces an electric dipole moment.

The antenna has a physical length of 5 mm, making it electrically short for frequencies up to 6 GHz. For frequencies up to 1.25 GHz, it can be accurately approximated as an infinitesimal electric dipole, as discussed in subsubsection 2.1.1. At higher frequencies, up to 6 GHz, it behaves as a small electric dipole, as explained in subsubsection 2.1.2.

5.2.2 Equivalent dipole moments

The corresponding equivalent electric and magnetic dipole moments, \mathbf{m}_e and \mathbf{m}_m , are analytically derived using Equations (3.44a) to (3.44b). The resulting \mathbf{m}_e shown in Fig-

ure 5.10 increases approximately linearly over frequency, while the magnetic dipole moment is negligible over the whole frequency range.

Furthermore, the phase difference between the power at the two output ports is zero across the entire frequency range. This observation is consistent with the assumption that a pure electric dipole moment introduces no phase shift between the output port powers, as discussed in subsubsection 3.4.2.

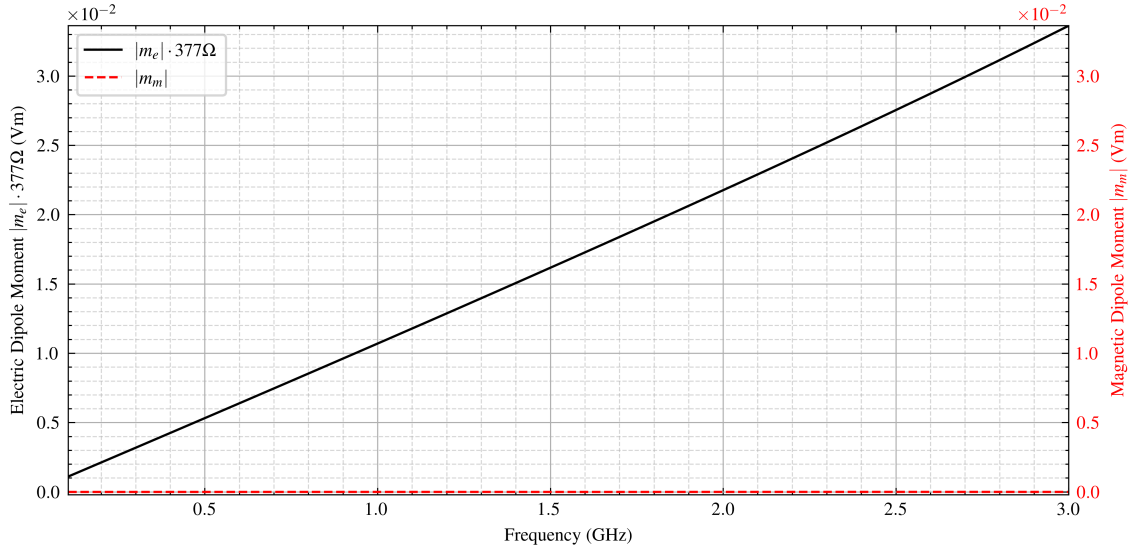


Figure 5.10 The equivalent electric and magnetic dipole moments analytically calculated with Equations (3.44a) to (3.44b). To enable direct comparison with the magnetic dipole moment, the electric dipole moment is weighted with the free space impedance Z_0 , as discussed in subsubsection 5.1.4.

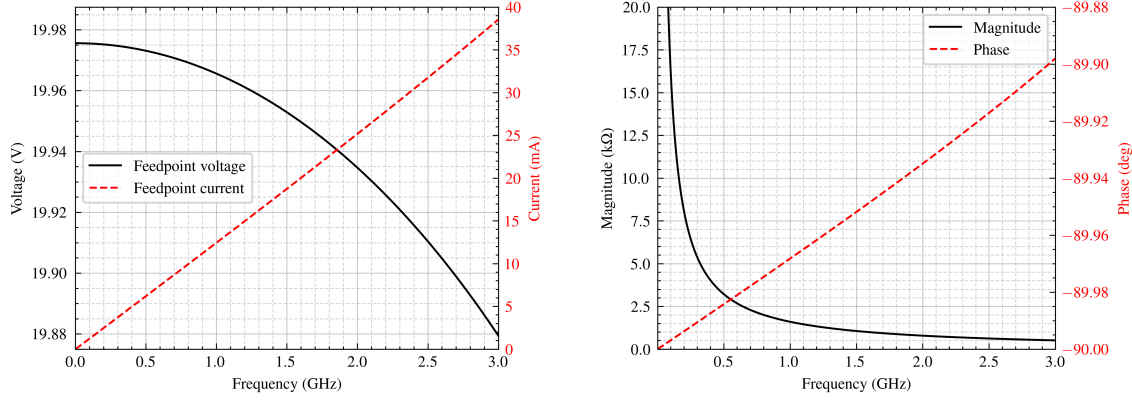
5.2.3 Electrical characteristics

The feedpoint voltage V of the antenna, shown in Figure 5.11a, remains largely constant over the investigated frequency range. Consequently, the voltage induced between the antenna and the septum is negligible. This observation is consistent with the absence of a magnetic dipole moment \mathbf{m}_m , which is directly related to the induced voltage according to Equation 3.48.

The feedpoint current I , shown in Figure 5.11a, increases linearly. The entire current contributes to displacement currents due to the absence of a return path. According to Equation 3.54, \mathbf{m}_e is proportional to the displacement current to the septum. The linear increase of \mathbf{m}_e and I are therefore related.

At low frequencies, the antenna impedance in Figure 5.11b shows a high magnitude, which rapidly decreases as frequency increases. Over the whole frequency range, it exhibits highly capacitive behavior, which is consistent with Equation 2.11 and the discussion in subsubsection 2.1.1.

Applying Equation 3.54 to determine \mathbf{m}_e requires knowledge of the magnitude of the



(a) Voltage and current at feedpoint over frequency

(b) Antenna impedance over frequency

Figure 5.11 Magnitude of the voltage and current applied at the feedpoint of the monopole antenna over frequency, derived through the S-parameters with Equations (5.7) to (5.8), with the respective magnitude and phase of the antenna impedance over frequency, derived through the S-parameters with Equation 5.9.

displacement current to the septum. Another possibility of determining \mathbf{m}_e is the integration of the current I weighted by $\mathbf{e}_{\text{TEM}}^\pm$ along the monopole antenna, as given in Equations (3.46a) to (3.46b). At a frequency of 3 GHz, this approach yields

$$\mathbf{m}_e(f = 3 \text{ GHz}) = \int_{b/2-5 \text{ mm}}^{b/2} I(y, f = 3 \text{ GHz}) dy = 85.69 \mu\text{Am} \cdot \hat{\mathbf{a}}_z, \quad (5.10)$$

which corresponds to $\mathbf{m}_e \cdot Z_0 = 3.23 \cdot 10^{-2} \cdot \text{Vm} \hat{\mathbf{a}}_z$ when normalized by the free-space wave impedance Z_0 . This approximates \mathbf{m}_e in Figure 5.10 at 3 GHz reasonably well, therefore supporting Equations (3.46a) to (3.46b).

The derived equivalent dipole moments \mathbf{m}_e , \mathbf{m}_m in the TEM cell produce the output power over frequency shown in Figure 5.12b, where they are compared with the output power produced by the monopole antenna. The equivalent dipole moment approximation of the monopole antenna loses precision when approaching the cut-off frequency of the first higher-order mode TE_{01} . Considering the coefficients $a_{\text{TE}01}$ and $b_{\text{TE}01}$ of the TE_{01} -moment increases accuracy, which is not done here.

The distribution of the current along the monopole antenna shown in Figure 5.13 is numerically derived by integrating the magnetic field intensity in a closed loop around the wire using Ampère's law,

$$\oint_L \mathbf{H} \cdot d\mathbf{l}' = I. \quad (5.11)$$

The current distribution at 3 GHz (see Figure 5.13) approximates that of a small electric dipole, as described in subsubsection 2.1.2. It shows an approximately linear decrease

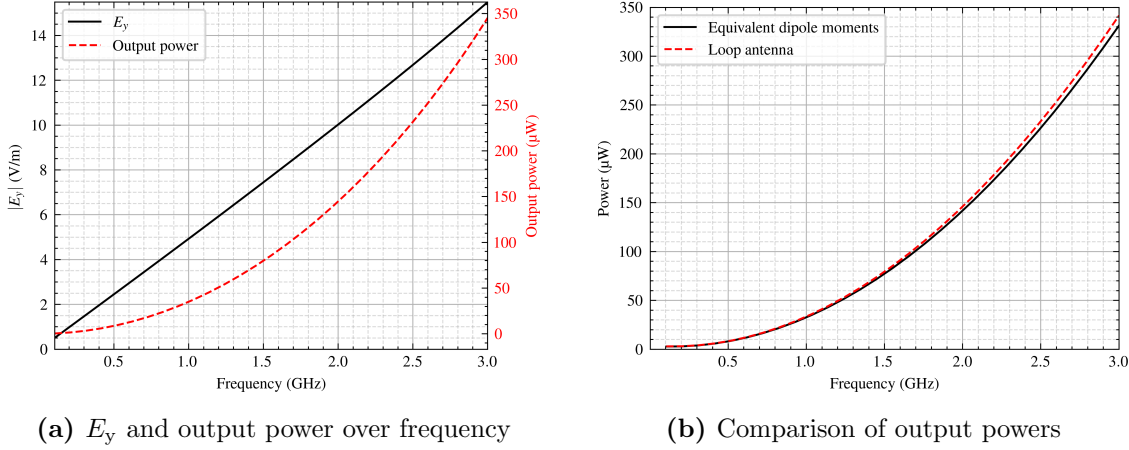


Figure 5.12 Electric field in y-direction E_y at $x = 0, y = b/4, z = \pm l/2$, and power at one output port, derived with the S-parameters in Equation 5.5. The output power produced by the monopole antenna is compared to the output power produced by the equivalent dipole moments, to demonstrate validity of the model.

towards zero.

The current distribution at 1 MHz, shown in Figure 5.14, also decreases linearly along the monopole antenna. It can be approximated with an infinitesimal electric dipole, as discussed in subsubsection 2.1.1.

A fine mesh resolution, as discussed in subsubsection 5.1.5, is important for accurate results delivered by Equation 5.11. Consequences of a rough mesh is non-linear behavior near the feedpoint at 0 mm in Figure 5.15, which becomes apparent due to significant displacement currents and numerical artifacts in this region. This causes the current to exhibit a steeper decline with non-physical oscillations.

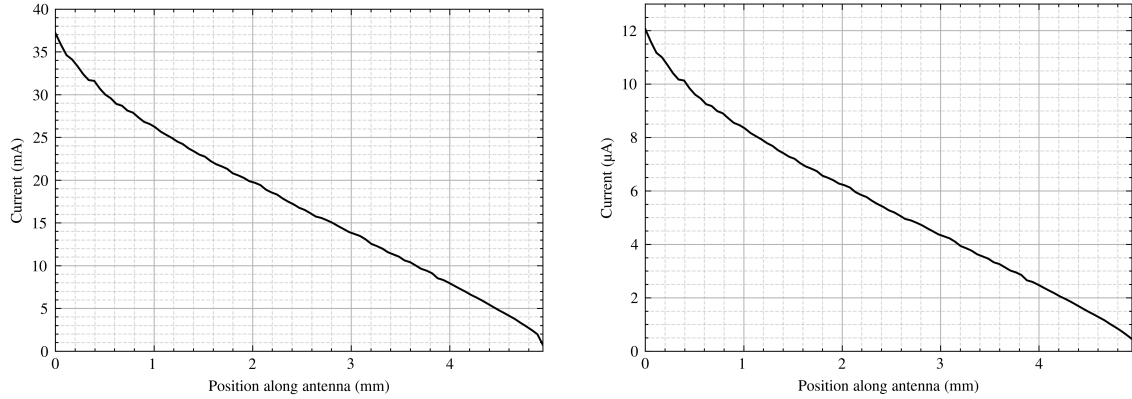


Figure 5.13 Current distribution at 3 GHz

Figure 5.14 Current distribution at 1 MHz

Figure 5.15 The current distribution along the monopole antenna at 3 GHz and 1 MHz.

TODO: Equivalent circuit for Monopole Antennas

An equivalent circuit is derived in Figure 5.16, which is known as Chu equivalent circuit for a short dipole [13].

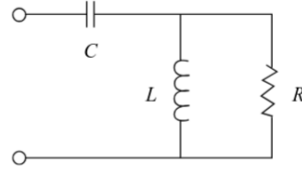
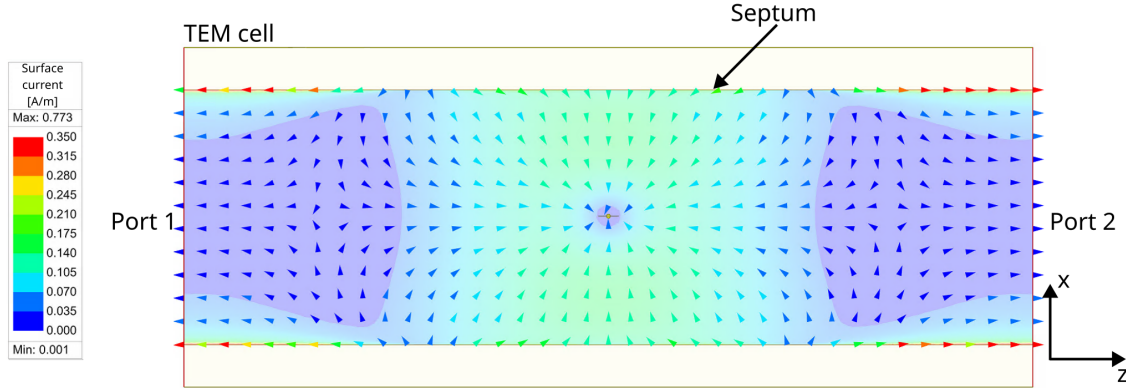


Figure 5.16 The Chu equivalent circuit for a short electric dipole models the monopole antenna's behavior.

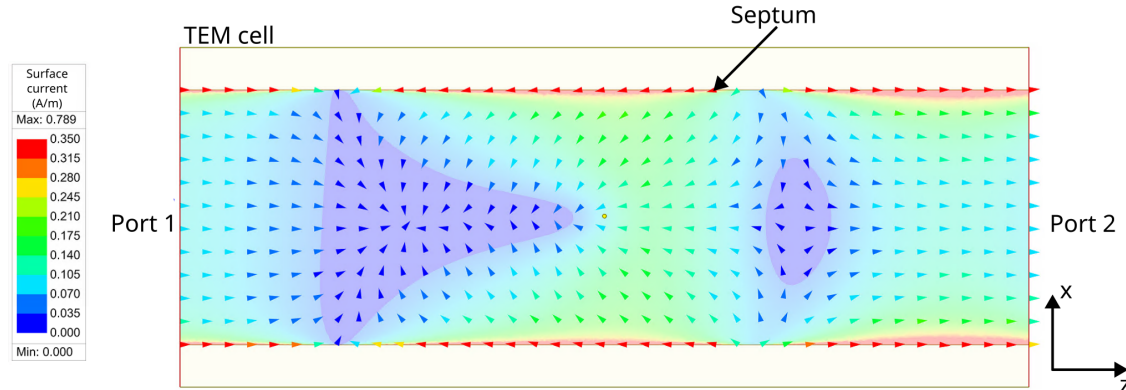
5.2.4 Current distribution on septum

Figure 5.17a shows the surface current density on the septum induced by the monopole antenna at 3 GHz. The current reaches both output ports in phase, confirming the absence of a phase shift between the output port powers.

Figure 5.17b shows the current density of the septum at 3.3 GHz, with the TEM-mode compensated at the output ports. Due to the magnetic fields propagating in the z -direction, the current on the septum forms a pattern of swirls. However, at a frequency of 3,GHz, this pattern is not as pronounced, as the current in the swirls negligible, as shown in Figure 5.17a. Furthermore, the phase shift of the induced power between the output ports is π . This results from the magnetic field intensities of the TE₀₁-mode being in-phase at the output ports, opposed to the magnetic field intensities of the TEM-mode.



(a) Current surface density at 3 GHz, where mostly the TEM-mode propagates.

(b) Current surface density of only the TE₀₁-mode at 3.3 GHz with the TEM mode compensated.**Figure 5.17** Current surface densities at different frequencies, below and above the cut-off frequency of the TE₀₁-mode.

5.2.5 Electromagnetic energy in the TEM cell

The monopole antenna generates electromagnetic fields within the TEM cell, resulting in stored electromagnetic energy. The frequency-dependent electric energy is shown in Equation 2.22. Its quadratic increase correlates with the output power in Figure 5.12a. The corresponding magnetic energy is several orders of magnitude smaller due to the capacitive behavior of the monopole antenna and is therefore neglected. From the stored electric energy, both the real and imaginary components of the power consumed by the antenna can be determined.

Moreover, the effective inductance and capacitance of the monopole antenna inside the TEM cell can be derived from the magnetic and electric energy expressions given in Equations (2.23a) to (2.23b). Using the peak value of the electric energy shown in Figure 5.18, the capacitance is estimated to be $C \approx 108.55 \text{ fF}$.

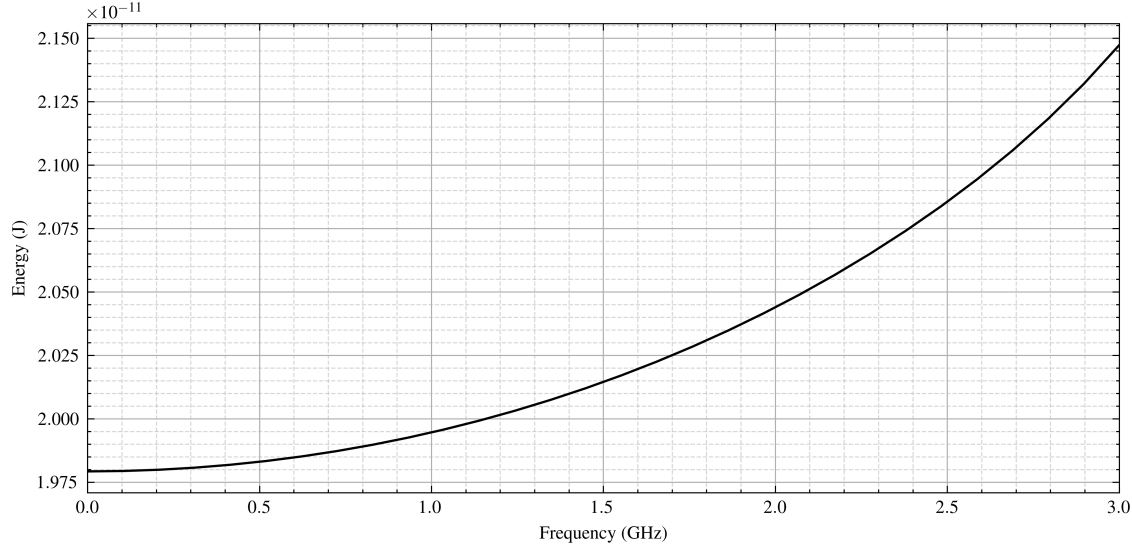


Figure 5.18 Electric energy determined by integrating the electric field over the TEM cell volume, using Equation 2.22.

5.3 Loop antenna

5.3.1 Setup

A loop antenna is the most basic form of an antenna generating a mangetic dipole moment.

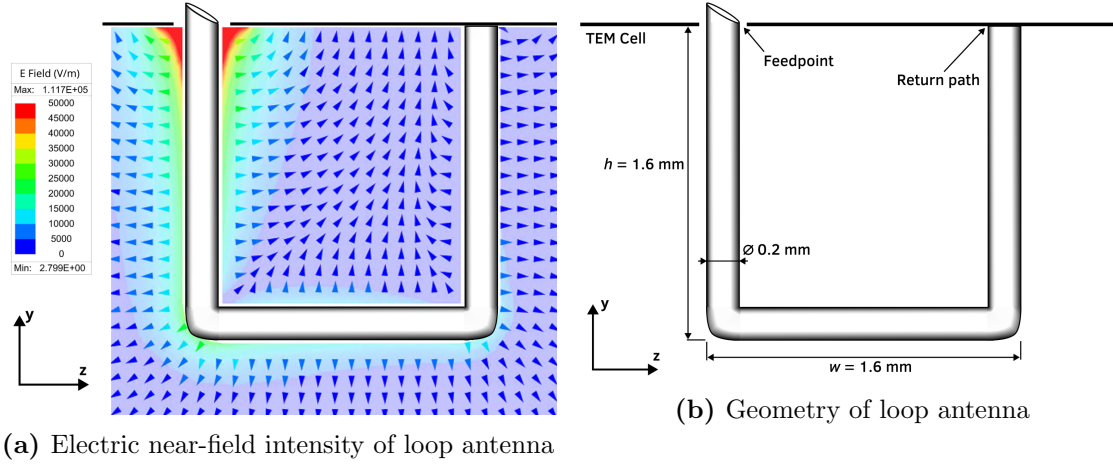
A square loop antenna is placed in the center of the TEM cell. It consists of four wires with a length of 1.6 mm each, and it is electrically short for frequencies up to 4.69 GHz. The square geometry is preferable to a round version in the numerical simulations, as it allows for more accurate meshes and enables a clearer investigation of the resulting dipole moments.

The normal vector of the loop surface points in x-direction, leading to a maximum coupling with the magnetic field of the TEM-mode. In contrast to the monopole antenna discussed in Section 5.2, a return path for the current exists, which generates a magnetic dipole moment.

5.3.2 Equivalent dipole moments

The equivalent dipole moments of the loop antenna are plotted in Figure 5.20a. The magnetic dipole moment \mathbf{m}_m dominates over the electric dipole moment \mathbf{m}_e . Opposed to the case of a monopole antenna, \mathbf{m}_e and \mathbf{m}_m demonstrate non-linear behavior over frequency, which is investigated further in Section 5.3.3.

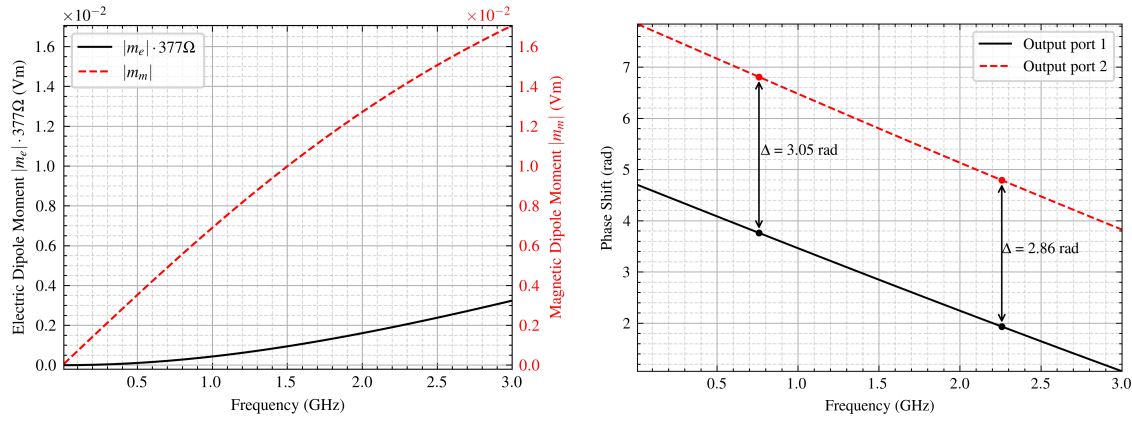
Furthermore, the phases of the powers at the output ports, shown in Figure 5.20b, differ from one another. The phase shift in the low-frequency range approaches π , but gradually decreases with increasing frequency. This agrees with the analysis presented in Section 3.4.2, which predicts a phase shift of π when only \mathbf{m}_m is present, and a reduced phase shift as \mathbf{m}_e increases, as is the case here.



(a) Electric near-field intensity of loop antenna

(b) Geometry of loop antenna

Figure 5.19 The geometry of the loop antenna assimilates a square with round edges. The height and width of the antenna equal $h = w = 1.6$ mm. The return path leads back to the PEC surface of the TEM cell. The electric near-field shows large a displacement current and voltage drop near the feed-point. It has been derived with a refined mesh on the antenna surface and near the feedpoint, according to the discussion in Section 5.1.5.



(a) Equivalent dipole moments

(b) Phase of the power at each output port

Figure 5.20 The equivalent dipole moments of the loop antenna are derived analytically with Equations (3.44a) to (3.44b), where the electric dipole moment \mathbf{m}_e is weighted with Z_0 to enable comparison with \mathbf{m}_m . The phases of the powers at output ports 1 and 2 are derived from the S-parameters, as discussed in Section 5.1.7. The analysis specifically focuses on the phase shift between the two ports, which provides information about the presence of \mathbf{m}_m and \mathbf{m}_e , as investigated in Section 3.4.2.

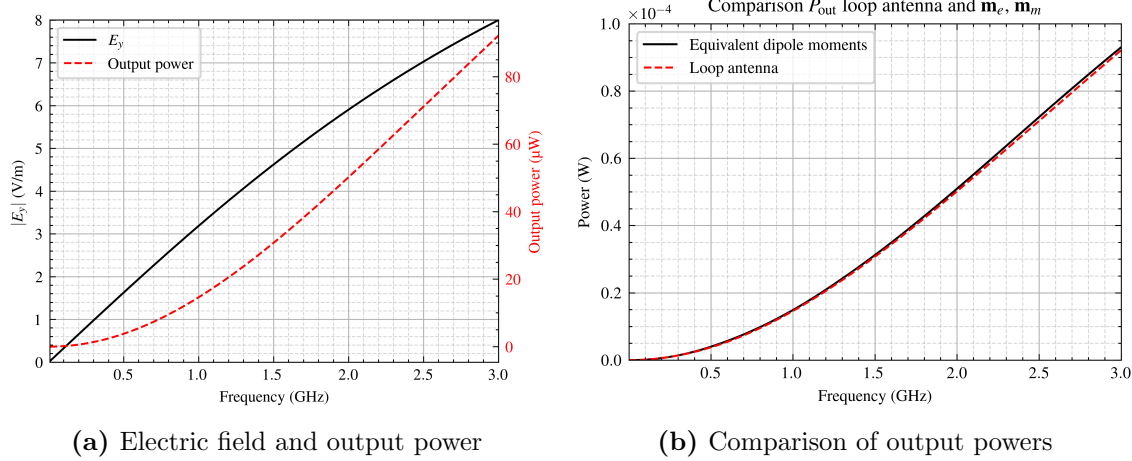


Figure 5.21 Electric field in y-direction E_y at $x = 0, y = b/4, z = \pm l/2$, and the closely related power at one of the output ports, derived with the S-parameters in Equation 5.5. The output power produced by the loop antenna is compared with that generated by the equivalent dipole moments.

The power and E_y induced by the loop antenna at the output ports is shown in Figure 5.21a, and increases not as steeply as the output power of the monopole antenna exhibited in Figure 5.12a. This directly correlates with the decrease of \mathbf{m}_m with increasing frequency.

Figure 5.21b demonstrates the output power generated by the equivalent dipole moments \mathbf{m}_m , \mathbf{m}_e and the loop antenna. Their similarity support the validity of the model used.

5.3.3 Electrical characteristics

Calculating the electric and magnetic energy in the radiation boundary, as discussed in Section 2.3.2.

The current I in the loop antenna changes along the antenna wire as shown in Figure 5.23a, indicating displacement current coupling to the septum and back to the feedpoint. The difference between the feedpoint and return path current increases over frequency, translating to rising displacement currents. Furthermore, the decrease in feed current over rising frequency, shown in Figure 5.23a, also hints to the presence of increasing displacement currents. Consequently, \mathbf{m}_e gains a significant magnitude according to Equation 3.54, increasing the electric coupling of the antenna to the TEM cell.

The feedpoint current is derived with Equation (5.11), through integration of \mathbf{H} in a closed loop of radius 0.11 mm, measured 0.17 mm above the feedpoint. The return path current is processed with the same loop integration at the same height above the PEC surface. The results vary with height above the PEC surface due to the displacement currents in the near-field.

Figure 5.23a demonstrates the voltage at the feedpoint of the antenna, which significantly rises over the frequency, signaling increased induced voltage V_n . According to Equa-

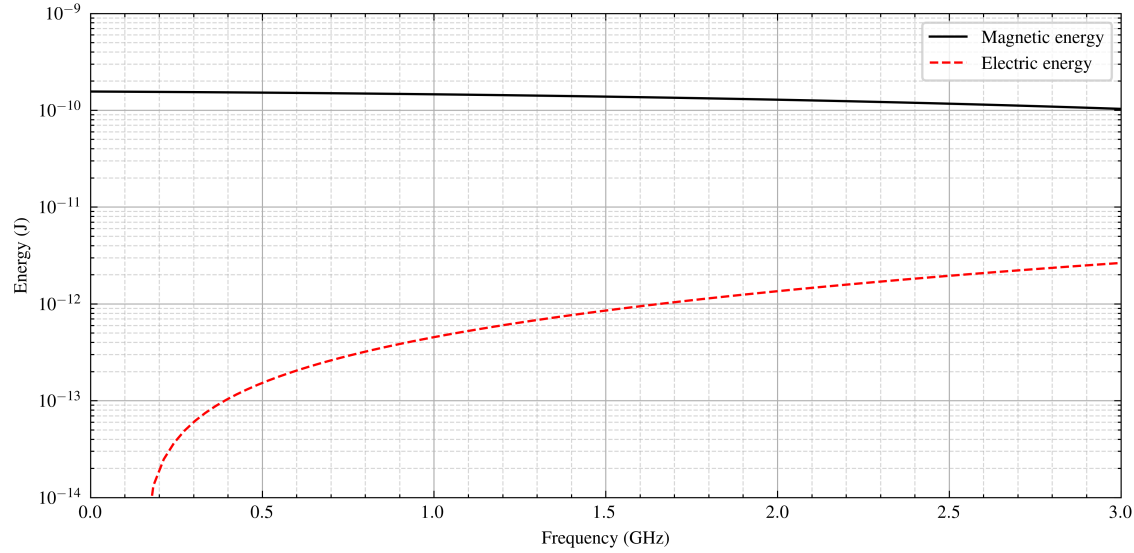


Figure 5.22 Electric and magnetic energy produced by the loop antenna in the TEM cell, derived with Equation 2.22 in the TEM cell volume.

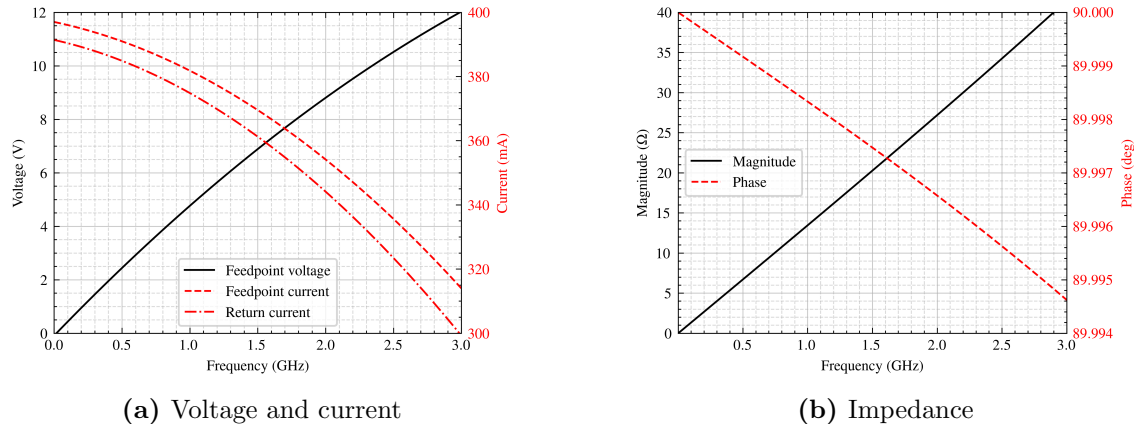


Figure 5.23 This figure demonstrates the voltage, current and impedance characteristics of the loop antenna. The difference between the current near the feedpoint and that on the return path increases with frequency, indicating a growing occurrence of displacement currents. The current on those paths are determined through magnetic near-field intensity, using Equation 5.11. The voltage across the feedpoint is obtained using Equation 5.8. Magnitude and phase of the impedance of the loop antenna are determined with Equation 5.9.

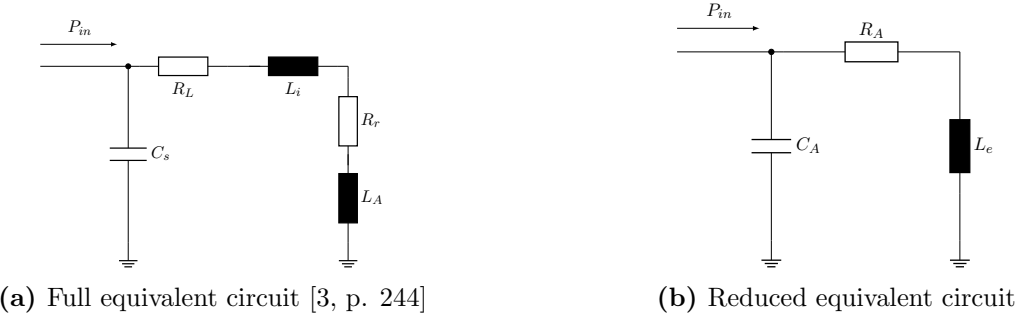


Figure 5.24 Equivalent circuits of the small loop antenna.

tion 3.48, this directly correlates with \mathbf{m}_m , which furthermore becomes apparent when comparing their behavior shown in Figures 5.20a to 5.23a. The increase in voltage also correlates with the displacement current. It raises the potential on the loop antenna, therefore increasing the charge distributions and displacement currents.

The increases in voltage and decrease in current agrees with the impedance, depicted in Figure 5.23b. The loop antenna shows strongly inductive behavior.

5.3.4 Equivalent circuit model

Equivalent circuit models of the antenna and the TEM cell are valuable tools for further analysis, as they enable analytical calculations and facilitate investigation and understanding of the observed coupling behavior.

Figure 5.24a demonstrates an equivalent circuit for the electrically small loop antenna in free space [3, p. 244], where

- C_s Stray capacitance of the loop antenna
- R_L Ohmic loss resistance of the antenna conductor
- R_r Radiation resistance of the loop antenna
- L_i Internal inductance of the loop antenna
- L_e External inductance of the loop antenna

As discussed in Section 5.1.2, the antenna is modeled as a perfect electric conductor, therefore R_L and L_e are neglected. Instead, the simplified equivalent circuit in Figure 5.24b is applied, where R_A , L_A and C_A represent the impedance behavior of the antenna.

To determine R_A , L_A and C_A , the antenna model is placed on a PEC surface in an open space, as demonstrated in Figure 5.25. The inductance and capacitance are derived according to Equations (2.23a) to (2.23b), which leads to

$$L_A = 2 \frac{W_m}{I_{LA}^2} = \frac{V_{in}^2}{2\omega^2 W_m}, \quad (5.12a)$$

$$C_A = \frac{2W_c}{V_{in}^2}, \quad (5.12b)$$

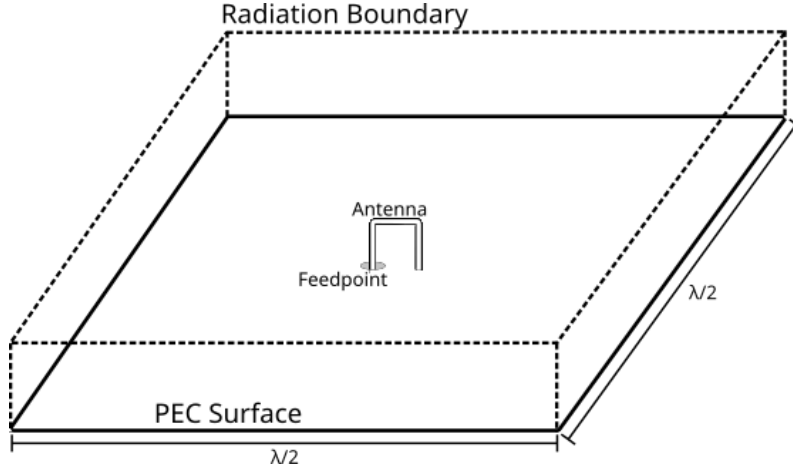


Figure 5.25 Loop antenna in free space on PEC plane

Figure 5.26 Model of the loop antenna connected to a feedpoint mounted on a PEC surface with a side length of $\lambda/2$, where λ corresponds to the free-space wavelength of the solution frequency. This configuration enables the investigation of the loop antenna reactance without influence of the TEM cell.

where $I_{LA} = V_{in}/(j\omega L_A)$ denotes the current through the inductor L_A . The resulting capacitance and inductance equal $C_A = 38.2 \text{ fF}$ and $L_A = 2.14 \text{ nH}$. The capacitance C_A is less pronounced than the inductance L_A of the antenna, which supports the inductive impedance demonstrated in Figure 5.23b.

The resulting L_A is compared with

$$L_{sq} = \frac{2\mu_0 l}{\pi} \left[\ln\left(\frac{l}{w_r}\right) - 0.774 \right], \quad (5.13)$$

which provides an approximation for the inductance of a square loop antenna in free-space [3, p. 245]. In this expression, l denotes the length of one side of the loop antenna and w_r the wire radius. For the loop antenna in investigation, Equation 5.13 yields $L_{sq} = 2.32 \text{ nH}$, which is comparable to the previously obtained L_A .

Check: Does this formula consider external inductances?

The model is extended in Figure 5.27 with an equivalent circuit representing the TEM cell, which consists of a TEM cell inductance $L_T = L_{T1} + L_{T2}$ and capacitance $C_T = C_{T1} + C_{T2}$. The part inductances $L_{T1} = L_{T2}$ and capacitances $C_{T1} = C_{T2}$ are of equal values and are split for symmetry purposes. Special care must be taken to ensure that the model is applied within the valid frequency range of the TEM cell equivalent circuit model. The equivalent circuits of the antenna and the TEM cell are coupled via C_k , which models the displacement current coupling, and the mutual inductances $M_{A,T1}$ and $M_{A,T2}$, which account for coupling through induced voltages. The mutual inductances are given by

$$\mathbf{V} = j\omega \begin{bmatrix} L_A & M_{A,T1} & M_{A,T2} \\ M_{T1,A} & L_{T1} & 0 \\ M_{T2,A} & 0 & L_{T2} \end{bmatrix} \mathbf{I}. \quad (5.14)$$

Due to the modeling of the power transfer with C_k , $M_{A,T1}$ and $M_{A,T2}$, the radiation resistance of the antenna shown in Figure 5.24b is neglected.

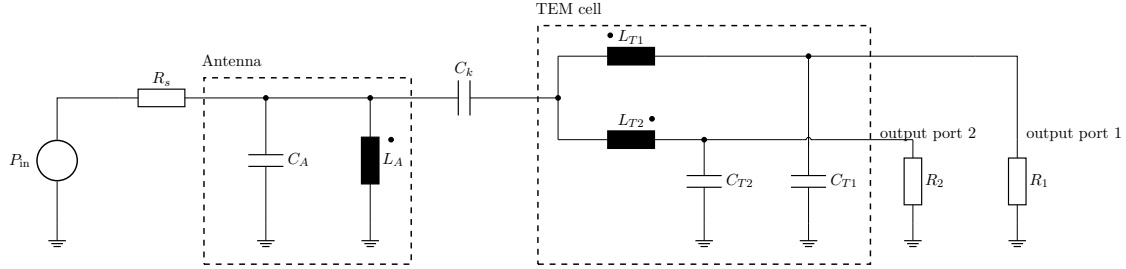


Figure 5.27 Circuit representing the TEM cell and the loop antenna, with the additional components C_k and $M_{A,T1}$, $M_{A,T2}$ modeling their near-field coupling behavior.

The magnetic dipole moment \mathbf{m}_m is derived by the induced voltage in L_{T1} and L_{T2} according to Equation 3.48, and the electric dipole moment \mathbf{m}_e by the displacement current in C_k through Equation 3.54. This results in \mathbf{m}_e and \mathbf{m}_m depicted in Figure 5.28, which are similar to the dipole moments derived by the simulator in the high-frequency range, but accuracy recedes in the low-frequency range.

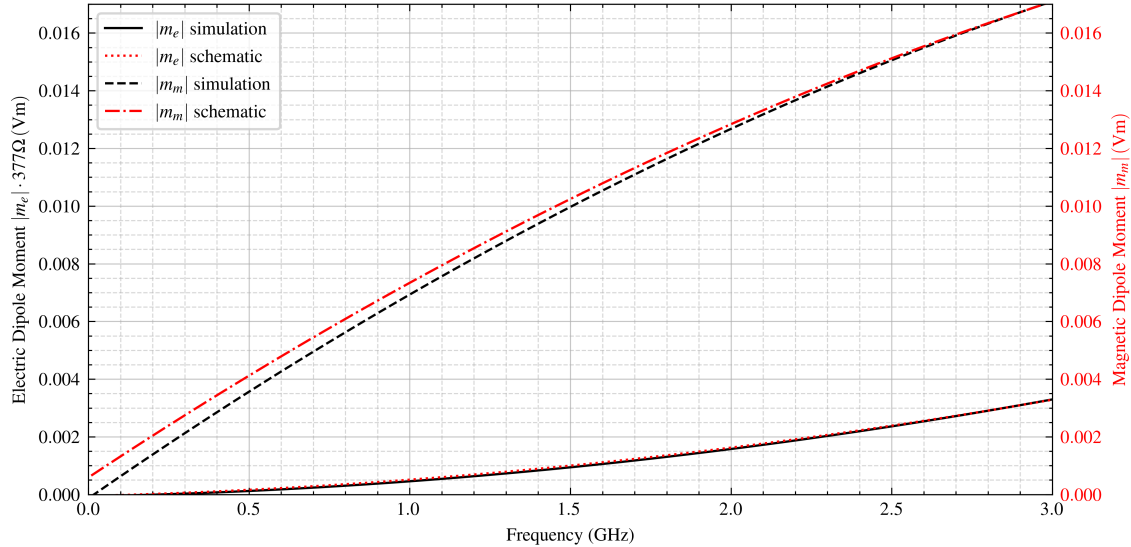


Figure 5.28 Equivalent dipole moments derived by the equivalent circuit depicted in Figure 5.27, compared to the dipole moments of the loop antenna, shown in Figure 5.20a. The electric dipole moment \mathbf{m}_e is weighted with Z_0 for comparison purposes.

The equivalent circuit of the loop antenna shown in Figure 5.24b can also be used to reason about the coupling behavior of the antenna. In particular, the voltage induced across the

inductance V_n is related to the displacement current I_n by

$$\frac{I_n}{V_n} = \frac{j\omega Q}{R_A\omega_0^2 + j\omega L\omega_0^2 - R_w\omega^2}, \quad (5.15)$$

where $\omega_0 = 1/\sqrt{L_A C_A}$ denotes the resonance frequency, $Q = \omega_0 R_w C_A$ the Q-factor of the equivalent circuit and R_w the real characteristic impedance of the antenna feedpoint. Since V_n and I_n are directly associated with the magnetic and electric dipole moments \mathbf{m}_m and \mathbf{m}_e through Equations (3.48) to (3.54), the electric and magnetic coupling behavior of the small loop antenna can be directly linked to its resonance frequency and Q-factor.

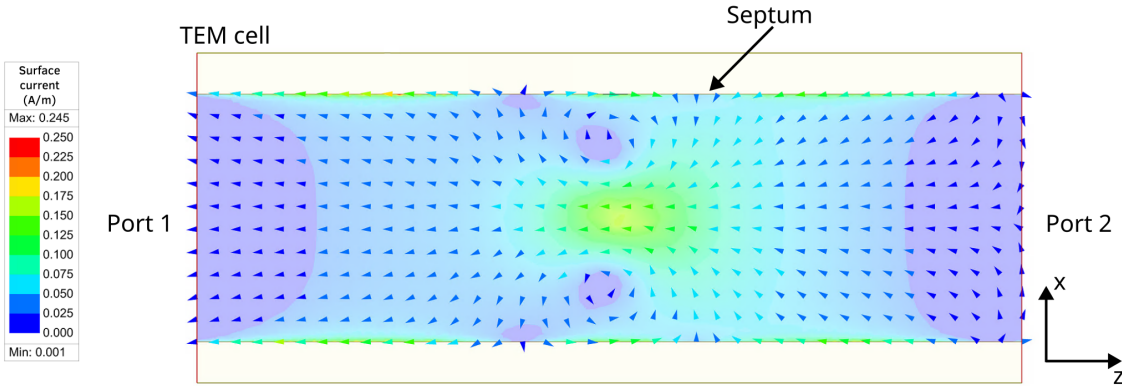
A lower resonance frequency ω_0 , higher Q-factor Q or capacitance C_A results in a more pronounced non-linear frequency-behavior of \mathbf{m}_m and \mathbf{m}_e . Furthermore, increased capacitance lowers the resonance frequency ω_0 toward the investigated frequency range and increases the antenna's electrical length [1], both attributing in increased radiated power.

5.3.5 Current distribution on septum and higher order modes

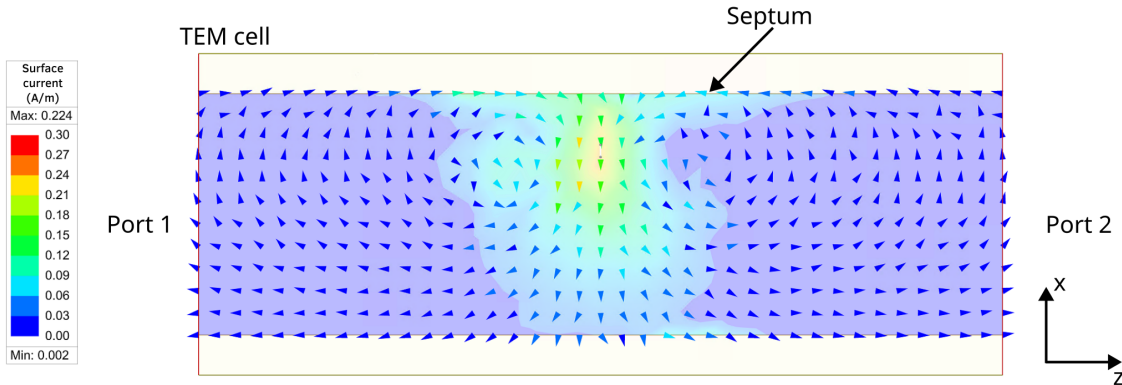
The radiating loop antenna induces surface currents on the septum of the TEM cell, as shown in Figure 5.29. At a frequency of 3 GHz, the currents reaching the output ports are out of phase, as illustrated in Figure 5.29a. This observation is consistent with the analysis in Section 3.4.2, which predicts a phase shift of $\pm\pi$ between the output port powers in the presence of a magnetic dipole moment.

When the antenna is rotated by $\pm\pi/4$ and offset by $x = 7$ mm, power transmission at 3 GHz is insignificant. According to Equations (3.47a) to (3.47b) and Equation 3.48, efficient coupling requires the magnetic field intensity of the propagating TEM mode $\mathbf{h}_{\text{TEM}}^\pm$ to be aligned with the vector normal to the antenna surface. The current distribution Figure 5.29b demonstrates no excited waves in this configuration. Instead, the power produced by the surface current remains reactive, forming closed circulation patterns around the induced magnetic fields.

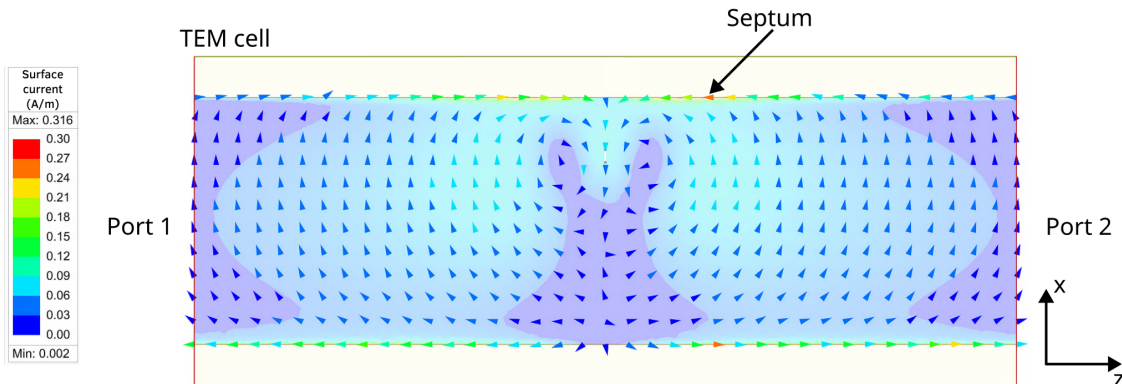
At a frequency of 3.3 GHz, the TE₀₁ mode propagates in the TEM cell. In this case, $\mathbf{h}_{\text{TE}01}^\pm$ aligns with the normal vector of the offset and rotated loop antenna surface. As shown in Figure 5.29c, a significant proportion of the current now reaches the output ports, resulting in transmission of power. In contrast to the previous case, the output powers are in-phase, as discussed in Section 3.4.2. The output power transmitted by the TE₀₁ mode increases sharply with frequency, as demonstrated in Figure 5.30.



(a) The centrally located loop antenna without offset or rotation at a frequency of 3 GHz, where mainly the TEM mode propagates.



(b) Loop antenna with offset of $x = 7$ mm and a $\pi/4$ rotation angle at 100 MHz, where only the TEM mode propagates. The currents passing to the output ports are negligible.



(c) Loop antenna with offset of $x = 7$ mm and a $\pi/4$ rotation angle at 3.3 GHz, where the TEM and TE₀₁ modes both propagate. The currents passing to the output ports produce significant power, as shown in Figure 5.30.

Figure 5.29 Surface current density on the septum induced by the loop antenna for different frequencies and positions of the antenna.

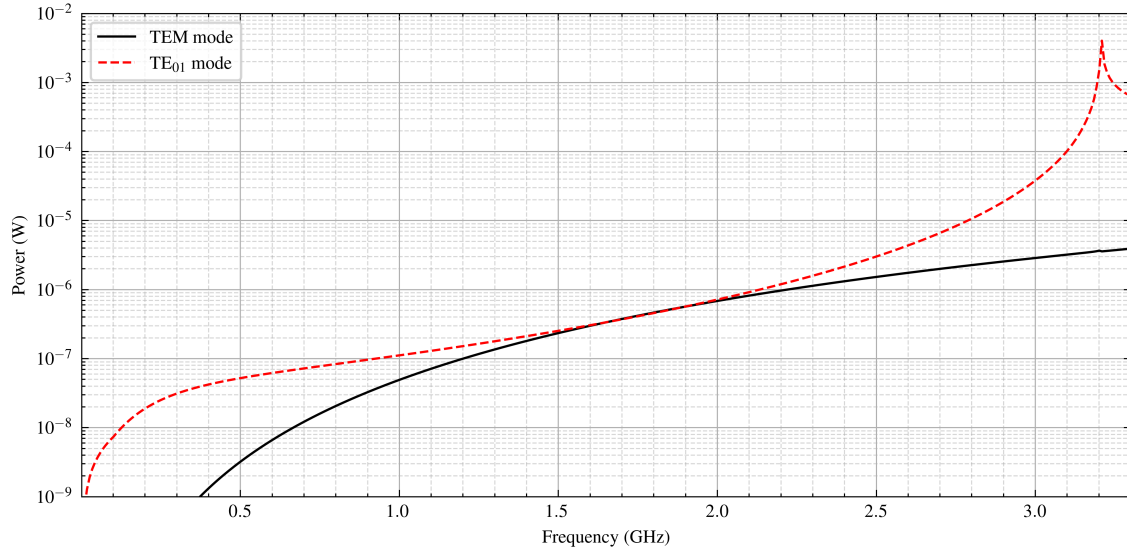


Figure 5.30 Output power transmitted by the antenna to the output port through the TEM and TE₀₁ modes, separately over frequency, determined through the S-parameters with Equation 5.5. At a frequency of $f = 3.21$ GHz a resonance in the TEM cell occurs, leading to the visible peak in the output power produced by the TE₀₁ mode.

5.3.6 Influence of antenna's geometry

The influence of the antenna's geometry on coupling behavior is investigated. The height h and width w of the loop antenna presented in Figure 5.19b is varied, and their dipole moments and power consumption compared in Figures 5.31a to 5.31b.

The loop area is identical in both configurations presented. Consequently, the behavior of the magnetic dipole moments \mathbf{m}_m are the same in both cases, which agrees with Equations (3.47a) to (3.47b). Nonlinear frequency dependence of \mathbf{m}_m persists in both configurations, due to the nearly constant capacitance of the antenna.

The electric dipole moment \mathbf{m}_e is strongly dependent on the antenna height h . The antenna with a height of $h = 2.16$ mm generates an electric dipole moment \mathbf{m}_e , more than twice as large as that of the antenna with $h = 1.2$ mm, as depicted in Figure 5.31a. This result supports validity of the used models and is consistent with Equation 3.54, which relates the displacement current between the antenna and septum to the electric dipole moment \mathbf{m}_e . Lastly, the output power produced by the antenna generating the larger electric dipole moment \mathbf{m}_e is also greater, as shown in Figure 5.31b.

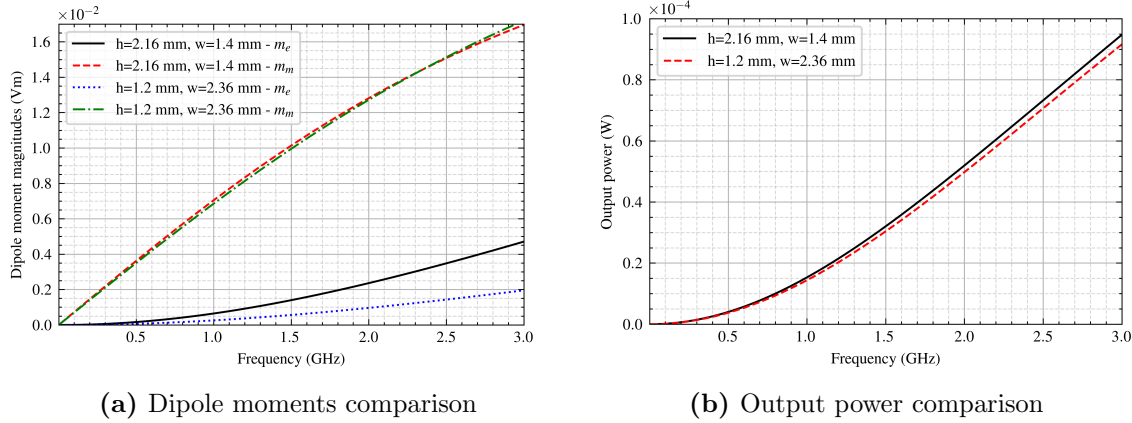


Figure 5.31 Dipole moments and output power comparisons of two different loop antenna configurations presented, one with $h = 2.16 \text{ mm}$, $w = 1.4 \text{ mm}$ and the other with $h = 1.2 \text{ mm}$, $w = 2.36 \text{ mm}$. The electric dipole moment \mathbf{m}_e is weighted with Z_0 for comparison purposes.

5.4 Loop antenna with gap

5.4.1 Setup and geometrical analysis

The geometry of the loop antenna with a gap is similar to that of the loop antenna discussed in subsection 5.3. It is electrically short for frequencies up to 4.69 GHz. A gap with a height of 10 μm is introduced in the return path, as shown in Figure 5.32b. The gap is intentionally kept small to emphasize specific coupling mechanics and to demonstrate the consistency of antenna analysis with the framework developed in this thesis, although such a small gap would be hard to implement in a physical antenna. Furthermore, manual mesh refinement is necessary around the gap region, as well as the feedpoint and the curved surfaces, as discussed in subsubsection 5.1.5.

The magnetic coupling is determined with Equations (3.47a) to (3.47b), just as is the case for the normal loop antenna. However, considering the gap region leads to

$$-\oint_C \boldsymbol{\tau} I(l) \cdot \mathbf{e}_n^\pm dl = - \int_{\text{wire}} \boldsymbol{\tau} I_{\text{wire}}(l) \cdot \mathbf{e}_n^\pm dl - \int_{\text{gap}} \boldsymbol{\tau} I_{\text{gap}}(l) \cdot \mathbf{e}_n^\pm dl. \quad (5.16)$$

The electric current across the gap is $I_{\text{gap}} = 0 \text{ A}$, while the current in the antenna wire I_{wire} is significantly reduced due to the interrupted current path. Consequently, the magnetic coupling between the loop antenna with a gap and the TEM cell is expected to be weaker than that of the loop antenna without a gap, but still more present than the monopole antenna discussed in subsection 5.2. Furthermore, reducing the gap height increases magnetic coupling and the magnitude of the magnetic dipole moment \mathbf{m}_m , attributable to the correlated increase of I_{wire} .

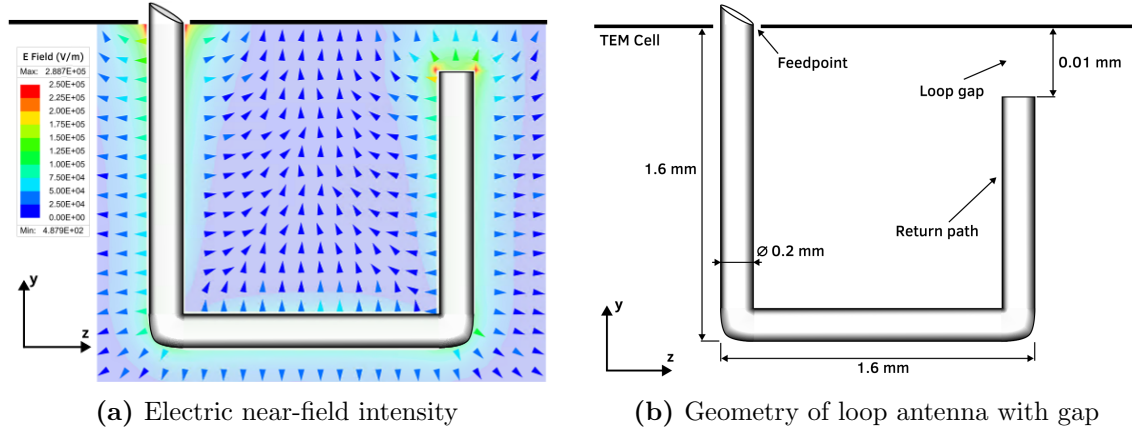


Figure 5.32 Geometry of the loop antenna with a gap in the return path inserted in the TEM cell. The gap height is exaggerated for demonstration purposes.

The conductors adjacent to the gap behave as capacitors plates, accumulating charges on both either side. According to Equations (3.53a) to (3.53b), these accumulated charges lead to electric coupling with the septum. A smaller gap height increases the amount of accumulated charges, and consequently leads to an increase in the electric dipole moment \mathbf{m}_e . Lastly, the absence of a conductive return path for the current leads to expect capacitive behavior of this electrically small antenna, similar to the monopole antenna analyzed in subsection 5.2.

5.4.2 Equivalent dipole moments

The equivalent dipole moments of the loop antenna with gap are shown in Figure 5.33a, where the electric dipole moment \mathbf{m}_e is larger than the magnetic dipole moment \mathbf{m}_m . The dipole moments behave non-linearly over the frequency.

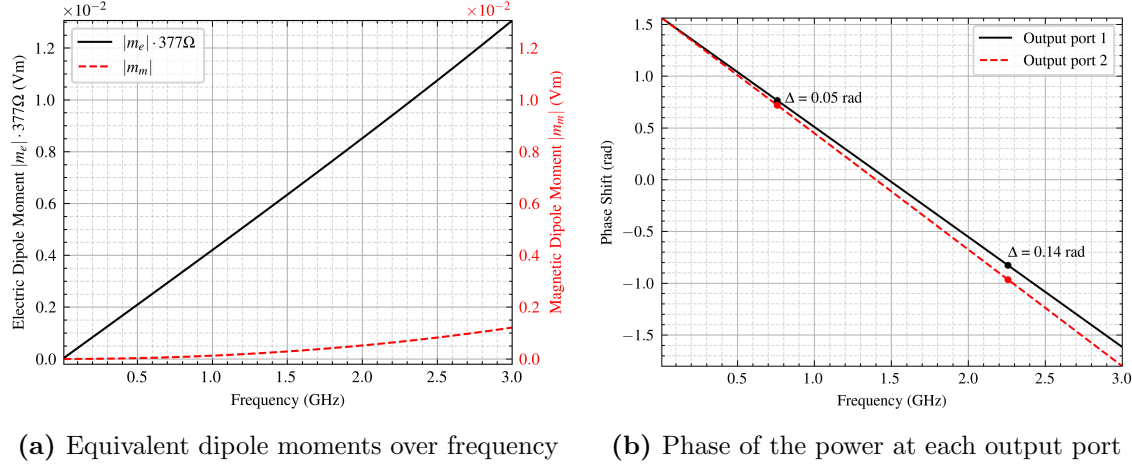
Figure 5.34a demonstrates the effect of the gap height on the dipole moment behavior. As discussed in subsubsection 5.4.1, the reduction of the gap height leads to an increase of both dipole moments, \mathbf{m}_e and \mathbf{m}_m . Their magnitudes correlate with the output power, as shown in Figure 5.34b.

An increase in gap height reduces the non-linearities in \mathbf{m}_e and \mathbf{m}_m . The voltage drop across the gap and the charge accumulation remains more stable over frequency.

5.4.3 Electrical characteristics

The impedance of the loop antenna with gap is capacitive, shown in Figure 5.35b. The inductance of this antenna is not negligible, opposed to the case of the monopole antenna in subsection 5.2. This causes a significant magnitude of \mathbf{m}_m in Figure 5.33a and a stronger decline in impedance magnitude of the loop antenna with gap, compared to the monopole antenna's impedance, demonstrated in Figure 5.11b.

The feedpoint voltage decreases more rapidly over frequency compared to that of the monopole antenna, see Figures 5.35a to 5.23a. This behavior is a direct result of increased



(a) Equivalent dipole moments over frequency (b) Phase of the power at each output port

Figure 5.33 The equivalent dipole moments of the loop antenna with a gap, where the electric dipole moment \mathbf{m}_e is weighted with Z_0 to enable comparison with \mathbf{m}_m . The phases of the powers at output ports 1 and 2 are derived from the S-parameters, as discussed in Section 5.1.7. The analysis specifically focuses on the phase shift between the two ports, which provides information about the presence of \mathbf{m}_m and \mathbf{m}_e , as investigated in Section 3.4.2.

induced voltage, which correlates with the pronounced magnetic dipole moment \mathbf{m}_m , according to Equation 3.48. Furthermore, the feed current increases more slowly, resulting in a slower growth of the electric dipole moment \mathbf{m}_e with frequency, according to Equation 3.54. The magnitude of \mathbf{m}_e is additionally smaller than that of the monopole in Figure 5.10.

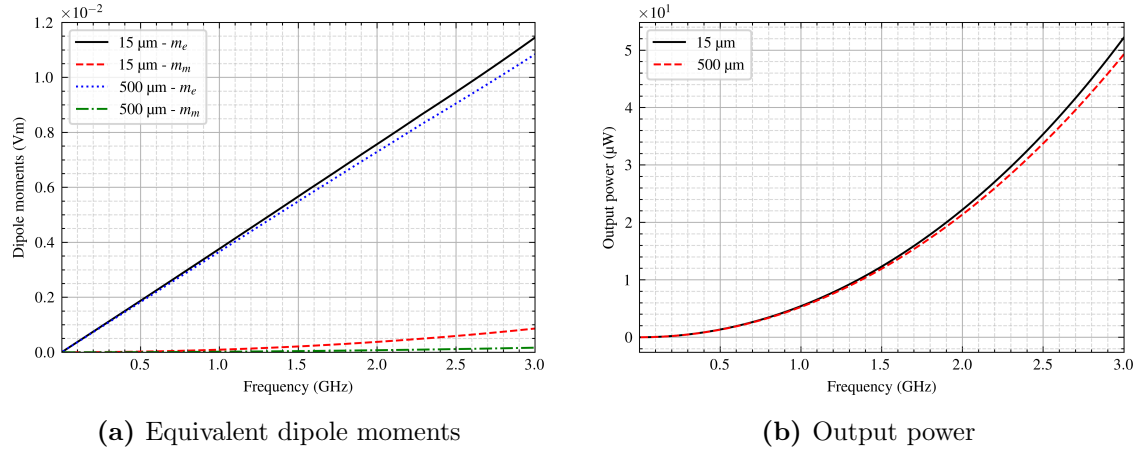


Figure 5.34 Comparison of dipole moments, where the electric dipole moment \mathbf{m}_e is weighted with η_0 to enable comparison with \mathbf{m}_m , and output power for different gap heights in the loop antenna.

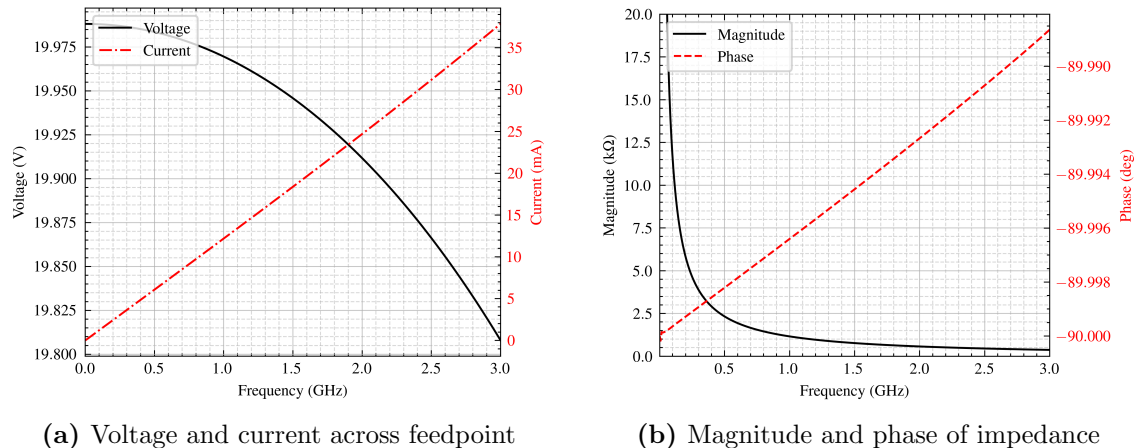


Figure 5.35 The voltage and current across the feedpoint, together with the related impedance of the loop antenna with gap.

5.5 Inverted-F and center-fed monopole antenna

5.5.1 Setup and geometrical analysis

The inverted-F antenna (IFA) and center-fed monopole antenna (CFM), shown in Figures 5.36a to 5.36b, are presented here together, because of their related geometry and similar electromagnetic behavior. Both have a maximum dimension of 5 mm, and are electrically small at frequencies up to 6 GHz. They exhibit an inductive nature, hence a similar behavior as the loop antenna in subsection 5.3 is expected. Both antennas consist of a loop of identical area to the loop antenna discussed in Section 5.3, to which a linear arm is connected. In the CFM, this arm is oriented toward the TEM cell septum, whereas in the IFA it is directed toward an output port.

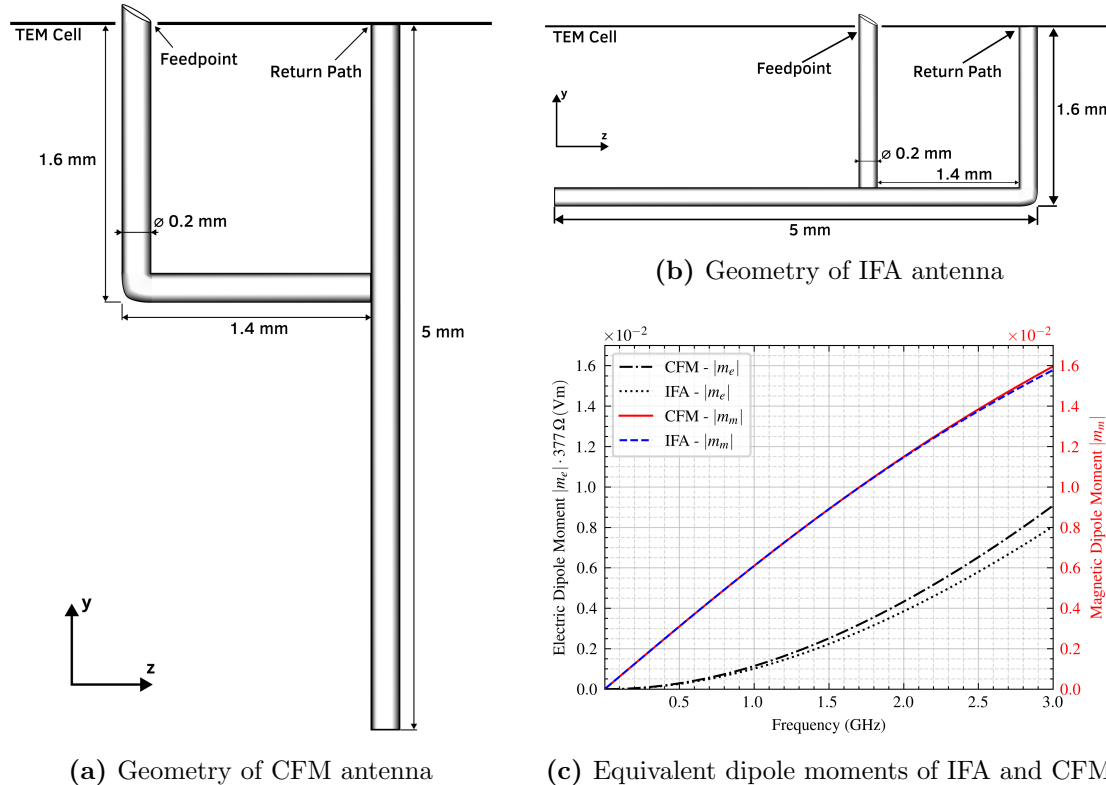


Figure 5.36 Geometries of IFA and CFM antenna, together with their equivalent dipole moments. the electric dipole moment \mathbf{m}_e is weighted with the free space impedance Z_0 to enable comparison with the magnetic dipole moment \mathbf{m}_m .

5.5.2 Equivalent dipole moments

The magnetic dipole moments \mathbf{m}_m of the CFM and IFA presented in Figure 5.36c are comparable to each other, but are smaller in magnitude than that of the loop antenna shown in Figure 5.20a. This reduction can be attributed to the linear arms of the CFM and IFA, which introduce additional capacitance. The increased capacitance enhances the displacement current while reducing the induced voltage. According to Equations (3.48)

to (3.54), this results in a decrease of magnetic dipole moment \mathbf{m}_m and an increase of the electric dipole moment \mathbf{m}_e .

Furthermore, for small loop and inductive antennas in general, Equation 5.15 predicts that an increase in capacitance leads to a stronger non-linear frequency dependence of both \mathbf{m}_m and \mathbf{m}_e . This assumption is confirmed by comparing the dipole moments of the loop antenna with those of the CFM and IFA, shown in Figures 5.20a to 5.36c.

6 Application of Shielding Techniques in TEM Cells

6.1 ASTM ES7-83 method

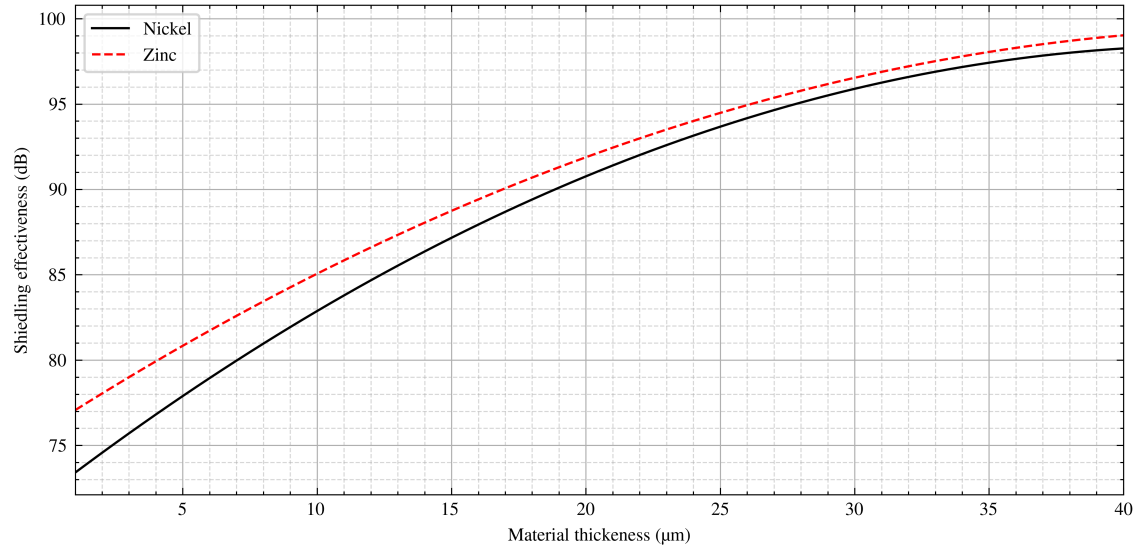


Figure 6.1 Shielding effectiveness of a sheet of zinc and nickel versus the material thickness determined with the ASTM ES7-83 Method.

A model as described in subsubsection 3.5.3 is used to determine the shielding effectiveness of barium titanate and ferrite according to the ASTM ES7-83 method discussed in Section 3.5.3. The TEM cell contains a shielding material sheet with a thickness of $10 \mu\text{m}$ in the center of the TEM cell at $z = 0$, which is modeled with impedance boundary conditions as discussed in Section 5.1.6. A reference power of $P_{\text{ref}} = 1 \text{ W}$ is chosen and the load power P_{load} is numerically derived. Equation 3.67 yields the shielding effectiveness SE_{dB} of the material depending on frequency. The investigated frequency is 1 GHz.

The properties of the materials used are listed in Table 6.1. Ferrite additionally is modeled to have a magnetic loss tangent of $\tan \delta_m = 0.05$.

Material	Rel. permittivity ϵ_r	Rel. permeability μ_r	Conductivity σ
Ferrite	≈ 12	$\approx 1,000$	0.01 S/m
Barium titanate	$\approx 2,000$	≈ 1	$3.64 \cdot 10^{-11}$ S/m

Table 6.1 Electromagnetic Properties of barium titanate and ferrite

6.2 Dual TEM cell

A simulation model of two TEM cells as shown in Figure 3.14, consisting of the models demonstrated in Section 5.1.3, without the tapered sections, is created. An empty square aperture with a side length of $d = 10$ mm is used, which makes it electrically small up to a frequency of approximately 3 GHz. The largest numerical error stems from insufficient mesh size in the aperture region, hence 10 to 15 mesh elements across the aperture are aimed for. The procedure described in Section 3.5.4 is applied to derive the electric and magnetic shielding effectiveness of, again, ferrite and barium titanate (BaTiO_3).

Port 1 excites the waveguides with a power of 1 W. The sum $P_{\text{ref,sum}}$ and difference $P_{\text{ref,diff}}$ of the powers arriving at port 3 and 4 is demonstrated in Figure 6.2, which is calculated using [31]

$$P_{\text{sum}} = (a + b)(a + b)^*, \quad (6.1a)$$

$$P_{\text{diff}} = (a - b)(a - b)^*, \quad (6.1b)$$

where a and b are the amplitudes of the fields at port 3 and 4, respectively.

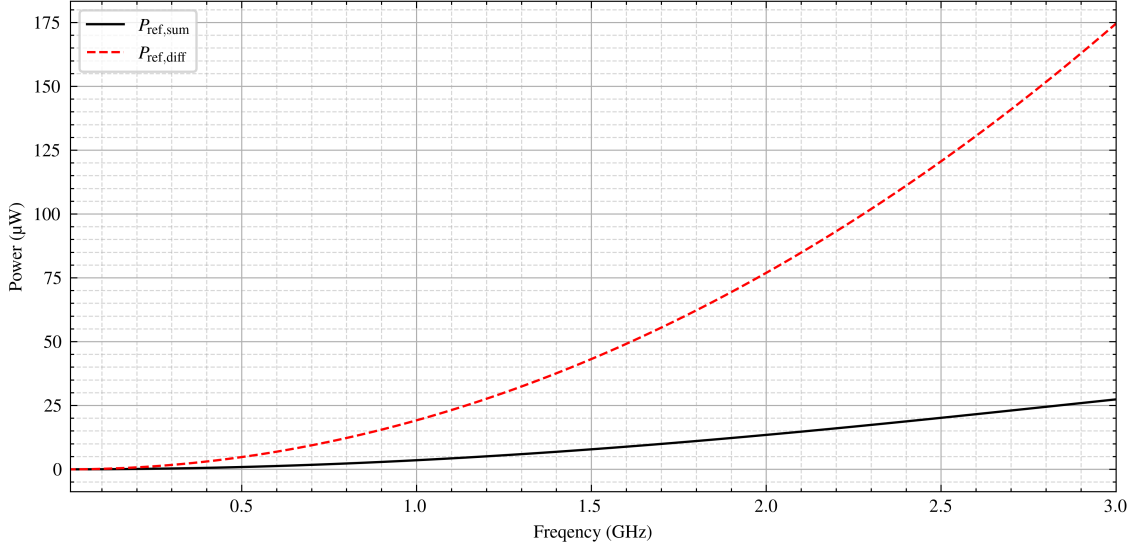


Figure 6.2 The sum $P_{\text{ref,sum}}$ and difference $P_{\text{ref,diff}}$ of the reference power, measured with empty aperture and calculated with the phase information considered.

Materials filling the aperture have a thickness of $t = 10$ μm.

When investigating highly conductive materials, applying skin-depth based meshing within the material enhances simulation accuracy while reducing computational effort. This approach refines the mesh especially near the material's surface, where rapid field variations occur. The skin depth is calculated as shown in Equation 5.2 and further discussed in Section 5.1.1. In contrast, both ferrite and barium titanate have a low conductivity, therefore, the mesh refinement of the aperture is instead achieved by setting a maximum mesh element length.

Again, the sum $P_{\text{ref,sum}}$ and difference $P_{\text{ref,diff}}$ of the powers at port 3 and 4 are derived and shown in Figures 6.3a and 6.3b, once for the aperture filled with barium titanate, and once with ferrite.

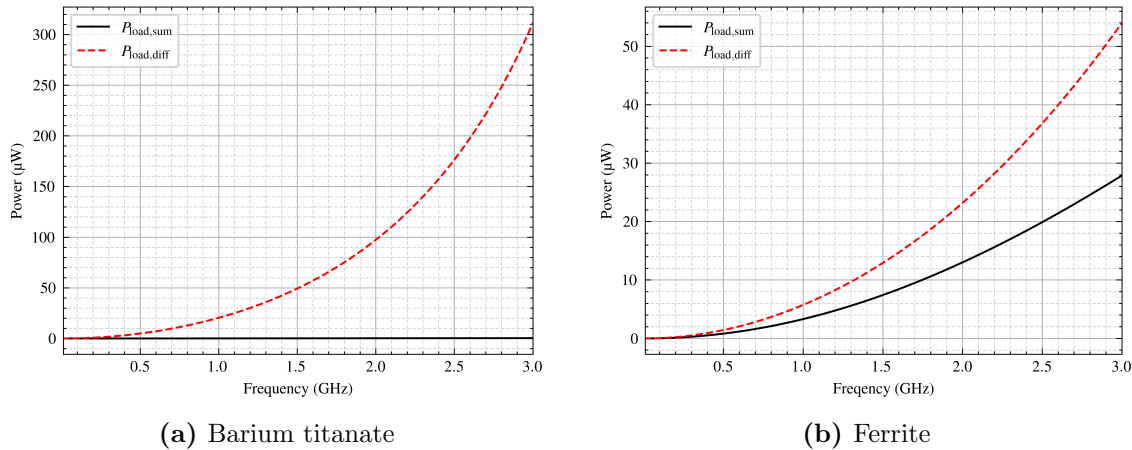


Figure 6.3 The sum $P_{\text{load,sum}}$ and difference in output power $P_{\text{load,diff}}$ measured at port 3 and 4 with the phase information considered.

Ferrite exhibits higher power transfer, indicating lower shielding effectiveness compared to barium titanate. Additionally, $P_{\text{load,sum}}$ is low for barium titanate, suggesting high electric shielding effectiveness, as indicated by Equation (3.69a). The power transfer of both materials increases with frequency, which can be attributed to the low bulk conductivity and slightly decreasing permittivity at higher frequencies. The electric and magnetic shielding effectiveness for both materials are illustrated in Figures 6.4a and 6.4b.

Barium titanate exhibits good electric shielding characteristics, but demonstrates a negative $SE_{\text{dB}}^{\text{m}}$ value, indicating poor magnetic shielding. Negative shield effectiveness values are possible, and occur due to interference patterns at the filled aperture, which cause a and the output power at port 3 to increase [37, 16, p. 63]. Ferrite, on the other hand, demonstrates a higher magnetic shielding effectiveness $SE_{\text{dB}}^{\text{m}}$, but a low or negative electric shielding effectiveness $SE_{\text{dB}}^{\text{e}}$.

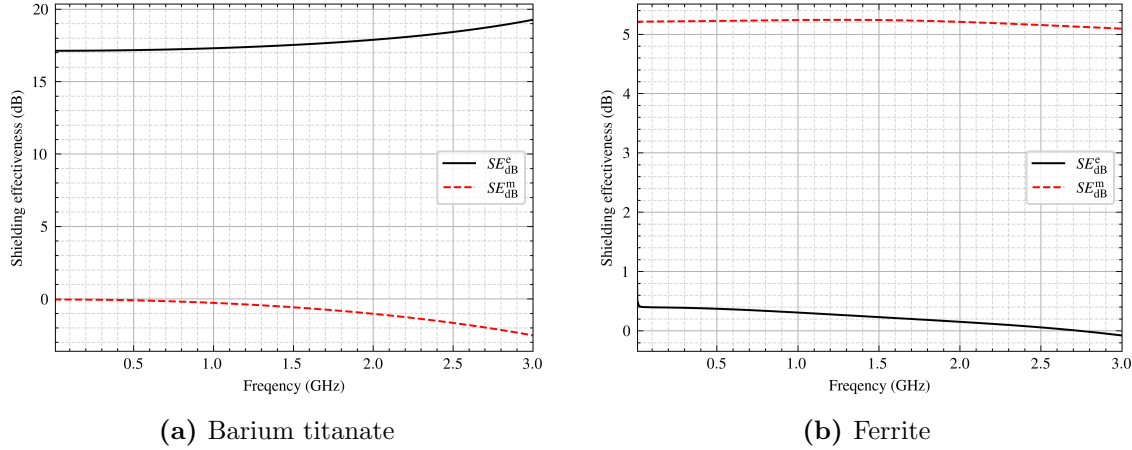


Figure 6.4 The electric SE_{dB}^e and magnetic SE_{dB}^m shielding effectiveness derived with Equations (3.69a) and (3.69b).

6.3 Antennas in shield enclosure

The loop and monopole antennas investigated in Sections 5.2 and 5.3 are shielded in a hollow enclosure, as shown in Figures 6.5a and 6.5b. The enclosure has a thickness of 10 µm, and all sides have a length of 6 mm.

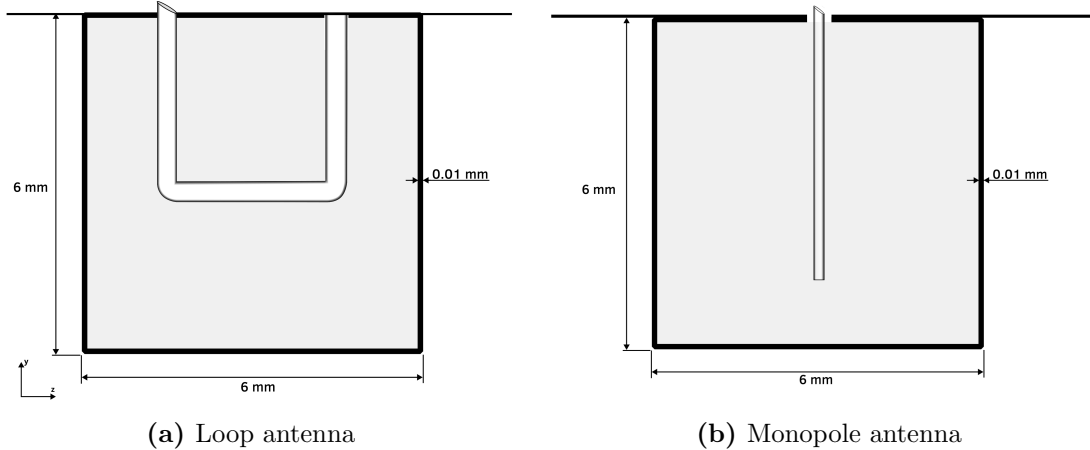


Figure 6.5 Investigated antennas placed in the TEM cell covered in a cubic, hollow enclosure.

Figure 6.6b shows the radiated power from the antennas with and without a barium titanate enclosure. The output power of the loop antenna increases because the barium titanate enclosure capacitively loads the antenna, resulting in a decrease in resonance frequency, which leads to a more efficient operating point of the antenna in the investigated frequency range, as discussed in Section 5.3. In contrast, the enclosure effectively shields against the monopole antenna's radiation. The results are consistent with the near-field region of the monopole antenna being predominantly electric (Equation 2.11), while that of the loop antenna is predominantly magnetic (Equation 2.19).

Similarly, Figure 6.6b shows the radiated power from the antennas with and without the ferrite enclosure. In this case, the output power of the monopole antenna increases due to the ferrite enclosure inductively loading the antenna. The enclosure serves as an effective shield against the loop antenna's radiation.

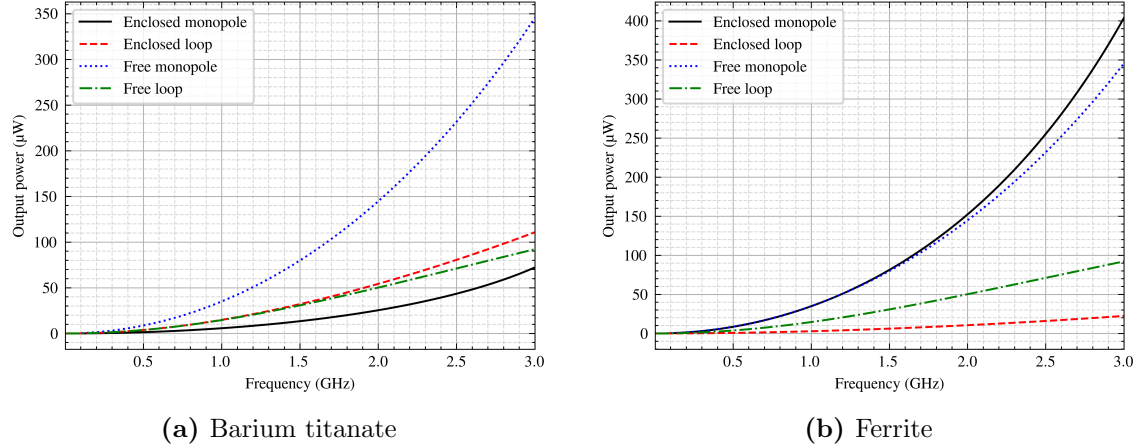


Figure 6.6 Output power over frequency produced by antennas with and without enclosure.

6.4 Dipole moments in shield enclosure

Next, the antennas in the enclosures are replaced with their equivalent dipole moments determined in Sections 5.2 and 5.3.

7 Conclusion

This thesis presents investigations of electrically small antennas and their coupling with a TEM cell using the finite element method. It further discusses applications of the framework created.

In this thesis, dipole moments equivalent to the electrically small antennas are calculated, whose magnitudes directly correlate with the electric and magnetic coupling of the antenna with the TEM cell. It finds, that the electric dipole moment correlates directly to the displacement current towards the septum, and the magnetic dipole moment to the voltage induced on the septum. An equivalent circuit model, both for capacitive and inductive antennas coupling to the TEM cell, is developed.

The relation of different geometrical and electrical antenna parameters to the equivalent dipole moments is investigated. An increase in Q-factor or decrease in resonance frequency of the antenna has been found to increase non-linear dipole moments frequency-behavior. The electric dipole moment generated by an antenna increases primarily with its physical height, due to increased displacement currents toward the septum. The magnetic dipole moment increases with the loop area normal to the magnetic field intensity of a propagating mode in the TEM cell. If the loop is not closed, a magnetic dipole moment can still exist due to curling electric field intensities $\nabla \times \mathbf{E} \neq 0$ forming perpendicular to the magnetic field intensity.

Further research could involve the measurement of such antennas with a real TEM cell, or the numerical analysis with other waveguides, such as the IC stripline. The framework in this thesis could be used to increase EMC of electronic systems containing electrically small, radiating structures, or represent them with dipole moments for less computational effort in complex simulation models.

References

- [1] In: *National Journal of Antennas and Propagation* 4.2 (2022). DOI: 10.31838/njap/04.02.07.
- [2] Constantine A. Balanis. *Advanced Engineering Electromagnetics*. John Wiley Sons, 2012.
- [3] Constantine A. Balanis. *Antenna theory: Analysis and design. Buch Constantine A. Balanis*. 3rd. Wiley, 1997.
- [4] C. Buccella et al. “Magnetic field computation in a physically large domain with thin metallic shields”. In: *IEEE Transactions on Magnetics* 41.5 (2005), pp. 1708–1711. DOI: 10.1109/TMAG.2005.846059.
- [5] Z. Cendes and D. Shenton. “Adaptive mesh refinement in the finite element computation of magnetic fields”. In: *IEEE Transactions on Magnetics* 21.5 (1985), pp. 1811–1816. DOI: 10.1109/TMAG.1985.1063929.
- [6] Z.J. Cendes. “Vector finite elements for electromagnetic field computation”. In: *IEEE Transactions on Magnetics* 27.5 (1991), 3958–3966. DOI: 10.1109/20.104970.
- [7] Z.J. Cendes and J.-F. Lee. “The transfinite element method for modeling MMIC devices”. In: *1988., IEEE MTT-S International Microwave Symposium Digest* (1988), 623–626. DOI: 10.1109/mwsym.1988.22111.
- [8] Robert E. Collin. *Field theory of guided waves*. IEEE Press, 2015.
- [9] Saju Daniel and Sabu Thomas. “Shielding Efficiency Measuring Methods and Systems”. In: *Advanced Materials for Electromagnetic Shielding: Fundamentals, Properties, and Applications*. 2019, pp. 61–87. DOI: 10.1002/9781119128625.ch4.
- [10] Alexander V. Demakov and Maxim E. Komnatnov. “TEM cell for Testing Low-profile Integrated Circuits for EMC”. In: *2020 21st International Conference of Young Specialists on Micro/Nanotechnologies and Electron Devices (EDM)*. 2020, pp. 154–158. DOI: 10.1109/EDM49804.2020.9153508.
- [11] David J. Griffiths. *Introduction to electrodynamics*. Cambridge University Press, 2024.
- [12] C. Groh et al. “TEM waveguides for EMC measurements”. In: *IEEE Transactions on Electromagnetic Compatibility* 41.4 (1999), pp. 440–445. DOI: 10.1109/15.809846.
- [13] Robert C. Hansen and Robert E. Collin. *Small antenna handbook*. Wiley, 2013.
- [14] K.H. Huebner et al. *The Finite Element Method for Engineers*. A Wiley-Interscience publication. Wiley, 2001. ISBN: 9780471370789. URL: <https://books.google.at/books?id=f3MZE1BYq3AC>.
- [15] John David Jackson. *Classical Electromagnetism*. 2nd ed. Wiley.
- [16] Maciej Wladyslaw Jaroszewski, Sabu Thomas, and Ajay V. Rane. *Advanced materials for electromagnetic shielding: Fundamentals, properties, and applications*. Wiley, 2019.
- [17] J.P. Karst, C. Groh, and H. Garbe. “Calculable field generation using TEM cells applied to the calibration of a novel E-field probe”. In: *IEEE Transactions on Electromagnetic Compatibility* 44.1 (2002), pp. 59–71. DOI: 10.1109/15.990711.
- [18] M. Koch, C. Groh, and H. Garbe. “Exact Determination of Resonant Frequencies in TEM Cells”. In: *13th International Zurich Symposium and Technical Exhibition on Electromagnetic Compatibility*. 1999, pp. 653–658. DOI: 10.23919/EMC.1999.10791592.

- [19] Galen H Koepke. In: *Theory and measurements of radiated emissions using a TEM cell* (1989). DOI: 10.6028/nist.tn.1326.
- [20] Dominik Kreindl et al. “A Simulation Workflow for Predicting IC Stripline Radiated Emissions of Bond Wire-Based Systems”. In: *2024 14th International Workshop on the Electromagnetic Compatibility of Integrated Circuits (EMC Compo)*. 2024, pp. 69–73. DOI: 10.1109/EMCCompo61192.2024.10742020.
- [21] Dominik Kreindl et al. “Evaluation of an analytical equivalent Hertzian dipole representation in tem cells applying the finite element method”. In: *IEEE Transactions on Magnetics* 60.3 (2024), 1–4. DOI: 10.1109/tmag.2023.3324698.
- [22] Dominik Kreindl et al. “Measurement and Simulation Methodology for Characterizing the Shielding Effectiveness of Coating Materials for Optical Sensors”. In: *2023 International Symposium on Electromagnetic Compatibility – EMC Europe*. 2023, pp. 1–6. DOI: 10.1109/EMCEurope57790.2023.10274360.
- [23] Ján Kruželák et al. In: *Electrical conductivity, EMI absorption shielding performance, curing process and mechanical properties of rubber composites* (2024). DOI: 10.20944/preprints202401.1547.v1.
- [24] J.-F. Lee, D.-K. Sun, and Z.J. Cendes. “Full-wave analysis of dielectric waveguides using tangential vector finite elements”. In: *IEEE Transactions on Microwave Theory and Techniques* 39.8 (1991), pp. 1262–1271. DOI: 10.1109/22.85399.
- [25] J.F. Lee, D.K. Sun, and Z.J. Cendes. “Tangential vector finite elements for electromagnetic field computation”. In: *IEEE Transactions on Magnetics* 27.5 (1991), pp. 4032–4035. DOI: 10.1109/20.104986.
- [26] M.F.N. Mohsen. “Some details of the Galerkin Finite Element Method”. In: *Applied Mathematical Modelling* 6.3 (1982), 165–170. DOI: 10.1016/0307-904x(82)90005-1.
- [27] Cristian MORARI and Cristian BĂLAN. In: *Methods for determining shielding effectiveness of materials* (2015).
- [28] Clayton R. Paul, Robert C. Scully, and Mark A. Steffka. *Introduction to electromagnetic compatibility*. Wiley, 2023.
- [29] S. A. Schelkunoff. “The impedance concept and its application to problems of reflection, refraction, shielding and power absorption”. In: *Bell System Technical Journal* 17.1 (1938), 17–48. DOI: 10.1002/j.1538-7305.1938.tb00774.x.
- [30] D. Shenton and Z. Cendes. “Three-dimensional finite element mesh generation using Delaunay tessellation”. In: *IEEE Transactions on Magnetics* 21.6 (1985), 2535–2538. DOI: 10.1109/tmag.1985.1064165.
- [31] Ippalapalli Sreenivasiah, David Chang, and Mark Ma. “Emission characteristics of electrically small radiating sources from tests inside a tem cell”. In: *IEEE Transactions on Electromagnetic Compatibility* EMC-23.3 (1981), 113–121. DOI: 10.1109/temc.1981.303930.
- [32] GILBERT STRANG. *Analysis of the finite element method*. WELLESLEY-CAMBRIDGE Press, 2018.
- [33] John C Tippet, David C Chang, and Myron L Crawford. In: *An analytical and experimental determination of the cutoff frequencies of higher-order te modes in a Tem cell* (1976). DOI: 10.6028/nbs.ir.76-841.

- [34] C.M. Weil and L. Gruner. "High-order mode cutoff in rectangular striplines (short papers)". In: *IEEE Transactions on Microwave Theory and Techniques* 32.6 (1984), 638–641. DOI: [10.1109/tmtt.1984.1132745](https://doi.org/10.1109/tmtt.1984.1132745).
- [35] Perry F Wilson. In: *Excitation of a tem cell by a vertical electric Hertzian dipole* (1981). DOI: [10.6028/nbs.tn.1037](https://doi.org/10.6028/nbs.tn.1037).
- [36] Perry F. Wilson, David C. Chang, and Mark T. Ma. "Input Impedance of a Probe Antenna in a TEM Cell". In: *IEEE Transactions on Electromagnetic Compatibility* EMC-26.4 (1984), pp. 154–161. DOI: [10.1109/TEMC.1984.304216](https://doi.org/10.1109/TEMC.1984.304216).
- [37] Perry F. Wilson and Mark T. Ma. "Shielding-Effectiveness Measurements with a Dual TEM Cell". In: *IEEE Transactions on Electromagnetic Compatibility* EMC-27.3 (1985), pp. 137–142. DOI: [10.1109/TEMC.1985.304277](https://doi.org/10.1109/TEMC.1985.304277).
- [38] Perry F. Wilson and Mark T. Ma. "Simple approximate expressions for higher order mode cutoff and resonant frequencies in TEM cells". In: *IEEE Transactions on Electromagnetic Compatibility* 28.3 (1986), 125–130. DOI: [10.1109/temc.1986.4307269](https://doi.org/10.1109/temc.1986.4307269).